UNIVERSITY OF CALIFORNIA,
IRVINE

Development of 3D High-Q Fused Quartz Micro Structures for Precision Coriolis Vibratory Gyroscopes

DISSERTATION

submitted in partial satisfaction of the requirements
for the degree of

DOCTOR OF PHILOSOPHY

in Mechanical and Aerospace Engineering

by

Mohammad H. Asadian Ardakani

Dissertation Committee:
Professor Andrei M. Shkel, Chair
Professor J. Michael McCarthy
Professor Franco de Flaviis

2019

DEDICATION

This dissertation is dedicated to my parents,
Mina and Mehdi

TABLE OF CONTENTS

LIST OF FIGURES

LIST OF TABLES

ACKNOWLEDGMENTS

Firstly, I would like to express my sincere gratitude to my advisor Professor Andrei M. Shkel for the continuous support of my Ph.D. research, for his patience, motivation, and immense knowledge. Besides my advisor, I would like to thank the rest of my thesis committee: Professor J. Michael McCarthy and Professor Franco De Flaviis, for taking the time to review this dissertation and provide insightful comments. My sincere thanks also goes to Professor Lorenzo Valdevit and Professor Roger Rangel, for endorsing my application for the PhD program in Mechanical and Aerospace Engineering at UC Irvine.

I am grateful to my fellow labmates at UCI Microsystems Lab, Dr. Doruk Senkal, Dr. Sina Askari, Dr. Radwan M. Noor, Dr. Joan Giner de Haro, Dr. Sergei Zotov, Yusheng Wang, Daryosh Vatanparvar, Danmeng Wang, Yu-Wei Lin, Chi-Shih Jao, and Austin Parrish for the stimulating discussions and for the moments we spent together. I would like to thank Dr. Arash Zandian and Amir Saman Rezaei, for their assistance in the finite element simulations.

I also would like to thank Professor Thomas W. Kenny and his team at Micro Structures and Sensors Lab at Stanford University, especially Ian B. Flader, Yunhan Chen, Dustin D. Gerrard, Dongsuk D. Shin, and Hyun-Keun Kwon, for the collaboration opportunity on Stanford EpiSeal fabrication run. I would like to acknowledge UCI Integrated Nano-Research Facility (INRF) staff, Jake Hes, Dr. Mo Kebaili, and Richard Chang for their assistance on the fabrication process development.

I would like to acknowledge the funding provided by Defense Advance Research Projects Agency (DARPA). This work was partially supported under Grant No. N66001-16-1-4021, Grant No. N66001-12-C-4035, and Grant No. W31P4Q-11-1-0006 under the Micro-PNT and PRIGM-AIMS programs.

Last but not the least, I would like to thank my family, my parents and my sister, for encouraging me and supporting me throughout my education. I am grateful to Shiva, for her support, motivation, and patience during writing of this thesis.

CURRICULUM VITAE

Mohammad H. Asadian Ardakani

EDUCATION

Doctor of Philosophy in Mechanical Engineering **2019**
University of California, Irvine *Irvine, CA*

Master of Science in Mechanical Engineering **2017**
University of California, Irvine *Irvine, CA*

Master of Science in Mechanical Engineering **2010**
Amirkabir University of Technology (Tehran Polytechnic) *Tehran, Iran*

Bachelor of Science in Mechanical Engineering **2007**
Amirkabir University of Technology (Tehran Polytechnic) *Tehran, Iran*

RESEARCH EXPERIENCE

Graduate Student Researcher **2014–2019**
University of California, Irvine *Irvine, California*

Research Assistant **2012**
Florida International University *Miami, Florida*

Graduate Student Researcher **2007–2010**
Amirkabir University of Technology *Tehran, Iran*

TEACHING EXPERIENCE

Teaching Assistant - Mechanical Vibrations **2016-2018**
University of California, Irvine *Irvine, California*

Teaching Assistant - Discrete Mathematics **2014**
University of California, Irvine *Irvine, California*

Teaching Assistant - Mechanics of Solids **2013**
University of California, Irvine *Irvine, California*

Instructor - Engineering Design **2009-2010**
Amirkabir University of Technology *Tehran, Iran*

REFEREED JOURNAL PUBLICATIONS

- Asadian, M.H.; Wang, D.;Shkel, A.M.; Fused Quartz Dual Shell Resonator Gyroscopes, IEEE Journal of Microelectromechanical Systems (JMEMS), 2019 (in preparation).
- Asadian, M.H.; Wang, Y.; Shkel, A.M.; Development of 3D Fused Quartz Hemi-toroidal Shells for High-Q Resonators and Gyroscopes, IEEE Journal of Micromechanical Systems (JMEMS), accepted on 09/27/2019.
- Noor, R.M.; Asadian, M.H.; Shkel, A.M.; Design Considerations for Micro-Glassblown Atomic Vapor Cells, IEEE Journal of Microelectromechanical Systems (JMEMS), accepted on 10/06/2019.
- Wang, Y.; Asadian, M.H.; Shkel, A.M.; Compensation of Frequency Split by Directional Lapping in Fused Quartz Micro Wineglass Resonators, Journal of Micromechanics and Microengineering 28, no. 9, 2018.
- Asadian, M.H.; Askari, S.; Shkel, A.M.; An ultra-high vacuum packaging process demonstrating over 2 million Q-factor in MEMS vibratory gyroscopes, IEEE Sensors Letters, 1 (6), 2017.
- Wang, Y.; Asadian, M.H.; Shkel, A.M.; Modeling the Effect of Imperfections in Glassblown Micro-Wineglass Fused Quartz Resonators, ASME Journal of Vibration and Acoustics, 139 (4), 8, 2017.
- Senkal, D.; Ahamed, M.J.; Asadian Ardakani, M.H.; Askari, S.; Shkel, A.M.; Demonstration of 1 Million Q-Factor on Microglassblown Wineglass Resonators With Out-of-Plane Electrostatic Transduction, IEEE Journal of Microelectromechanical Systems (JMEMS), 24 (1), pp. 29-37, 2015.

REFEREED CONFERENCE PUBLICATIONS

- Asadian, M.H.; Noor, R.N.; Shkel, A.M.; Simulation-Based Approach in Design of 3D Micro-Glassblown Structures for Inertial and Optical Sensors, IEEE Sensors, Montreal, QC, October 2019.
- Asadian, M.H.; Askari, S.; Wang, Y.; Shkel, A.M.; Characterization of Energy Dissipation Mechanisms in Dual Foucault Pendulum Gyroscopes, IEEE International Symposium on Inertial Sensors and Systems, Naples, FL, April 2019.
- Asadian, M.H.; Wang, Y.; Shkel, A.M.; Design Space Exploration of Hemi-Toroidal Fused Quartz Shell Resonators, IEEE International Symposium on Inertial Sensors and Systems, Naples, FL, April 2019.

- Asadian, M.H.; Shkel, A.M.; Fused Quartz Dual Shell Resonator, IEEE International Symposium on Inertial Sensors and Systems, Naples, FL, April 2019.
- Vatanparvar, D.; Asadian, M.H.; Shkel, A.M.; Characterization of Scale Factor Nonlinearities in Coriolis Vibratory Gyroscopes, IEEE International Symposium on Inertial Sensors and Systems, Naples, FL, April 2019.
- Askari, S.; Asadian, M.H.; Askari, S.; Shkel, A.M.; Retrospective Correction of Angular Gain by Virtual Carouseling in MEMS Gyroscopes, IEEE International Symposium on Inertial Sensors and Systems, Naples, FL, April 2019.
- Noor, R. M.; Kulachenkov, N.; Asadian, M.H.; Shkel, A.M.; Study on MEMS Glass-blown Cells for NMR Sensors, IEEE International Symposium on Inertial Sensors and Systems, Naples, FL, April 2019.
- Asadian, M.H.; Askari, S.; Flader, I.B.; Chen, Y.; Gerrard, D.D.; Shin, D.D.; Kwon, H-K; Kenny, T.W.;Shkel, A.M.; High Quality Factor Mode Ordered Dual Foucault Pendulum Gyroscope, IEEE Sensors, New Delhi, India, October 2018.
- Asadian, M.H.; Wang, Y.;Shkel, A.M.; Design and Fabrication of 3D Fused Quartz Shell Resonators for Broad Range of Frequencies and Increased Decay Time, IEEE Sensors, New Delhi, India, October 2018.
- Askari, S.; Asadian, M.H.; Shkel, A.M.; High quality factor MEMS gyroscope with whole angle mode of operation, IEEE International Symposium on Inertial Sensors and Systems, Lake Como, Italy, March 2018.
- Asadian, M.H.; Wang, Y.; Askari, S.; Shkel, A.M.; Controlled Capacitive Gaps for Electrostatic Actuation and Tuning of 3D Fused Quartz Micro Wineglass Resonator Gyroscope, IEEE International Symposium on Inertial Sensors and Systems, Kauai, Hawaii, April 2017.
- Wang, D.; Asadian, M.H.; Efimovskaya, A.; Shkel, A.M.; A Comparative Study of Conventional Single-Mass and Amplitude Amplified Dual-Mass MEMS Vibratory Gyroscopes, IEEE International Symposium on Inertial Sensors and Systems, Kauai, Hawaii, April 2017.
- Wang, Y.; Asadian, M.H.; Shkel, A.M.; Frequency Split Reduction by Directional Lapping of Fused Quartz Micro Wineglass Resonators, IEEE International Symposium on Inertial Sensors and Systems, Kauai, HI, April 2017.
- Askari, S.; Asadian, M.H.; Kakavand, K.; Shkel, A.M.; Near-navigation grade quad mass gyroscope with Q-factor limited by thermo-elastic damping, Solid-State Sensors, Actuators, and Microsystems Workshop, Hilton Head Island, South Carolina, USA, June 2016.
- Askari, S.; Asadian, M.H.; Kakavand, K.; Shkel, A.M.; Vacuum sealed and getter activated MEMS Quad Mass Gyroscope demonstrating better than 1.2 million quality

factor, IEEE International Symposium on Inertial Sensors and Systems, Laguna Beach, CA, March 2016.

- Wang, Y.; Asadian, M.H.; Shkel, A.M.; Predictive Analytical Model of Fundamental Frequency and Imperfections in Glassblown Fused Quartz Hemi-Toroidal 3D Micro Shells, IEEE Sensors, Orlando, FL, November 2016.
- Senkal, D.; Ahamed, M.J.; Asadian, M.H.; Askari, S.; Shkel, A.M.; Out-of-plane Electrode Architecture for Fused Silica Micro-glassblown 3-D Wineglass Resonators, IEEE Sensors, Valencia, Spain, November 2014.

Patent Disclosures

- Shkel, A.M.; Asadian, M.H.; Fused Quartz Dual-Shell Resonators and Method of Fabrication, UC Case No. 2019-670.
- Shkel, A.M.; Wang, Y.; Asadian, M.H.; Piezo Actuation of Fused Quartz Dual Shell Resonator, UC Case No. 2020-334.

ABSTRACT OF THE DISSERTATION

Development of 3D High-Q Fused Quartz Micro Structures
for Precision Coriolis Vibratory Gyroscopes

By

Mohammad H. Asadian Ardakani

Doctor of Philosophy in Mechanical and Aerospace Engineering

University of California, Irvine, 2019

Professor Andrei M. Shkel, Chair

The contribution of this Ph.D. thesis is in development of miniaturized 3-dimensional structures with high stiffness symmetry, high damping symmetry, and high Q-factor, for potential implementation as precision rate and rate-integrating Coriolis Vibratory Gyroscopes (CVGs). The focus of this research is toward sensor design and process development, based on Microelectromechanical System (MEMS) techniques, for realization of 3D "Fused Quartz" micro-shell gyroscopes. The challenges in fabrication of low-frequency and 3D high-Q microstructures are addressed. A precision micro-assembly, as a crucial technological step, is developed to complete the development cycle of micro-shell gyroscope devices. "Dual-shell" architectures are introduced as an innovative approach for implementation of 3D microresonators and gyroscopes. A test-bed for 2D silicon MEMS gyroscopes is designed and implemented to study the limiting dissipation mechanisms of resonant structures. An ultra-high vacuum sealing process with proven long-term vacuum stability is developed, eliminating the primary damping mechanism for MEMS resonators and gyroscopes.

Several new fabrication processes for "non-flat" 3D microstructures are developed based on the high-temperature micro-glassblowing technique. Limitations of the previously developed baseline process in fabrication of low-frequency shell resonators are addressed by

introducing and demonstrating two alternative approaches, leading to realization of micro-shell resonators with a broad range of operational frequencies, from a few to hundreds of kilohertz. The Q-factor up to 1.7 million was demonstrated by improving the surface quality and reducing residual thermal stresses in the micro-shell resonators.

Temporal evolution of 3D micro-shells during the glassblowing process was simulated using a time-dependent fluid flow model. The hybrid fluidic-structural simulation framework enabled a prediction of final geometry, modal characteristics, and dynamic behavior of micro-shells. The simulations were used toward design optimization to (1) reduce the energy dissipation and (2) enhance the shock resilience in micro-shells. The models were used in optimization of structures for operation through environmentally challenging conditions.

A vacuum-compatible micro-assembly process was developed for integration of micro-shell resonators with reduced capacitive gaps ($<5\mu$m), which is a critical technological step leading to improvements in sensitivity of shell-type devices. The electrostatic actuation, detection, and frequency-mismatch tuning, as well as the rate gyro operation, are demonstrated on fabricated 3D micro-shell resonators.

This thesis developed a practical realization of the fused quartz "dual-shell" structures for 3D MEMS resonators and gyroscopes. A full-cycle of development, including design, modeling, fabrication, as well as instrumentation of the structure as a resonator and a gyroscope, is presented. The high-Q dual-shell resonators with an amplitude ring-down time of over 120 seconds and with the Q-factor of 3.75 million were experimentally demonstrated. The obtained results are a glimpse of design opportunities for high performance and compact form factor MEMS gyro implementations using 3D shell geometries.

Finally, the energy dissipation mechanisms in MEMS vibratory gyroscopes were studied. An ultra-high vacuum sealing process was developed to eliminate viscous damping, one of the major contributing factor to energy dissipation. A 2D "flat" silicon MEMS gyro

was designed as a test structure for the energy dissipation study. The Q-factors above 1.1 million were measured on the device, approaching its fundamental thermoelastic damping (TED). The low-temperature Q-factor measurements revealed the Q-factor of 9.29 million, associated with the anchor loss, which, to the best of our knowledge, is the highest Q-factor reported on silicon MEMS resonators. More importantly, the developed approach for cryogenic characterization of micro-resonators offers a methodology for study high precision gyroscopes and resonators, which is expected to be broadly adopted by future research efforts on the topic.

Chapter 1

Introduction

This Chapter presents a background and principle of operation of Micro Electro Mechanical System (MEMS) based Coriolis Vibratory Gyroscopes (CVG), followed by a literature review. Objectives of the research are formulated, and the chapter is concluded by outline of the dissertation.

1.1 Motivation

The current Microelectromechanical system (MEMS) inertial sensors are based on the well-developed commercially-available bulk-micromachining, for example Silicon-on-Insulator (SOI), and surface micromachining fabrication technologies. A variety of designs - tuning forks, rings, and disk resonators- have been implemented using silicon microfabrication technology, in pursuit of improving the noise performance of microscale Coriolis Vibratory Gyroscopes (CVGs). However, the existing silicon MEMS technology fundamentally suffers from large imperfections in fabrication, which limits the accuracy of the existing sensors. Innovative design solutions, new materials, and innovative microfabrication processes are required to achieve the necessary level of accuracy and increase performance of the next-generation of

MEMS inertial sensors, as compared to the present state-of-the-art technologies.

The most successful implementation of a CVG on macro-scale is a Hemispherical Resonator Gyroscope (HRG) architecture, which demonstrated the performance on the level of 0.0005 deg/hr bias stability [3]. The advantages of existing HRG technology are in its high sensitivity, extremely low dissipation, environmental stability, and robust operation with proven performance over millions of hours without any failure [3]. The principle of operation of the HRG is based on the precession of elastic waves in a rotating solid object. The core of HRG is an axisymmetric hemispherical resonator made out of fused silica, which is manufactured using a precision machining process. Advantages of the fused silica 3D hemispherical geometry are the absence of precedence directions due to isotropic material properties of fused quartz and axial symmetry in the wineglass geometry, resulting in high tolerances to shock and environmental vibrations, and low energy dissipation due to a low intrinsic loss in the material and reduced energy transfer from the resonator to the supporting substrate. The disadvantages of the current HRG technology, despite its outstanding performance and successes, are its extremely high cost, complexity of manual assembly of multiple discrete parts, relatively large size, and high power consumption.

The majority of existing MEMS gyroscopes are "flat" 2D structures. The miniaturization of HRGs requires a revolutionary microfabrication technology with an unprecedented capability of fabricating "non-flat" 3D structures. The goal of such technology would be to enable batch-fabrication of chip-scale micro-shell resonator gyroscopes. Maintaining the key characteristics of resonators (their high Q-factor, damping symmetry, and frequency symmetry) in micro-shells are critical, as they directly relate to the gyro performance metrics. When fully matured, the low-cost chip-scale 3D micro-shell resonator gyroscopes with high accuracy in rotation measurements would lead to a broad application spectrum, from self-contained on-chip navigation systems to compact platforms for precision location services. This dissertation develops the micro-fabrication techniques and addresses challenges in re-

alization of high-Q and environmentally robust micro-shell resonators for precision CVGs. This work is in continuation of previous efforts in advancing the microfabrication technologies for realization of 3D micro rate-integrating gyroscopes, initially presented in [4].

1.2 Background

The principle of operational of a CVG is based on rotation-induced Coriolis acceleration measurement by a vibrating structure. The sensitive element of a CVG can be either a series of lumped masses utilizing translational vibration or distributed masses such as rings, disks, and shells utilizing flexural standing waves. In both implementations, the equations of motion of an ideal sensing element can be written in terms of the primary (drive) and secondary (sense) generalized displacements:

$$\begin{bmatrix} \ddot{x} \\ \ddot{y} \end{bmatrix} + 2\xi_0\omega_0 \begin{bmatrix} 1 & 0 \\ 0 & 1 \end{bmatrix} \begin{bmatrix} \dot{x} \\ \dot{y} \end{bmatrix} + \omega_0^2 \begin{bmatrix} 1 & 0 \\ 0 & 1 \end{bmatrix} \begin{bmatrix} x \\ y \end{bmatrix} = \begin{bmatrix} F_x/m \\ F_y/m \end{bmatrix} + \begin{bmatrix} 2\Omega\dot{y} \\ -2\Omega\dot{x} \end{bmatrix}, \tag{1.1}$$

where Ω is the input rotation, ω_0 is the resonant frequency of the mode-matched gyro in $[rad/sec]$, ξ_0 is the damping ratio, m is the modal mass, F_x and F_y are the control forces applied to the orthogonal gyro's axes.

CVGs can be instrumented in rate and rate-integrating modes to measure the angular rate and the angle of rotation, respectively [5]. In the rate mode of operation, the oscillation with a controlled amplitude is established along the drive axis, and the Coriolis acceleration coupling excites the oscillation along the sense mode. The steady-state amplitude of the sense mode is linearly related to the external input rotation. In the rate-integrating mode of operation, the oscillation pattern precesses freely in response to an external rotation. The position of the oscillation pattern with respect to gyroscope's rotating frame is proportional to the absolute angle of rotation, and the precession rate is proportional to the angular rate.

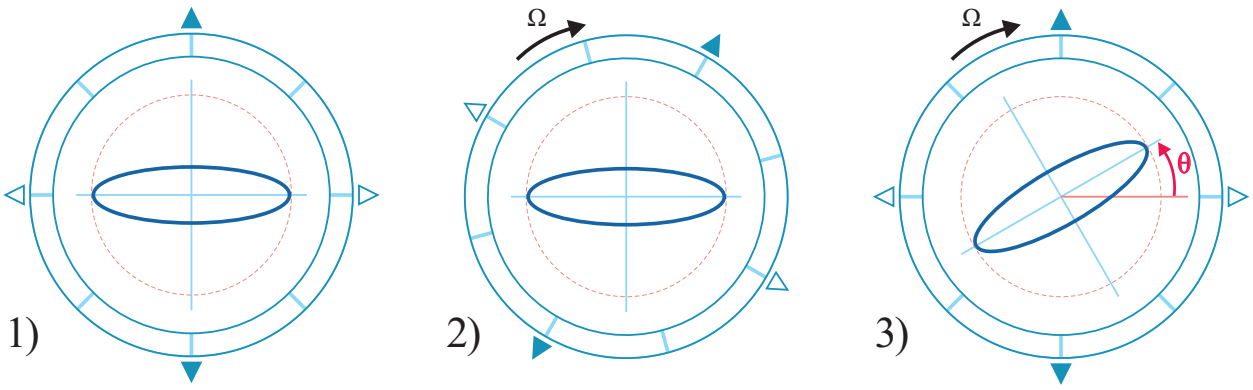

Figure 1.1: Principle of rate-integrating mode of operation, (1) oscillation pattern when there is no rotation applied to the gyroscope, (2) oscillation pattern from an observer point of view in an inertial fixed coordinate frame after a rotation is applied, (3) oscillation pattern from an observer point of view in a non-inertial rotating coordinate frame (gyro body fixed) after a rotation is applied. Precession of the oscillation pattern in the gyroscope rotating frame gives a direct angle measurement of the input inertial rotation (A_g=1, $\theta_0 = 0$)

Fig. 1.1 schematically illustrates the rate-integrating mode of operation.

MEMS CVG Operational and Performance Parameters

Mechanical scale factor in the rate mode of operation is the ratio of sense axis displacement to the input rate of rotation. In the presence of frequency mismatch in a rate gyro, the mechanical scale factor is [6]:

$$SF_{mech} = \frac{y_{ss}}{\Omega} = \frac{2A_g m_d X_{ss} \omega_d}{m_s \omega_s^2 \sqrt{[1 - (\frac{\omega_d}{\omega_s})^2]^2 + [\frac{1}{Q_s}\frac{\omega_d}{\omega_s}]^2}} \tag{1.2}$$

where X_{ss} is the steady-state amplitude of the drive oscillation, ω_d is the frequency of the drive oscillation, ω_s is the sense resonant frequency, Q_s is the Q-factor of the sense oscillation, A_g is the angular gain, m_d and m_s are the effective masses in the drive and sense oscillations. In mode-matched rate gyroscopes, where ω_s=ω_d=ω, the mechanical scale factor is maximized. Assuming an inertial isotropy (m_d=m_s), the scale factor of a mode-matched

rate gyro can be written as:

$$SF_{mode-matched} = \frac{y_{ss}}{\Omega} = \frac{2A_g X_{ss} Q}{\omega} \tag{1.3}$$

Thus, a higher sensitivity can be achieved through mode-matching, increasing the drive amplitude and Q-factor, reducing the operational frequency. The ratio of $\frac{Q_s}{\omega}$ is equal to $\frac{1}{2}\tau$, where τ is the amplitude ring-down time constant of the oscillation.

Angular gain in the rate-integrating mode of operation is the ratio of the vibration pattern precession angle to the input angle of rotation, or the corresponding time derivatives of these parameters:

$$\begin{aligned} \dot{\theta} &= -A_g \Omega \\ \theta &= \theta_0 - A_g \int_{t_0}^{t} \Omega(\tau) d\tau \end{aligned} \tag{1.4}$$

where θ, as shown in Fig. 1.1, is the precession angle of the oscillation pattern. The mechanical angular gain is related to the portion of modal mass that contributes to the Coriolis force, and depends exclusively on the mass distribution of the sensing element.

Angle drift in the output of a rate-integrating gyroscope is related to the damping and the frequency asymmetry, based on the model derived in [7]:

$$\dot{\theta} = -A_g \Omega + \frac{1}{2}\Delta\left(\frac{1}{\tau}\right) sin2(\theta - \theta_\tau) \frac{E}{\sqrt{E^2 - Q^2}} + \frac{1}{2}\Delta\omega cos2(\theta - \theta_\omega) \frac{Q}{\sqrt{E^2 - Q^2}}, \tag{1.5}$$

where E is the energy, Q is the quadrature error, $\Delta\omega = \omega_x - \omega_y$ is the frequency mismatch, $\Delta(\frac{1}{\tau}) = \frac{1}{\tau_x} - \frac{1}{\tau_y}$ is the damping mismatch, θ_ω is the orientation of principal axes of elasticity, θ_τ is the orientation of principal axes of damping. The principal axes of damping and principal axes of damping are not generally aligned. The damping and frequency symmetry in a rate-integrating gyroscope are required to reduce the drift in the angle measurement

output.

Allan deviation is a statistical method to analyze the time domain output signal, and to quantify different random noise modes.

Bias Instability is the smallest value in the Allan deviation plot of Zero-Rate-Output (ZRO), which is related to the $1/f$ noise (Flicker noise) and has units of deg/hr (or deg/sec).

Angle Random Walk (ARW) is attributed to the rate white noise and identified with the -1/2 sloped part in the log-log scale of Allan variation plot. The ARW has units of $deg/\sqrt{hr}$ and sometimes is referred to as the rate resolution with units of $deg/hr/\sqrt{Hz}$. The rate resolution depends on the Mechanical-Thermal Noise (MTN) of the proof mass and the noise in the electronics circuitry that converts the motional current to pick-off voltage signals.

Mechanical-Thermal Noise (MTN) equivalent rate in an open-loop rate gyroscope defines the lower bound in the sensor performance. The Q-factor of the sense mode, frequency mismatch between the drive and the sense modes, and amplitude of the drive mode are the parameters influencing the MTN equivalent rate, [8]:

$$\Omega_{rw} \approx \sqrt{\frac{k_B T \omega_y}{A^2 M_{eff} \omega_x^2 Q_y} \left[1 + \left(\frac{Q_y(\omega_y^2 - \omega_x^2)}{\omega_y \omega_x}\right)^2\right]^{-1}}, \tag{1.6}$$

In summary, the high Q-factor, damping symmetry, and stiffness symmetry are the critical characteristics to improve the performance in MEMS rate and rate-integrating gyroscopes. These are the optimization parameters that will be discussed in this thesis.

Energy Dissipation Mechanisms in MEMS

The Q-factor is a figure of merit that indicates the dissipation of energy in MEMS Resonators. The primary energy dissipation mechanisms in MEMS resonators and gyroscopes are (1)

viscous damping, (2) anchor losses, (3) thermoelastic damping (TED), (4) mode-mixing losses, and (5) intrinsic material losses [9]. The overall Q-factor can be calculated form the reciprocal sum of the Q-factors from all of the damping mechanisms:

$$\frac{1}{Q_{overall}} = \frac{1}{Q_{viscous}} + \frac{1}{Q_{material}} + \frac{1}{Q_{surface}} + \frac{1}{Q_{mode-mixing}} + \frac{1}{Q_{TED}} + \frac{1}{Q_{anchor}} + \frac{1}{Q_{Other}} \quad (1.7)$$

The weakest link among the energy dissipation mechanisms limits the overall Q-factor of a resonant structure [9]. In MEMS devices, because of the large surface-to-volume ratio and small spacing between static and moving structures, the viscous damping is the major source of energy dissipation, unless the vibratory device is operated in a high-vacuum encapsulation. The anchor loss, TED, and mode conversion loss depend on the structural design, mode of operation, and fabrication imperfections. In an ideal case, a dynamically-balanced structure operating in an anti-phase balanced mode mitigates the dissipation of energy through the substrate, as the net reaction forces and moments acting on the anchors are minimized [10]. The examples of dynamically balanced modes are "wine-glass vibration modes" in the disk, ring, and shell resonators. In the lumped mass designs, anti-phase driven multi-mass implementations mitigate the dissipation of energy through the substrate. A tuning-fork type gyroscope provides a dynamically-balanced motion along a selected axis of oscillations. A proper suspension element design would provide a large frequency separation between the operational mode and spurious modes, and would minimize the mode conversion losses [11].

Thermoelastic Damping (TED) is an energy dissipation mechanism in resonators due to a non-reversible heat conduction in a solid medium, as a result of coupling between the non-homogeneous strain fields and the temperature field within the vibration structure [12, 13]. The general expression of the TED based on the Zener's model for a beam element is,

$$Q_{TED}^{-1} = \left(\frac{E\alpha^2 T_0}{\rho C_p}\right) \sum_k f_k \frac{\omega\tau_k}{1 + (\omega\tau_k)^2} \quad (1.8)$$

where, ρ is the density, C_p is the heat capacity at constant pressure, E is the Young's modulus, α is the Coefficient of Thermal Expansion (CTE), T_0 is the equilibrium temperature, ω is the mechanical angular frequency, k denotes the number of thermal modes, f_k are the weights with $\sum f_k = 1$, and τ_k denotes the relaxation time constant to establish a temperature equilibrium across length b_k of different thermal modes,

$$\tau_k = \frac{b_k^2}{\pi^2 D} \tag{1.9}$$

where D is the thermal diffusivity of the material. The maximum energy dissipation through TED occurs when $\tau_k \omega = 1$, which maximizes the summation term in Eq. 1.8. Besides, TED strongly depends on the CTE of resonator's material. The Q_{TED} in fused quartz resonant structures is anticipated to be higher than the silicon counterparts because of a lower CTE of fused quartz, $\alpha_{FQ} = 0.51 \times 10^{-6}[K^{-1}]$ [14], as compared to silicon, $\alpha_{Si} = 2.55 \times 10^{-6}[K^{-1}]$ [15]. Eq. 1.8 and Eq. 1.9 suggest that TED can be reduced through the geometry of design and material selection of MEMS resonators.

Even though this model was developed of a cantilever beam, and we are considering in this thesis shell resonators, the model highlights some key characteristic parameters in design of resonators for a variety of geometries [16].

1.3 Prior Art

The amorphous and isotropic structural properties of engineered glasses make them an attractive structural material for a variety of applications, such as biomedical, optics, photonics, and mechanical sensors. A variety of microfabrication techniques have been developed for 2D glass processing in fabrication of microfluidic channels, photonic waveguides, and microlenses, such as laser ablation [17], abrasive-jet blasting [18], Reactive Ion Etching (RIE) [19], and Femtosecond Laser Irradiation and Chemical Etching (FLICE) [20]. The

state-of-the-art fabrication processes to realize MEMS-based 3D resonant structures can be classified into two main categories: (1) thin-film shell resonators and (2) bulk-deformed shell resonators. In the former, thin-film structural and sacrificial layers were deposited on pre-etched hemispherical cavities or precision micro-spheres, and the micro-shell resonators were released by removal of the sacrificial material. The bulk-deformed shell resonators were fabricated in a high-temperature thermo-plastic deformation process where the structural materials, such as borosilicate glass, Bulk Metallic Glass (BMG), Ultra-Low Expansion (ULE) glass, and fused quartz, were blown or molded in a 3D geometry. In this section, the recent efforts in the development of 3D micro-shell resonators were presented.

1.3.1 Micro-shell Resonators by Thin Film Deposition

This section focuses on review of micro-shells fabricated by deposition of a thin-film structural layer, such as silicon dioxide, polysilicon, and polycrystalline diamond, on a pre-defined mold. The thickness of thin-film shell resonators were typically limited by the maximum thickness allowance to achieve a low-stress thin-film deposition; hence, the micro-shells fabricated by thin film deposition processes would typically have thicknesses smaller than 5μm and diameters on the order of 2 mm. This is an alternative approach to the one presented in this thesis, which to date has been less successful in realization of 3D shell architectures.

- Silicon dioxide hemispherical resonators were fabricated by isotropically etching cavity molds in a silicon substrate and thermally growing SiO_2 inside a cavity to create a spherical shell. The shell was released by removing the surrounding silicon molds in XeF_2 [21]. The thermal oxide was often selected as the shell material due to its similar thermal properties to fused silica. In [21], micro-shells with the equatorial radius of 500 μm and the nominal thickness of 2 μm were fabricated with radial deviation of $<4\mu$m. For electrostatic actuation and detection, 30 nm TiN was deposited by atomic layer deposition (ALD). Electrodes were etched on a separate SOI wafer using the

Bosch process. Shells and electrodes were assembled and bonded using an adhesive layer. Radial capacitive gaps of 30 μm were achieved after assembly. The electrostatic characterization in [21] revealed the Q-factor of $\sim$ 5600 at the resonant peak of n=4 wineglass mode at 113.9 kHz. The effect of thickness anisotropy from the non-uniform etching of the underlying silicon cavity on the frequency mismatch of the wineglass degenerate was studied [22].

- Polysilicon micro-shell resonators with a shell thickness of 660 nm and a shell diameter of 1200 μm were fabricated with 16 integrated electrodes for driving, tuning, and sensing [23]. A hemispherical shell was fabricated by a three-dimensional high aspect-ratio poly- and single crystalline silicon (3D-HARPSS) process with self-aligned tall capacitive electrodes intended for driving, sensing, and tuning of the gyroscope. High Aspect-Ratio Poly- and Single crystalline Silicon (HARPSS) process was used to fabricate 2D devices [24]. The Q-factor of 40,000 was measured at the center frequency of 33 kHz after optimization of stem geometry [25].

- In [26], sputtered SiO_2 hemispherical shells with a shell diameter of 500 μm were fabricated by pre-etching hemispherical molds in a silicon wafer and depositing amorphous silicon as the sacrificial layer. A probe tip was used to actuate the device, and LDV was used to pick up the vibration signal. The Q-factor of 22,000 was reported at 22 kHz under a vacuum level of 50 mTorr.

- Sputtered ULE micro-wineglass resonator was proposed in "Poached-Egg Micro-Molding" fabrication process [27]. Precision sapphire ball lenses were uniformly coated with a polysilicon sacrificial layer. 1.2 μm ULE was sputtered as the device layer. The device and sacrificial layers above the equator of the ball were etched. The sacrificial layer and the ball lens were removed to release the hemispherical ULE wineglass. Thickness uniformity of 120 ppm and less than 0.125 μm deviations from a perfect sphere were reported. The Q-factor of 20,000 at 17.32 kHz was reported [28].

- SiO_2 3D micro-shell was introduced by HRL laboratories [29]. All-dielectric cylindrical gyroscopes were fabricated and characterized using electric field gradients. The dissipation through deposition of a conductive layer was mitigated, in this work. The Q-factor of 12,000 at 47 kHz was reported for this device in [30].

- Single crystalline diamond offers very high strength, high thermal conductivity, and low coefficient of thermal expansion (CTE), which may potentially result in low TED and suitable for high Q resonators [31]. There was a growing interest in exploring diamond as a structural material in micro-shell resonators. In [32], micromachined polycrystalline diamond hemispherical resonators were fabricated by 1 μm hot-flame chemical vapor deposition (HFCVD) of the microcrystalline diamond (MCD) into hemispherical cavities. The hemispherical molds were created by micro-EDM (electro-discharge machining). A conformal layer of SiO_2 was deposited on the silicon mold as a sacrificial layer in the CVD process and later removed by HF release. Electrostatic excitation was applied through a probe tip and LDV detection at the rim of the shell for frequency response characterization. In [33], the Q-factor of 6300 associated with 0.11 s ring-down time at the center frequency of 18.3 kHz was reported with an as-fabricated frequency mismatch of 5 Hz. In [34], MCD micro wineglass resonators were operated in the rate mode. A scale factor of 140 μV/deg/s and ARW of 11 mdeg/s/rt-Hz was reported. In [35], microcrystalline cylindrical resonators were fabricated with a device thickness of 5 μm in DRIE etched silicon molds. The Q-factor of 313,000 was reported at 23 kHz with as-fabricated frequency mismatch of 3 Hz. In [36], the Q-factor was improved to 580,000 which was attributed to the post-fabricating thermal annealing surface treatment.

- A 1.4 mm diameter MCD micro-shell resonator with integrated electrodes was fabricated by the Draper Laboratory and reported in [37]. Glass cavities were isotropically etched to fabricate molds for the deposition of MCD. The Q-factor as high as 20,000

was reported on the n=2 wineglass modes. Laser trimming was demonstrated to permanently tune the frequency mismatch to better than 0.3 Hz by selectively removing material from a segmented rim of the shell. Q-factor of up to 143,000 in the fundamental wineglass mode at 16 kHz was reported [38].

- Half-toroidal MCD resonators were fabricated by Honeywell and reported in [39]. Instead of etched cavities, the group fabricated a hemi-toroidal glass mold by micro-glassblowing. Boron-doped MCD structural layer with 0.8 to 1.5 μm thickness was deposited using the HFCVD process. Polysilicon layers were used for sacrificial layer and also as a hard mask for subsequent patterning of the MCD layer. Devices with the frequency range of 6 kHz to 11 kHz were fabricated, and as-fabricated frequency mismatch as low as 2.4 Hz was reported.

- A Nickel-Iron alloy (Invar36) was also used by thin-film deposition to fabricate 3D hemispherical shells [40]. Invar36 was a Nickel-Iron (36/64) alloy with a very low coefficient of thermal expansion [41]. Micro-shells with 3.5 to 5.6 μm thicknesses, and the diameter of 780 to 910 μm were demonstrated in literature. The Q-factor up to $\sim$ 3200 was achieved on as-fabricated device, and the Quality factor of $\sim$7600 was reported on the annealed micro-shells which was attributed to a reduction of CTE due to thermal annealing.

- In [42], boron-doped polysilicon shell resonators were fabricated with self-aligned integrated spherical electrodes. A silicon mold was isotropically etched in a $< 111 >$ wafer. The thermal oxide was grown as the sacrificial layer and coated with 2 μm polysilicon as the structural material. The spherical electrodes were dry-etched, and the sacrificial layer was removed to release the polysilicon shell. The fabrication process can potentially be scaled to wafer-level for the fabrication of 3D micro-shells.

- In [43], a highly-symmetric silicon dioxide, SiO_2, 3D micro-shell resonator with a thickness of 650 nm and a diameter of 180 μm was fabricated by thermally oxidizing and

patterning of a $< 111 >$ silicon substrate. The Q-factor of 31,542 was reported at the center frequency of 100 kHz with a frequency mismatch of 512 Hz. A deep isotropic chemical etching process was introduced to etch highly isotropic cavities in a silicon substrate with pop-up ring masks in an HNA (hydrofluoric, nitric, acetic) etching process.

1.3.2 Micro-shell Resonators by Thermo-Plastic Deformation

In this section, micro-shell resonators fabricated by large deformation of a bulk structural layer are reviewed. Micro-shell resonators made out of BMG, borosilicate glass, ULE glass, and fused quartz were reported in literature by the blow-molding and the glassblowing processes. These approaches are directly related to the approach discussed in this thesis and served as a starting point for the process developments.

- The micro-glassblowing process was initially developed for wafer-level fabrication of micro-spherical glass cells for nuclear magnetic resonance (NMR) atomic sensors by the MicroSystems laboratory at the University of California, Irvine (UCI) [44, 45, 46]. The design parameters of glass-blown micro-spheres was described analytically. An array of sub-mm micro-cells was fabricated by etching cavities in a silicon wafer using DRIE, followed by bonding a borosilicate glass wafer to the silicon substrate and glassblowing at 850 ℃.

- The process was adapted for the fabrication of micro-spherical resonators with 3D capacitive electrodes by the UCI group [47]. In addition, metal traces where introduced on the glass before the glassblowing, which were subsequently formed into 3D patterns and used for electromagnetic actuation of shells [48]. Later, by the same group, micro-wineglass resonators with different stem designs were fabricated by laser trimming of the micro-spheres [49].

- By the UCI group, inverted micro-wineglass resonators with self-aligned stems were fabricated by pre-etching hemi-toroidal cavities on a silicon substrate, followed by wafer bonding and glassblowing [50]. An electrode assembly with adjustable capacitive gaps were fabricated separately on an SOI wafer and assembled on the micro-wineglass shells for the electrostatic actuation and detection. The electrode design with position resolution of 10 μm enabled adjusting the capacitive gaps on the vicinity of the released shell [51]. A fabrication process for inverted wineglass borosilicate glass devices with integrated electrodes was developed for excitation and detection of n=2 vibration modes. As-fabricated frequency symmetry of 160 mHz was reported, demonstrating the capability of micro-glassblowing to fabricate highly symmetric structures when a furnace with high temperature uniformity was utilized [52].

- In [53], micro-spherical resonators with in-situ integrated silicon electrodes were fabricated on a stack of silicon-glass-silicon bonded wafers. Cavities were initially etched on a silicon substrate and anodically bonded to a glass wafer. The electrode wafer was bonded to the other side of the glass prior to glassblowing. Electrodes were etched on silicon in the DRIE process, followed by glassblowing of the micro-sphere resonator. Inner surface of the glass-blown micro-spheres was coated using ALD for electrostatic transduction. The electrostatic frequency response characterization demonstrated feasibility of excitation and detection of flexural vibration modes in a high-frequency micro-spherical resonator.

- By the UCI group, a high-temperature (>1700 ℃) micro-glassblowing process was developed for a batch-fabrication of fused quartz and ULE micro-wineglass resonators [54]. Plasma activation fusion bonding was employed for direct bonding of wafers with similar materials. The surface roughness measurement before and after glassblowing demonstrated an improvement in the surface roughness due to the smoothing effect of surface tension forces. The composition of glass was analyzed by Energy Disper-

sive X-Ray Spectroscopy (EDX) and revealed that high-temperature glassblowing does not alter the composition of the glass material [55]. The design of inverted-wineglass resonators were described in [56]. The out-of-plane electrode architecture was implemented for electrostatic excitation and detection of wineglass modes [57]. The Q-factor of 1.14 million and an as-fabricated frequency mismatch of 14 Hz on a metal-coated fused quartz micro-shell resonator with a center frequency of 105 kHz was reported in [1].

- In [58], an analytical model based on a combination of the Rayleigh's energy method and the generalized collocation method was developed to predict the frequency of wineglass modes in hemi-toroidal glass-blown micro-shell resonators. The effect of lapping misalignment on the frequency mismatch between the orthogonal wineglass modes and a balancing technique to permanently tune the frequency mismatch on micro-shell resonators by directional lapping approach were presented in [59]. In [60], the effect of thermal and chemical post-processing of the surface quality and the Q-factor of micro-shells were reported.

- In [61], the blow-torch molding process was introduced to fabricate micro-Birdbath resonators. In this process, an annular cavity was machined in a graphite fixture and the fused silica substrates were clamped on the fixture. During the blow-torch molding, the cavity was pumped down to create the pressure difference and pull down the substrate into the cavity. The substrate of 3D micro-Birdbath resonators was mechanically lapped, and the exposed rim of the shells was fine-polished in a chemical mechanical planarization (CMP) process [62]. The Q-factor as high as $\sim$ 10 million were reported on n=2 and n=3 modes of two different un-coated micro-shell resonator with a diameter of 10 mm [63, 64]. In [65], an in-run bias instability of 0.03 deg/hr on metal-coated micro-Birdbath Resonator Gyroscope (μBRG) with Q-factor of 419,000, and in [66], an in-run bias instability of 0.01 deg/hr was reported on a μBRG with the

Q-factor of 1.55M, which was the best noise performance demonstrated by a MEMS gyroscope to date.

- A whirling platform was integrated to the blow-torch molding approach to fabricate micro-shell resonators with more uniform thickness distribution in [67]. The micro-shell resonators were released from the substrate using a femto-second laser ablation process. T-shaped masses were added to the rim of the resonator shell to improve the electrostatic actuation and detection efficiency. The Q-factor of 37,000 was reported at the center frequency of 9.6 kHz.

- In [68, 69], micro-spherical and micro-hemispherical shells were fabricated using blow molding of a thin sheet of Platinum-based BMG. The BMG exhibits outstanding mechanical properties such as high strength and elasticity as well as homogeneity, material isotropy, and electrical conductivity [70, 71]. The BMG micro-shells were blow-molded at 275 ℃ to a pre-etch hemispherical glass cavity. The gold electrodes were deposited and patterned on the cavity before blow-molding. After mechanical grinding and polishing the excess material, a hemispherical BMG shell was released from the underlying gold electrodes due to thermal mismatch coefficient, resulted in 15 μm separation between the sensing element and electrodes. The Q-factor of 6000 was reported at the center frequency of 9 kHz. Devices were annealed at 190 ℃ for 120 hours. The Q-factor after annealing was improved to 9600, which was explained as the reduction of the residual thermal stresses.

1.3.3 Research Objectives

A performance gap exists between the current MEMS-based gyros and the gyro technologies in the navigation systems, such as Ring Laser Gyros (RLG), Fiber Optics Gyros (FOG), and Hemispherical Resonator Gyroscopes (HRG). The HRG technology, with an outstanding Q-factor of over 25 million and a bias instability of 0.0005 deg/hr, motivated the de-

velopment of new designs and innovative processes to advance the micro-fabrication of 3D micro-structures. The primary goal of this research is to develop new MEMS-based technologies for realization of 3D micro-shell resonators with broad range of operational frequencies, low energy dissipation, and high-shock tolerance.

One of the objectives of this research was to address the technological challenges of the existing process and to enable the batch-fabrication of low-frequency micro-shell resonators. The optimization of micro-shell geometry was also identified in this thesis as a crucial step to reduce the energy dissipation and a achieve high mechanical Q-factor. Toward this goal, the design space of micro-shells was explored to identify the critical geometric parameters at different operational frequencies.

The design optimization requires knowledge about the geometry of glass-blown micro-shells, especially the non-uniform thickness distribution, height, and stem geometry. Toward this goal, a finite element model of the micro-glassblowing process was developed in this thesis to simulate the temporal evolution of micro-shells in the micro-glassblowing process and to predict the final glass-blown geometry.

Operation of the micro-shell resonators as a gyroscope required integration of the glass-blown micro-shells with an electrodes substrate with controlled capacitive gaps less than 5 μ. Development of a vacuum-compatible assembly process was another objective of this research, which led to electrostatic actuation, detection, tuning, and gyro operation, all demonstrated on an integrated micro-shell resonator gyroscope. The reduction of capacitive gaps in a controlled fashion was a technological step leading to drastic improvements of sensitivity of shell-type devices.

One of the key characteristics in the macro-scale HRGs is their immunity to external shocks. The high-shock tolerance in micro-shell resonators requires innovative designs and processes. The "dual-shell" concept was proposed to be investigated as a potential solution to achieve

high-performance and high-shock tolerance in micro-scale 3D resonators. The dual-shell resonators anticipated to provide a rugged structure which would enhance the mechanical integrity in a compact form factor, would enable an in-situ vacuum encapsulation when integrated with electrode substrate, and would create a protection shield for the resonating structure. Demonstration, for the first time, of a dual-shell resonator and a gyroscope and completion of a full-cycle of development were pursued in this research.

Achieving high mechanical Q-factor in silicon MEMS resonators and gyroscopes was another objective of this research. Toward this goal, the primary energy dissipation mechanism was identified as the viscous damping, and a vacuum sealing process to effectively eliminate the viscous damping was developed. A new suspension element for mode-ordering was proposed to reduce the energy dissipation through mode-mixing and anchor loss in dual-mass anti-phase driven MEMS resonant structures.

1.4 Thesis Outline

In Chapter 2, the design optimizations for the fused quartz micro-shell resonators are presented. The primary objectives of the design space exploration are (i) selection of micro-shell geometric parameters to increase the modal frequency separation, especially in low-frequency resonators, (ii) mitigation of the energy dissipation in shell resonators through TED, and (iii) ordering the resonant modes, such that the operational n=2 wineglass mode becomes the first mode of vibration. It is demonstrated that for a given frequency of interest, there are multiple combinations of micro-shell geometric parameters which satisfy the design optimization goals. Also, the limitations of the baseline micro-glassblowing process in the fabrication of fused quartz micro-shells are discussed. The alternative processes are developed, enabling fabrication of micro-shells with broad range of geometries. As a result, micro-shell resonators with wide range of operational frequencies, from 4 kHz to 100 kHz, are realized.

Chapter 3 is dedicated to simulation of the temporal evolution of the micro-shells in the micro-glassblowing processes. A time-dependent isothermal fluid flow model was developed, which captures sufficient mechanisms of the micro-glassblowing process to predict the final glass-blown shell geometry. The assumptions of developed model, material properties, governing equations, and the boundary conditions are discussed in details. The developed model employs a time-dependent pressure boundary condition which is continuously calculated at each time-step, based on the geometry of deforming shell. The FEM simulations demonstrate the self-limiting nature of the micro-glassblowing process and predicts the micro-shell geometry based on the initial design and process parameters. We also present the post-processing of fluid flow results to calculate the modal frequencies using model analysis, and estimate the response of the micro-shells to transient dynamic loads, such as external shock and vibrations.

In Chapter 4, we report the frequency response characterization results and post-fabrication assembly process of micro-shells to build an operational resonator gyroscope. We report the Q-factor of over 1.7 million in a micro-shell resonator at the center frequency (n=2 mode) of 22 kHz, which corresponds to over 25 seconds of ring-down time. We report the effect of thermal annealing on the Q-factor improvement as a piece of evidence that residual thermal stresses are limiting the Q-factor in glass-blown micro-shell resonators. We also present a vacuum-compatible and temperature-robust assembly process to build a gyroscope prototype. We discuss the material selection criteria, based on the electrical, thermal, and chemical compatibility of the process. We demonstrate a uniform capacitive gaps of < 5 μm in an assembled micro-shell on planar electrodes. We demonstrate, for the first time, the electrostatic tuning of frequency mismatched and the gyro operation in a glass-blown fused quartz micro-shell device.

In Chapter 5, for the first time, we present a "dual-shell" resonator gyroscope. The full-cycle design, process development, prototype fabrication, integration, and gyro operation from

concept to final device is presented. We report the Q-factor of over 1 million repeatedly in multiple dual-shell prototypes with center frequencies in the range of 4.7 kHz to 9.6 kHz. The ring-down time of over 120 seconds was reported on a dual-shell resonator at the center frequency of 4.7 kHz, which corresponds to over 1.8 million mechanical Q-factor. On n=3 mode of operation, we report the Q-factor of over 3.7 million. We demonstrate the assembly and vacuum encapsulation of "dual-shell" resonators using a silicon-in-glass electrode substrate. The electrostatic frequency characterization, frequency tuning, and open-loop gyro operation are demonstrates on the "dual-shell" resonator gyroscopes.

In Chapter 6, we report our results on the development of high-Q silicon MEMS gyroscopes. First, we demonstrate an ultra-high vacuum sealing process for an effective elimination of viscous damping in a compact leadless chip carrier packages for MEMS inertial sensors. We report the Q-factor of over 2 million on a ∼2 kHz silicon MEMS Quad Mass Gyroscope (QMG). An ultra vacuum stability is reported based on the Q-factor measurement over a long period of time. Besides, for the first time, we present a mode-ordering suspension element for silicon MEMS Dual Foucault Pendulum (DFP) gyroscopes. The mode-ordered DFP provides a large frequency separation between the high-Q anti-phase operational mode and low-Q in-phase spurious mode. We demonstrate Q-factors of over 1.1 million in a fabricated mode-ordered DFP, which corresponds to the damping mismatch of ∼0.0002 Hz. In order to eliminate the TED and make the anchor loss observable, the Q-factors are measured at low-temperature in a Cryogenic probe station setup from 78 ℃ to 360 ℃. An outstanding Q-factor of 9.29 million is measured at 110 ℃, and is identified as the anchor loss limit in the mode-ordered DFP.

In Chapter 7, a summary of contributions and future research directions are presented.

Chapter 2

Process Development

2.1 Introduction

In this chapter, the micro-shell design optimization, considering scaling of resonant modes and thermoelastic damping with micro-shell geometry, are discussed. MEMS-based micro-fabrication processes were developed to fabricate 3D high-Q fused quartz micro-shell resonators with a broad range of operational frequencies. Micro-shell structures with a variety of geometric parameters were fabricated in these processes.

2.2 Design Space Exploration

The main parameters in the design of shell resonators are thickness, diameter, and anchor radius, Fig. 2.1. The frequency of operational and spurious vibration modes, the dissipation of energy through Thermoelastic Damping (TED), and anchor loss depend on the design of shell resonators. In this section, scaling of the resonant frequency of operational and spurious vibrations modes with respect to the shell radius, thickness, and anchor radius are analyzed using a parametric Finite Element (FE) modal analysis.

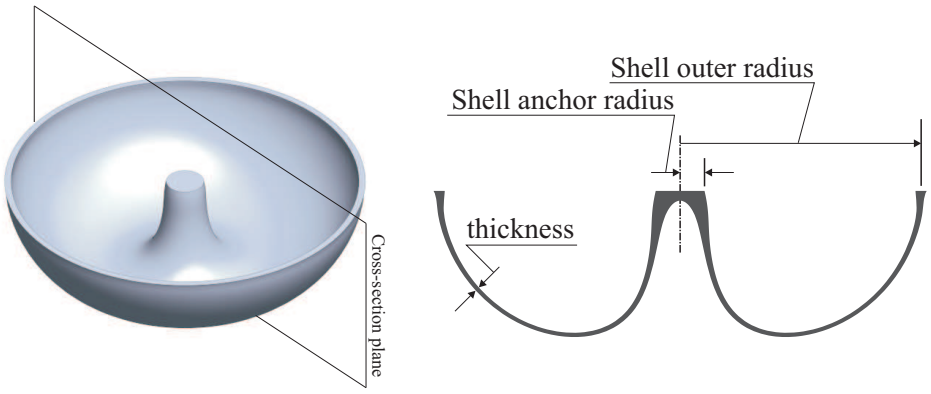

Figure 2.1: Schematics of a typical 3D shell resonators showing the geometric features; thickness, anchor radius, and outer radius.

2.2.1 Scaling of Modal Resonant Frequencies

Similar to any continuous structures with distributed mass and stiffness, such as beams, rings, plates, and membranes, a 3D shell geometry has an infinite number of orthogonal vibration modes. Fig. 2.2 shows six vibrational modes of a typical hemi-toroidal shell geometry, anchored at the central stem. An input rotation along the axis of symmetry of shell resonators couples (any) degenerate wineglass modes through the Coriolis acceleration and can be configured to detect the rotation rate (rate gyro) or the absolute angle of rotation (whole angle gyro). The n=2 wineglass mode is considered to be a preferable structural mode for operation due to its higher angular gain, which is related to a measure of sensitivity in the whole angle gyroscopes.

The resonant frequency of the $n\Theta$ wineglass modes of hemispherical and hemi-toroidal shells was approximated analytically based on the Rayleigh's energy method [72, 58]. In a hemi-toroidal shell with a uniform thickness, the wineglass frequency is (nearly) linearly proportional to the thickness and (nearly) inversely proportional to the square of the diameter. A parametric FE modal analysis was performed using ANSYS Workbench modal analysis module to derive the frequency scaling of the resonant modes. A hemi-toroidal geometry was considered to approximate the fused quartz micro-shell geometry. It was assumed that

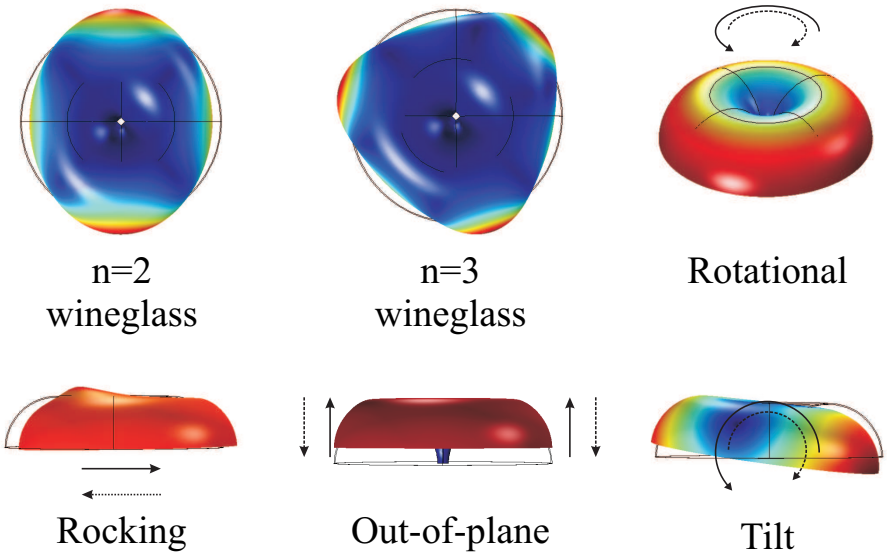

Figure 2.2: The first six resonance modes of a typical hemi-toroidal shell structure, any degenerate wineglass modes can be used for rotation sensing. The n=2 mode is preferable due to a higher gain in the whole angle mode of operation.

the shell was fully evolved to a hemi-toroidal shape, and the thickness was uniform, Fig. 2.3. The shell thickness, anchor radius, and shell outer radius were defined as parameters, and the modal analysis simulations were performed for more than 200 design combinations.

The scaling of resonant frequencies with respect to three geometric parameters are plotted in Fig. 2.4a-c. For a constant anchor radius and thickness, Fig. 2.4a, the frequency of all resonance modes decreased with the increase of the shell radius. Fig. 2.4b shows the effect of

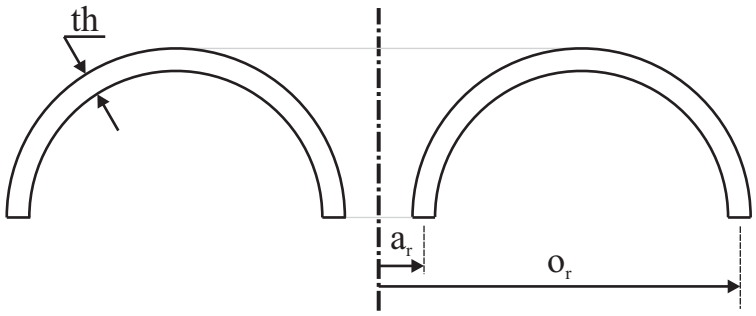

Figure 2.3: Schematics of cross-section of a hemi-toroidal shell used to approximate the micro-shell geometry in the parametric FE simulations for frequency scaling analysis. The anchor radius, a_r, shell outer radius, O_r, and the shell thickness, th, are indicated on the cross-sectional view.

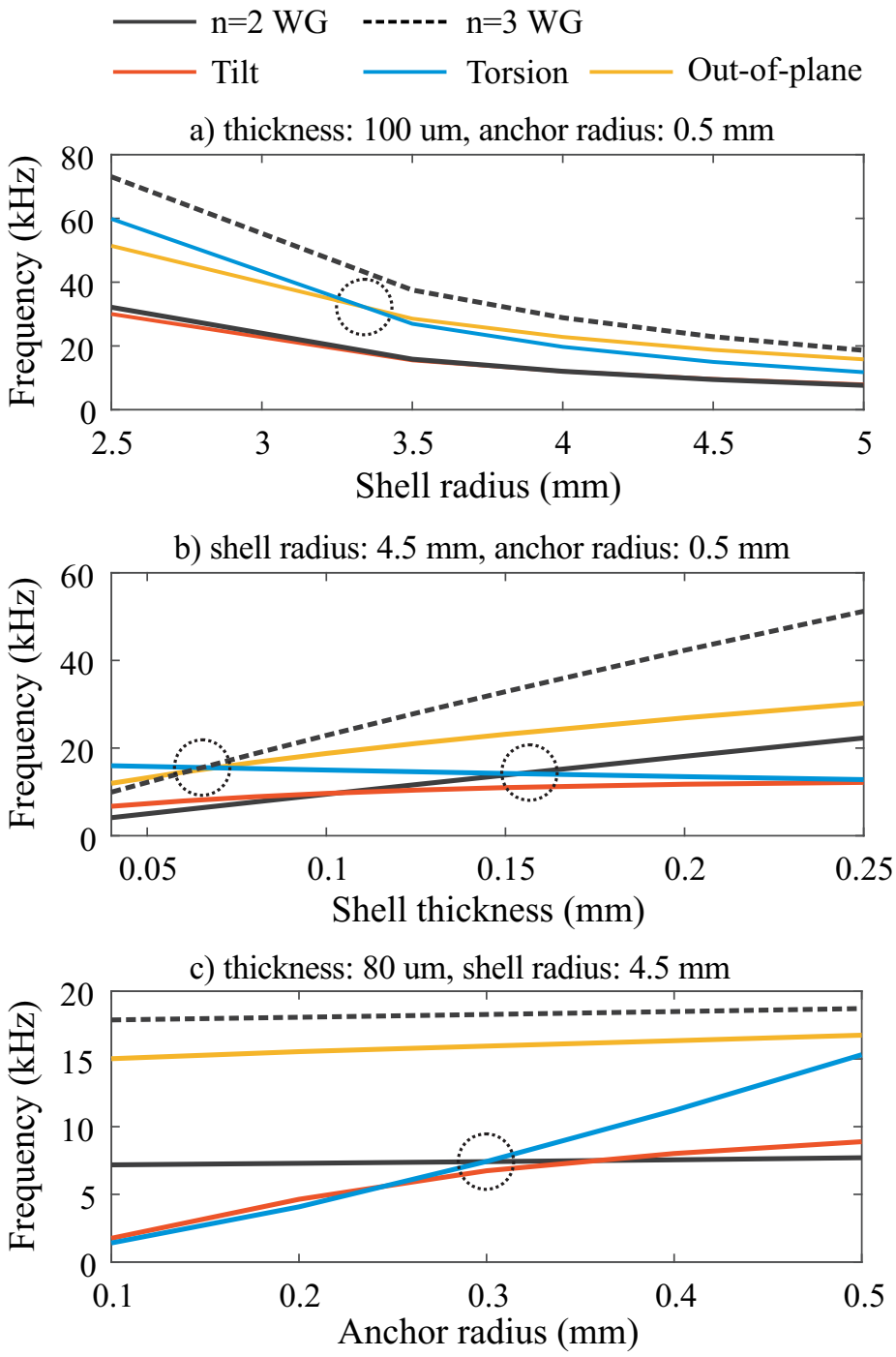

Figure 2.4: Scaling of the resonance frequencies with respect to the geometry of hemi-toroidal shell resonators. Notice, the order of structural modes can switch at certain geometries. Circles indicate the geometries that the mode order of the n=2 wineglass mode and its closest spurious modes changes.

the thickness on the resonant frequencies with a constant shell radius and anchor size. It was observed that the order of resonance modes would switch at certain shell thicknesses (circled in Fig. 2.4b). A similar trend was observed with anchor sizes, Fig. 2.4c. A larger anchor radius resulted in a higher torsional resonant frequency, while the wineglass and the out-of-plane modes were nearly insensitive to the size of the anchor. Similar trends were observed in other combinations of the shell radius, anchor radius, and thickness. The analysis of the frequency scaling results reveal that:

- The resonance modes scale differently with respect to geometrical parameters of the hemi-toroidal shell;
- The frequency separation between the n=2 wineglass mode and spurious mode changed with shell geometry;
- The order of the resonance modes switched at certain geometries.

Based on the above observations, the different scaling of modal resonant frequencies would allow optimization of geometric parameters to fulfill the large frequency separation between the resonance modes and the mode-ordering condition in micro-shell resonators.

2.2.2 Effect of Shell Geometry on Modal Frequency Separation

The shell radius, thickness, and anchor size are the design parameters that define the geometry of a hemi-toroidal shell. Using a series of parametric FE modal simulations, the shell thickness, radius, and anchor radius were varied from 40 μm to 150 μm, 2.5 mm to 5 mm, and 100 μm to 500 μm, respectively, to generate more than 200 design combinations. The n=2 wineglass resonant frequency and the frequency separation with the closest parasitic mode at different design combinations were identified and plotted in Fig. 2.5. In this plot, each data point represents a distinct shell geometry, forming the design space for the geometry of hemi-toroidal shell resonators. The design space demonstrates that for a wineglass

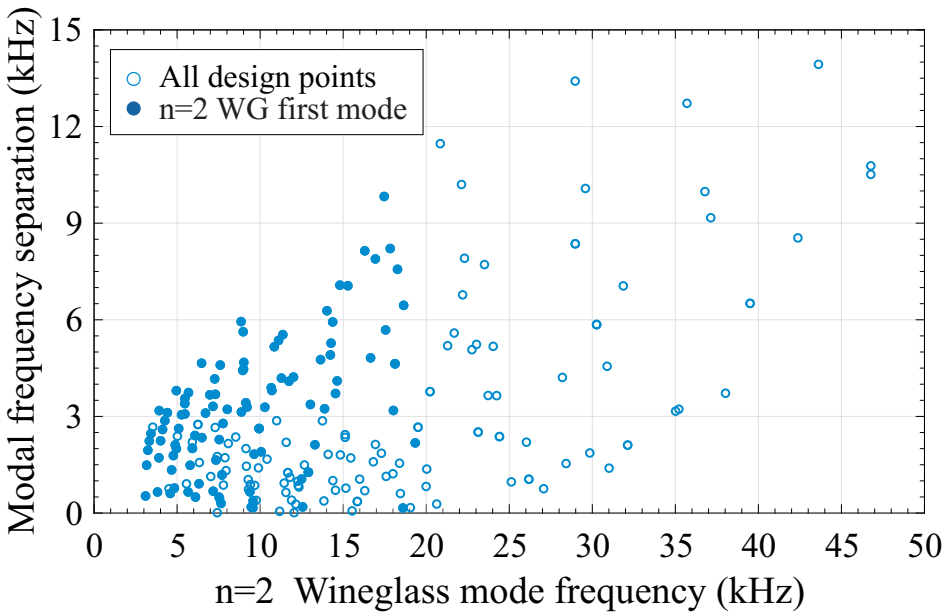

Figure 2.5: The design space of hemi-toroidal shell resonators; frequency separation between the operational and the closest spurious modes at different n=2 wineglass resonance frequencies. Each data point represents a distinct shell geometry. The solid dots represent the mode-ordered design combinations where the n=2 wineglass is the lowest resonance mode.

frequency of interest, a shell resonator can be obtained from a different combination of design parameters. Also, it indicates that separation between spurious and operational modes depends on the selection of the geometric parameters. The result demonstrated a possibility of ordering the resonance modes of a shell resonator, with spurious modes at higher resonance frequencies, as compared to the frequency of the n=2 wineglass mode, which is an important consideration to avoid an environmental excitation of the device during operation. The solid data points in Fig. 2.5 refer to cases where the mode-ordering condition is satisfied, and the n=2 wineglass mode has the lowest resonance frequency.

The trend of data points revealed that the modal frequency separation decreases at lower operational frequencies. Thus, at lower frequencies, the shell geometry must be optimized to avoid the proximity of spurious modes to the n=2 wineglass mode.

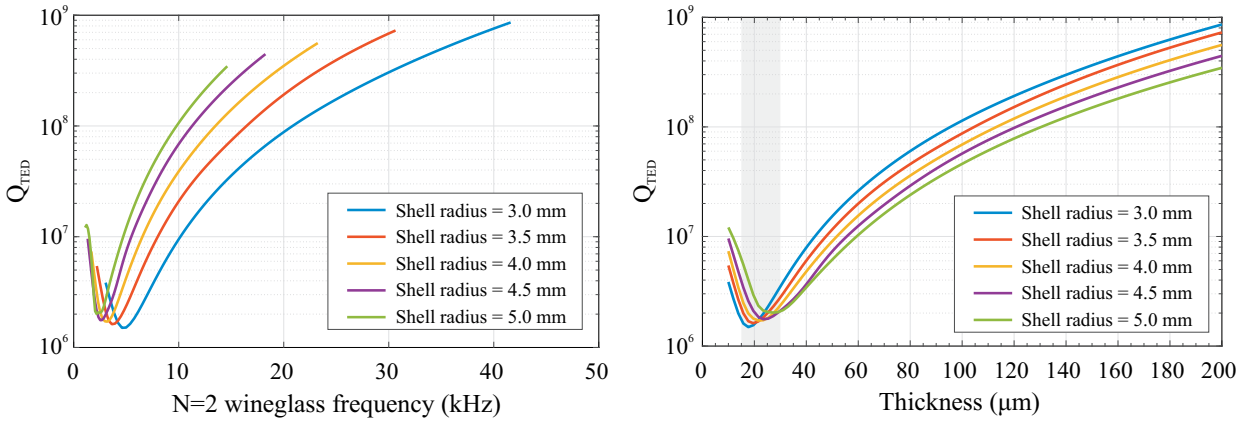

Figure 2.6: Simulated Q_{TED} of uncoated micro-shell resonators with "hemi-toroidal" geometry are plotted as a function of N=2 wineglass frequency (left) and as a function of shell thickness (right). The maximum dissipation was observed for the thickness in the range from 20μm to 30μm.

2.2.3 Effect of Shell Geometry on Thermoelastic Damping

The Q_{TED} of fused quartz shell resonators were calculated for the n=2 wineglass mode from FE simulations, using COMSOL Multiphysics. The Q_{TED} is plotted as a function of the n=2 frequency, and as a function of thickness in Fig. 2.6, for the shell radius from 3 mm to 5 mm, and the shell thickness from 10 μm to 200 μm. Among all geometric parameters, thickness has the most significant effect on the TED in shell resonators [16]. For the range of studied parameters, the minimum Q-factor occurred when the thickness was between 20μm and 30 μm, corresponding to the condition when the resonant frequency was between 2 kHz and 5 kHz. The quasi-isothermal condition in thinner shells and the quasi-adiabatic condition in thicker shells cause a weaker coupling between the strain field and the thermal field, reducing the energy dissipation through TED. Also, the amplitude ring-down time was calculated based on the simulated Q_{TED} and the n=2 wineglass frequency and plotted in Fig.2.7. A similar trend was observed in the ring-down time.

A lower operational frequency in shell resonators relaxes the capacitive gap requirement for

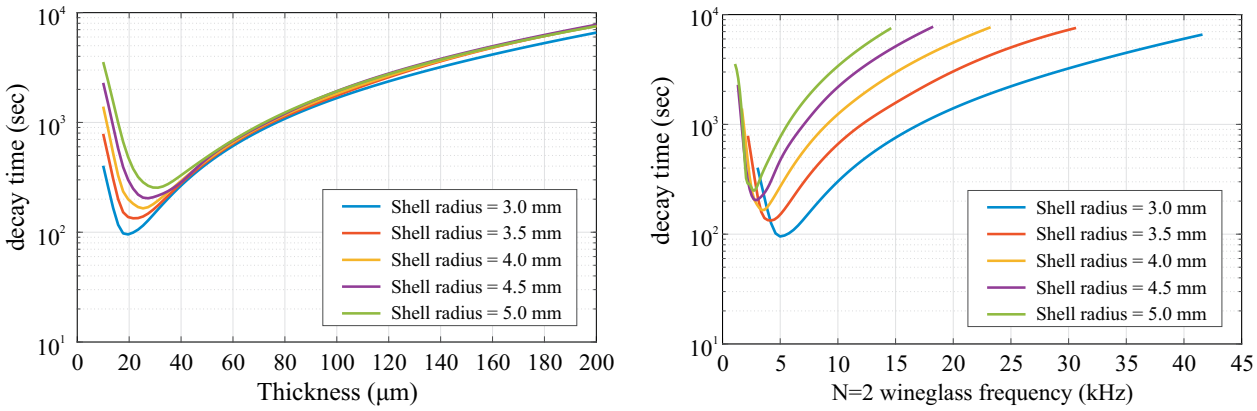

Figure 2.7: Simulated decay time constant (τ) of shell resonators with "hemi-toroidal" geometry are plotted as a function of N=2 wineglass frequency (left) and as a function of shell thickness (right). A minimum of $\sim$ 90 seconds amplitude decay time constant is expected for the simulated hemi-toroidal geometries.

Table 2.1: A subset of design combinations from Fig. 2.5, corresponding to n=2 wineglass frequency $\sim$ 10 kHz.

Shell radius (mm)	Shell thickness (μm)	Anchor radius (mm)	N=2 Freq. (kHz)	Freq. separation (kHz)	Mode-ordered	Q-TED
3.5	60	0.6	10.21	3.2	Y	1.9E7
3.5	60	0.7	10.60	3.8	Y	1.9E7
4.0	80	0.6	10.02	1.9	Y	3.5E7
5.0	125	1.0	10.38	1.6	Y	8.1E7
5.0	150	0.3	10.84	4.4	N	1.6E8

the electrostatic frequency tuning when shell resonators are instrumented to operate as a mode-matched gyroscope [2]. The design space was defined to select design parameters for low-frequency shell resonators to increase the modal separation and achieve mode-ordering. The TED analysis was performed to avoid the design parameters that lead to increased energy dissipation (lowest Q_{TED}). A set of parameters corresponding to design combinations with $\sim$ 10 kHz are listed in Table 2.1. The modal frequency separation varies from 1.6 kHz to 4.4 kHz for the chosen set of parameters.

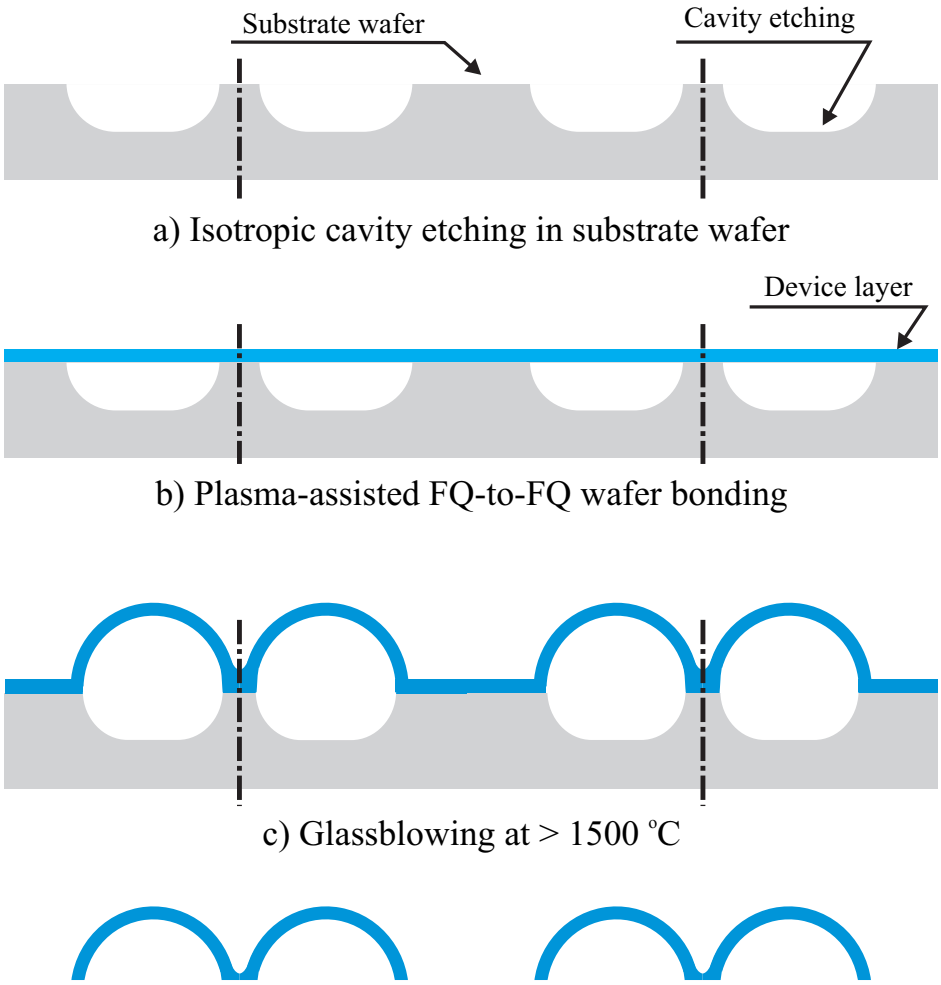

Figure 2.8: The baseline micro-glassblowing fabrication process [1]

2.3 Fabrication of Hemi-Toroidal Shell Resonators

The high-temperature micro-glassblowing processes were developed to realize the fused quartz micro-shell resonators with a broad range of geometries and operational frequencies.

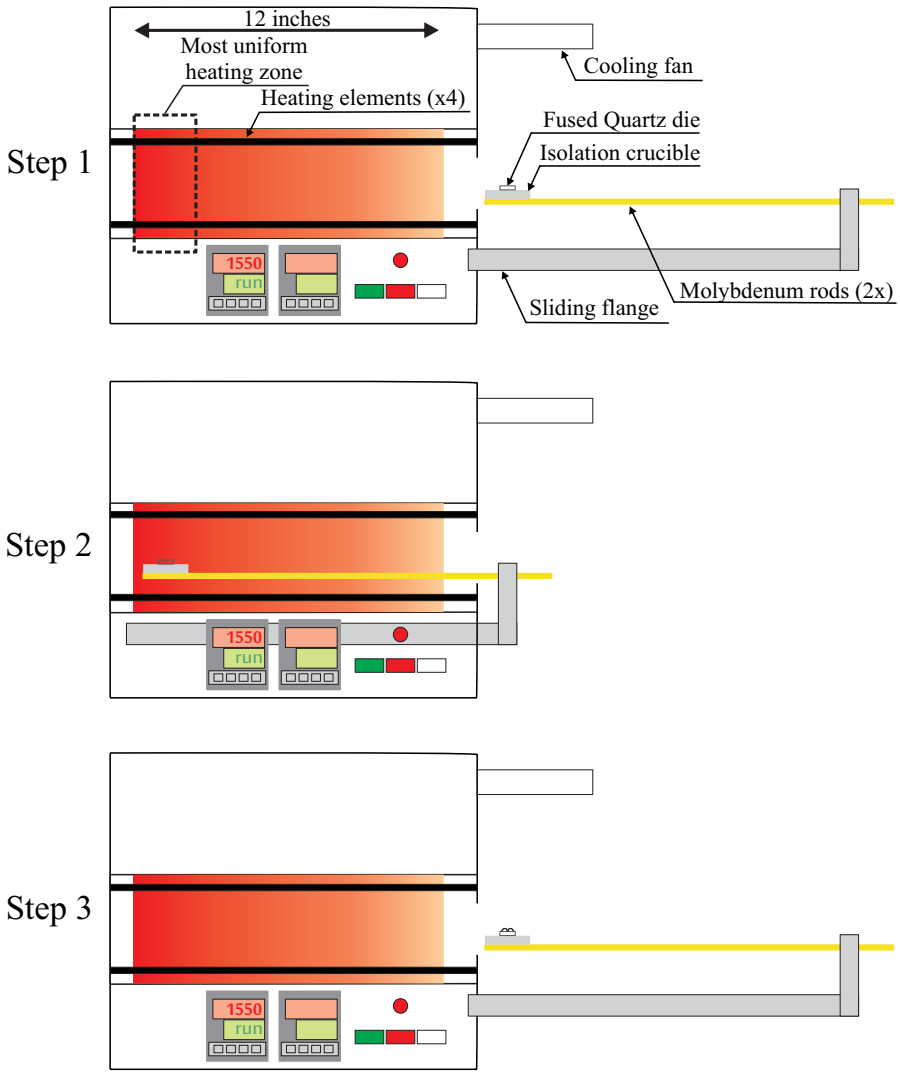

Figure 2.9: Schematics of a die-level glassblowing process using a high-temperature furnace with a sliding flange for loading and unloading of the samples. Step 1: furnace is at 1550 ℃, Step 2: sample is loaded into the furnace for glassblowing (2-3 minutes), Step 3: sample retrieved and fast cooled using the cooling fan. The schematics shows a side-view of the furnace.

2.3.1 Baseline Micro-Glassblowing Process

A high-temperature micro-glassblowing process was developed in [1] for fabrication of symmetric fused quartz wineglass resonators. In the baseline process, a fused quartz "substrate" wafer was initially coated with a thin-film of PolySilicon (2 microns) as a hard mask in a low-pressure chemical vapor deposition (LPCVD) process. Annular cavities were etched on the fused quartz substrate wafer in a wet etching process using hydrofluoric (HF) acid (48 wt. % in water solution). The Polysilicon hard mask was removed using potassium hydroxide (KOH) solution (45 wt. % in water solution). The standard grade Corning HPFS® 7980 wafers were used as the "device" wafer. The pre-etched substrate wafer was bonded to a blank fused quartz (or ULE) device wafer using the plasma-assisted wafer bonding under atmospheric pressure conditions. The bonding surface activation was performed in a PlasmaTherm Reactive Ion Etching (RIE) chamber at 90 [mTorr] pressure under 25 [sccm] flow of oxygen and 50 [W] coil power. After the surface activation, wafers were rinsed with DI wafer, blow-dried with nitrogen, and bonded manually. The bonding was followed by thermal annealing at 400 [℃] to complete the bond formation. After dicing the bonded pair of wafers, the individual dies were transferred to a Rapid Thermal Processing (RTP) furnace, operating at a temperature above the softening point of the fused quartz (>1500 [℃]) to perform the micro-glassblowing. The process takes between 2 to 3 minutes to evolve the micro-shell structures completely. For the die-level micro-glassblowing process, a tube RTP furnace with a sliding flange (MTI GSL-1500X-RTP50) for fast heating and fast cooling was used. Fig. 2.9 shows schematically the steps of the die-level micro-glassblowing. The samples are loaded into the uniform temperature zone of the furnace, step 2, and retrieved from the furnace, step 3, using the sliding flange. In order to reduce the temperature gradient caused by the zirconium rods, a perforated quartz crucible was used to thermally isolate the samples from the rods. After the glassblowing, the shells were released from the substrate using a back-lapping process, Fig. 2.8. A shell resonator with the Q-factor of 1.1 million

after metal coating at the operational frequency of $\sim$ 100 kHz was demonstrated using the baseline process [1].

The glassblowing process is a high-temperature thermal process which consists of transient and steady-state thermal regimes. The transient regime is at the beginning of the process when the die is loaded into the furnace. The temperature of the sample increases until it reaches a steady-state condition. During (most of) the transient regime, the temperature is below the softening point of fused quartz, and viscous deformation does not occur. Hence the volume of the cavity does not change. However, the internal pressure rises with temperature, according to the ideal gas law with constant gas volume assumption,

$$P_i = \frac{T_i}{T_{wb}} \times P_{wb} \tag{2.1}$$

where P_i is the internal pressure inside the encapsulated cavity, T_i is the instantaneous temperature of the sample, T_{wb} and P_{wb} are the temperature and pressure of the wafer bonding, respectively. The build up of the internal pressure induces tensile stresses within the fused quartz sample. The maximum stress, σ_{max}, occurs at the edge of encapsulated cavities due to stress concentration,

$$\sigma_{max} = K_t \frac{(P_i - P_{gb})(r_2 - r_1)}{2\ t_i} \tag{2.2}$$

where K_t is the stress concentration factor, P_{gb} is the pressure of glassblowing furnace, r_1 and r_2 are the inner and outer radius of the pre-etched cavity, respectively, and t_i is the initial device wafer thickness. The maximum stress is proportional to r_2 and inversely proportional to t_i. A stationary solid mechanics FE model was utilized to compute the maximum tensile stress in fused quartz samples. The pressure was calculated from Eq. 2.1 for $T_i = 1100$ [℃], and was applied to the inner surface of the cavity. The temperature-dependent properties of fused quartz were obtained from COMSOL Multiphysics material

library. The FE results revealed that in some cases the maximum stress at the location of stress concentration exceeds the tensile strength of the fused quartz material, ∼50 MPa. In these cases, solid fracture occurs on the fused quartz layer before the viscous deformation was activated. Fig. 2.10 demonstrates the solid fracture map of fused quartz dies in the baseline micro-glassblowing process. The labels on the graphs indicate maximum stresses for the given combination of fused quartz thickness and outer radius. The FE results revealed that solid fracture was more likely to occur in the glassblowing of thinner and larger (in diameter) samples, which limited the fabrication of micro-shell resonators in the baseline glassblowing process. The solid fracture was also observed in the micro-glassblowing experiments. The data points of the fracture map indicate the successful and failed glassblowing geometries using the baseline process. Fig. 2.11 shows a glassblown shell using the baseline process with a diameter of 6.5 mm, device initial thickness of 400 μm, and substrate etch depth of 300μm. The backside of the substrate wafer also deforms during the process. The backside blowing is discussed in Chapter 3.

2.3.2 Vacuum Micro-Glassblowing Process

The maximum stress during the transient thermal regime is directly proportional to the instantaneous pressure of the cavity, Eq. 2.1. The cavity pressure can be reduced by wafer bonding at reduced pressure, $P_{wb} < 1$ atm. The FE simulations were repeated for the reduced wafer bonding pressures. Fig. 2.12 shows the FE results for wafer bonding at 0.6 and 0.2 atm. As expected, the lower wafer bonding pressure would reduce the maximum stress and expands the safe design region of the glassblowing process. The wafer bonding step in the vacuum micro-glassblowing process was performed in a wafer bonder under controlled pressure for successful glassblowing. The surface activation of the pre-etched substrate wafer and the "device" wafer was performed in a plasma chamber and wafers were transferred to a wafer bonding system (AML-AWB) for the wafer bonding in partial pressure.

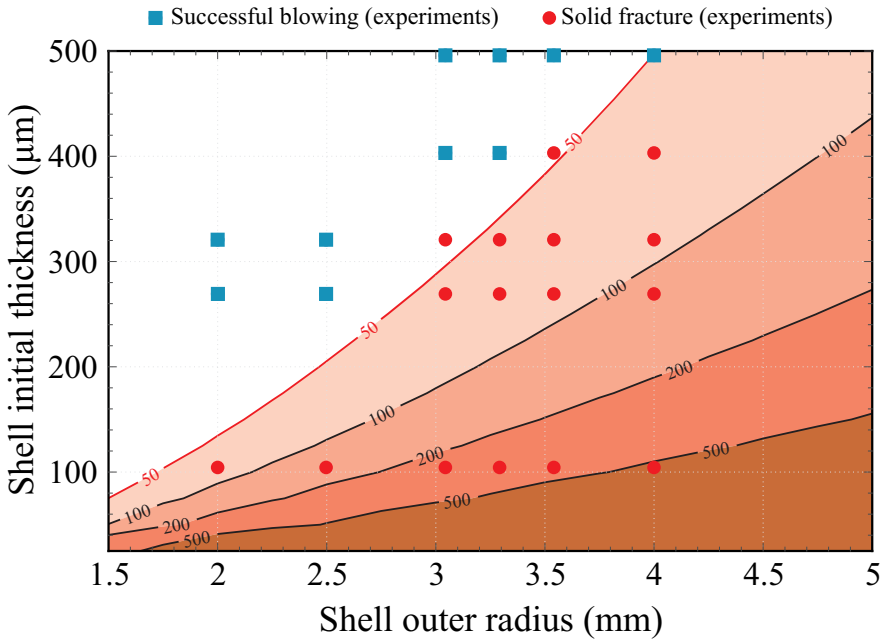

Figure 2.10: Fracture limit of fused quartz shells before the viscous deformation due to exceeding the tensile strength of fused quartz (∼50 MPa). The labels on dashed boundary lines indicate the stress level in MPa. Any combination of initial shell thickness and outer radius that results in regions with tensile stress level above 50 MP a would result in a solid fracture before glassblowing. The blue squares are the successful glassblowing experiments, and red dots represent the failed glassblowing due to solid fracture.

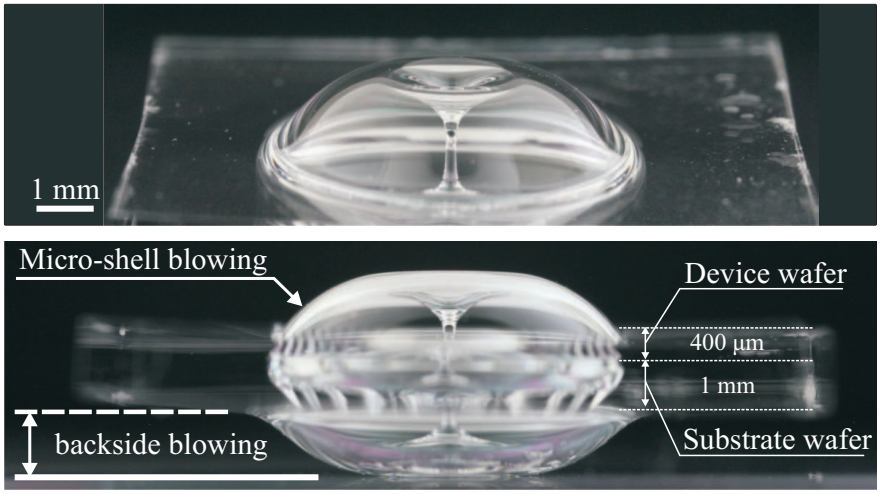

Figure 2.11: A glassblown shell using baseline fabrication process with an initial device thickness of 400 μm and diameter of 6.5 mm. A 300 μm cavity was etched on the substrate wafer with 1 mm thickness. During the glassblowing, not only the device layer but also the substrate deforms. The substrate backside blowing can be reduced by using a thicker substrate wafer.

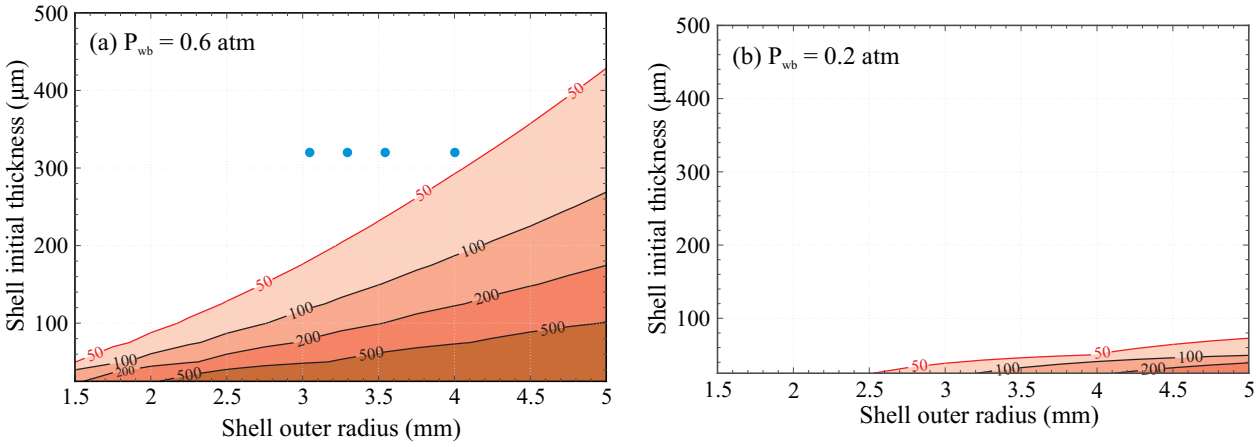

Figure 2.12: Shown are FE simulation results of maximum stress in an fused quartz die bonded initially at (a) 0.6 atm and (b) 0.2 atm. The wafer bonding in a reduced pressure expands the safe design region of the shell geometry to avoid the solid fracture before the glassblowing. The solid blue dots represent the successful experimental glassblowing at 0.6 atm ($\sim$ 450 Torr). No experiments were attempted at 0.2 atm.

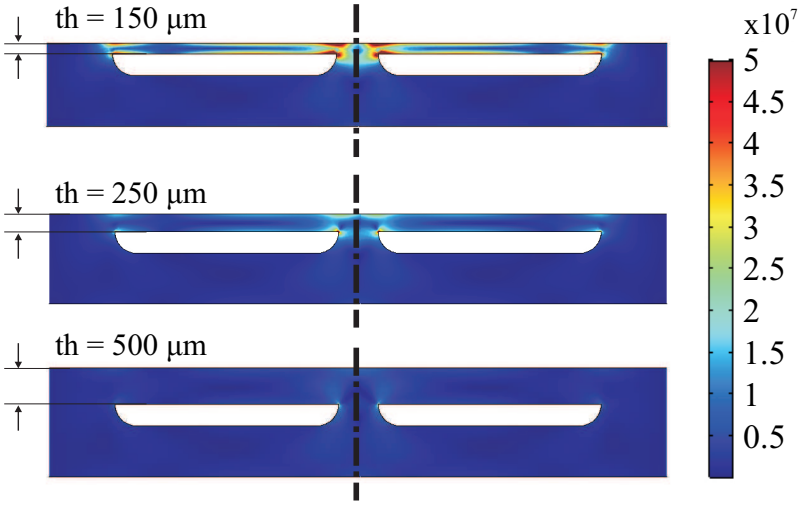

Figure 2.13: FE simulations revealed the localized concentration of stress on the edge of the encapsulated cavities, which is expected to initiate to initiate cracks and breakage of the fused quartz die in the baseline glassblowing process.

2.3.3 Reverse Micro-Glassblowing Process

Another approach to mitigate the maximum stress on the thin device layer during the glassblowing is to reduce the stress concentration. Fig. 2.13 shows the stress distribution in the fused quartz dies, demonstrating the local concentration of tensile stresses at the edge of encapsulated cavities. The stress concentration factor (K_t) depends on the geometry, and it can be mitigated by reducing curvature at the sharp edges. The reverse glassblowing process takes advantage of the round edges formed during the isotropic wet etching of fused quartz wafers. In the reverse process, the cavities were etched on the "device" wafer instead of the "substrate" wafer. Fig. 2.14 shows a cross-section of an encapsulated die, illustrating round corners on the thin side of the wafer. The pre-etched device wafers were bonded to blank substrate wafers (1 mm thick) using plasma-assisted wafer bonding under atmospheric pressure conditions. Unlike the baseline micro-glassblowing process, devices were glassblown from the cavity side, reducing the stress concentration due to round edges formed by the isotropic wet etching, Fig. 2.15. In addition, the initial thickness of the device layer depends on the device wafer thickness and the depth of isotropic etch in the reverse micro-glassblowing. Fig. 2.16 illustrates schematically the difference in geometry of fused quartz dies. From the design point of view, the initial device thickness and the cavity etch depth are independent design parameters in the baseline and the vacuum micro-glassblowing processes. On the other hand, cavity etch depth, initial device thickness, and device wafer thickness are related in the reverse micro-glassblowing process. As an example, if 300 μm cavities were etched in a device wafer with 500 μm thickness, the initial device thickness would be 200μm. If a device wafer with 400 μm thickness were used, the initial device thickness would reduce to 100μm. Thus, an additional parameter is added in the design of reverse glassblowing process for 3D micro-shell resonators. Fig. 2.17 shows a glassblown shell using the reverse process with a diameter of 7.0 mm, initial device thickness of 175 μm was achieved by etching 325 μm cavities in a 500 μm device wafer. The substrate wafer thickness was 1 mm.

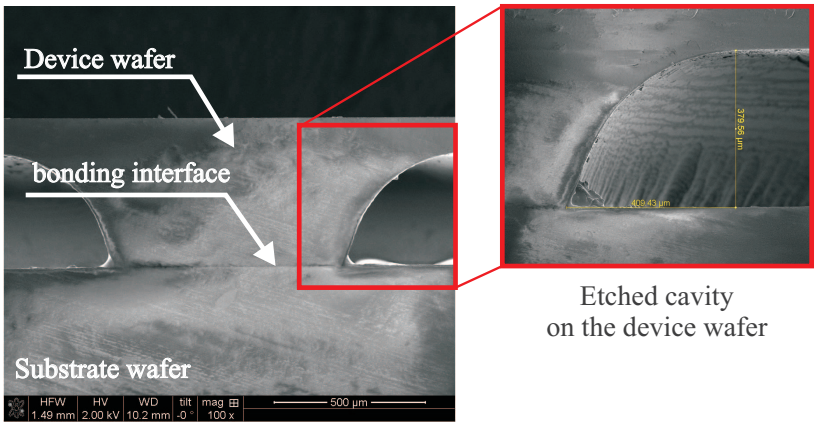

Figure 2.14: Etch profile of a cavity on the device layer showing the round corners around the perimeter of the die on the thinner side.

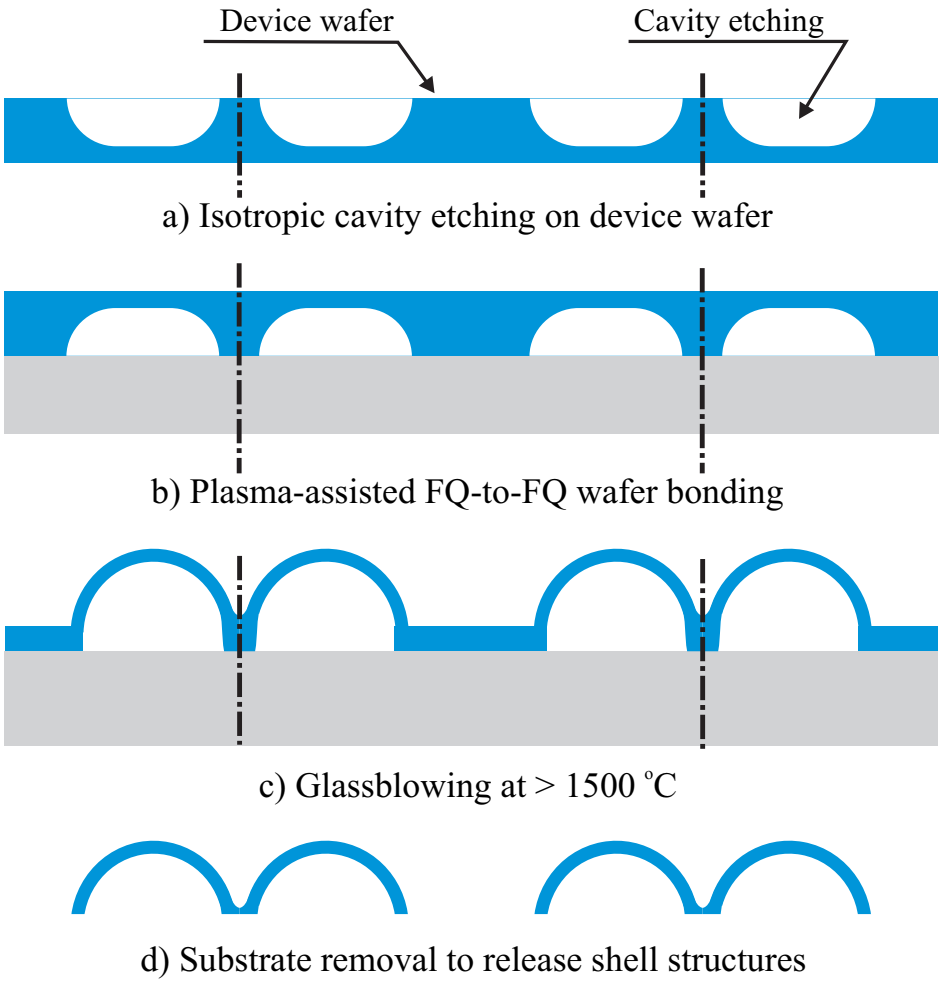

Figure 2.15: The reverse micro-glassblowing fabrication process. The round edges on the thinner side of the cavity mitigates the fracture of fused quartz die before the glassblowing.

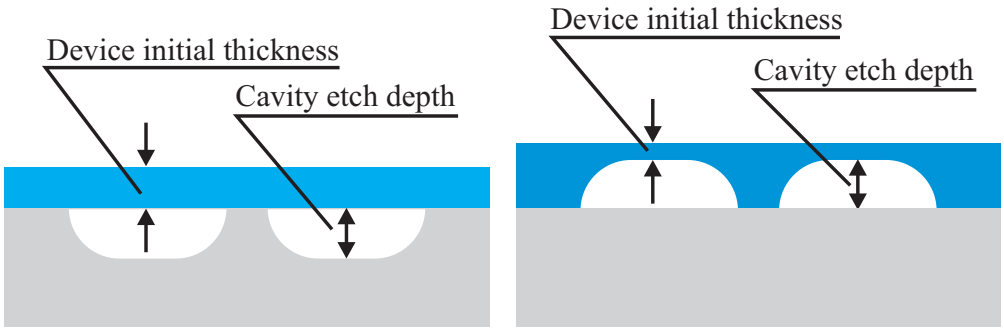

(a) Die geometry in baseline and vacuum micro-glassblowing

(b) Die geometry in reverse micro-glassblowing

Figure 2.16: Schematics of the fused quartz die geometry in different micro-glassblowing processes. The substrate wafer is shown in gray and device wafer is shown in blue. In the baseline and vacuum processes, the cavity etch depth and device initial thickness are independent design parameters. However, the etch depth and initial thickness in the reverse process are related through thickness of the device wafer.

Figure 2.17: A 7 mm glassblown shell using reverse process with the device initial thickness of 175 μm and the cavity etch depth of 325 μm, as depicted in Fig. 2.16, on a device wafer with thickness of 500 μm.

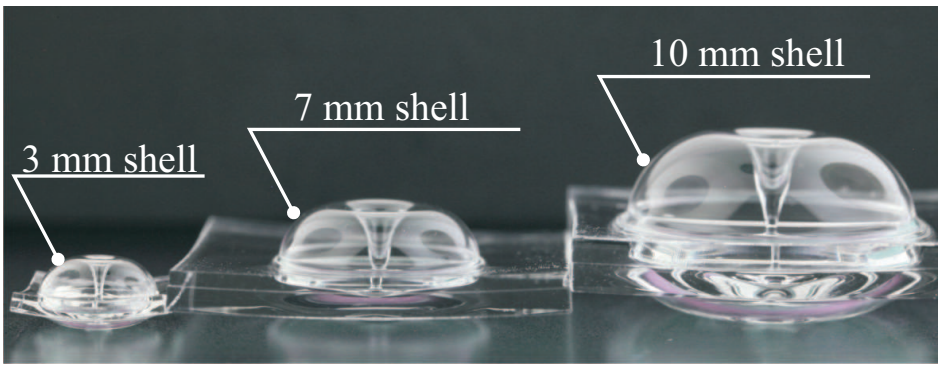

Figure 2.18: 3D fused quartz shells with different diameters (3 mm, 7 mm, and 10 mm) were fabricated using the reverse micro-glassblowing processes.

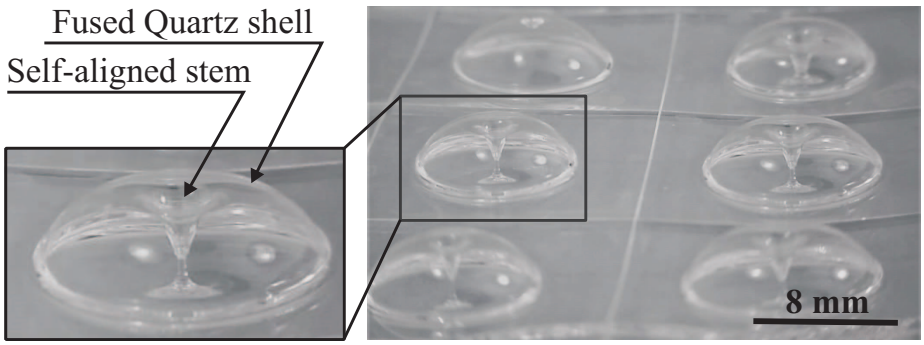

Figure 2.19: An array of Fused Quartz shells fabricated using the "reverse" micro-glassblowing process presented in this paper.

For the footprint of devices in this research, from 6 mm to 8 mm in diameter, shell resonators with higher operational frequencies, >50 kHz, were fabricated using the baseline process, and the reverse process was employed for fabrication of lower frequency shell resonators, <25 kHz. The vacuum glassblowing process was employed to fabricate shell resonators in the frequency range between 25 kHz and 50 kHz. In general, a broad range of shell geometries with a wide range of diameters and thicknesses can be fabricated with the developed micro-glassblowing methods. Fig. 2.18 demonstrates three examples of glassblown fused quartz shells with diameters of 3, 7, and 10 mm.

Fig. 2.19 shows an example of an array of fused quartz shells fabricated in the reverse micro-glassblowing process. A successful scaling of the micro-glassblowing process to the wafer-level requires a high-temperature furnace with temperature uniformity across the wafer.

Table 2.2: Detailed summary of the process steps, materials, and tools for the fabrication of 3D shell resonators using the glassblowing technique

Step	Process	Material	Tool
1	Hard mask deposition (LPCVD)	Polysilicon	Tystar 10 furnace
2	Photolithography	AZ 4600	Spn coater / MA-6 mask aligner
3	Hard mask etch (RIE)	Polysilicon	PlasmaTherm RIE
4	Cavity Etch (48% HF etch)	Fused Quartz	Wet bench
5	Hard mask removal (45% KOH etch)	Polysilicon	Wet bench
6	Wafer cleaning (RCA-1)	-	Wet bench
7	Plasma activation (O2 Plasma)	Fused Quartz	PlasmaTherm RIE
8	Wafer bonding	Fused Quartz	AML or Manual
9	Wafer dicing	Fused Quartz	DISCO 330
10	Glassblowing	Fused Quartz	MTI tube furnace
11	Lapping/Polishing	Diamond film/slurry	Allied HighTech MultiPrep
12	Sample cleaning (RCA-1)	-	Wet bench
13	Thermal annealing	Fused Quartz	Thermco Ranger 3000 furnace
14	Metal coating	Cr/Au	Angstrom Evaporator

The details of the micro-glassblowing fabrication process, including the process steps, materials, and fabrication tools are listed in Table. 2.2.

2.4 Conclusion

The micro-shell resonators with a wide variety of geometric parameters were fabricated using the proposed variations of the glassblowing process. A broad range of operational frequencies from less than 5 kHz to hundreds of kilohertz was achieved on fused quartz micro-shell resonators. In micro gyroscopes, it is often desired to increase the ring-down time, $\tau = \frac{Q}{\pi.f}$, thus lowering the operational frequency and maximizing the Q-factor are key approaches to improve the gyro performance. The frequency scaling of the operational and non-operational (spurious) resonant modes must be considered in designing a fused quartz shell resonator. Due to different scaling of different modes, the geometric parameters must be selected such that the modal frequency separation is maximized from the operational frequency of interest. In gyroscopes, it is desired to select the first resonant mode as the operational mode, and the non-operational modes to be located at higher frequencies to

reduce the environmental sensitivity and enhance the shock and vibration immunity [73]. It was demonstrated that mode-ordering could be also achieved through the design of micro-shell geometry. The effect of shell resonator geometric parameters on TED revealed that Q_{TED} changes by orders of magnitude with the resonator's thickness and diameter. Thus, it is crucial to consider the effect of resonator's geometry on TED during the design stage. The geometry optimization is an essential step in the design of micro-shell resonators to achieve a higher Q-factor and a larger separation between the operational and non-operational resonant modes. In addition, for gyro performance optimization, other parameters such as effective mass, mechanical sensitivity, and detection efficiency must be carefully selected to improve the overall performance of micro-shell resonator gyroscopes [67, 74]. The developed micro-glassblowing processes could enable a low-cost and highly-flexible fabrication of high-Q fused quartz micro shells, which can be implemented as a core sensing element with a compact form factor in microresonators and Coriolis vibratory microgyroscopes for precision navigation and timing applications.

Chapter 3

Modeling of Micro-Glassblowing Process

3.1 Introduction

The explored design space provides a set of parameters for the shell geometry at the operational frequency of interest. However, during the glassblowing process, the shell undergoes a severe deformation. Thus, it is crucial to determine the initial thickness of the fused quartz dies before glassblowing to achieve the intended final geometry. In addition, the thickness variation is inevitable in the glassblowing process. Because of the deformation gradient, the shell is thinner at the top and thicker around the rim area. Fig. 3.1 shows the thickness measurement at the cross-section of a glassblown shell with an initial thickness of 110μm. The measurements revealed that the shell thickness at the rim is $\sim$90μm, but at the top is $\sim$60μm.

Although the shell thickness was assumed to be uniform in the parametric FE modal analysis, the design space provides an insight into the shell geometry design optimization. For a more

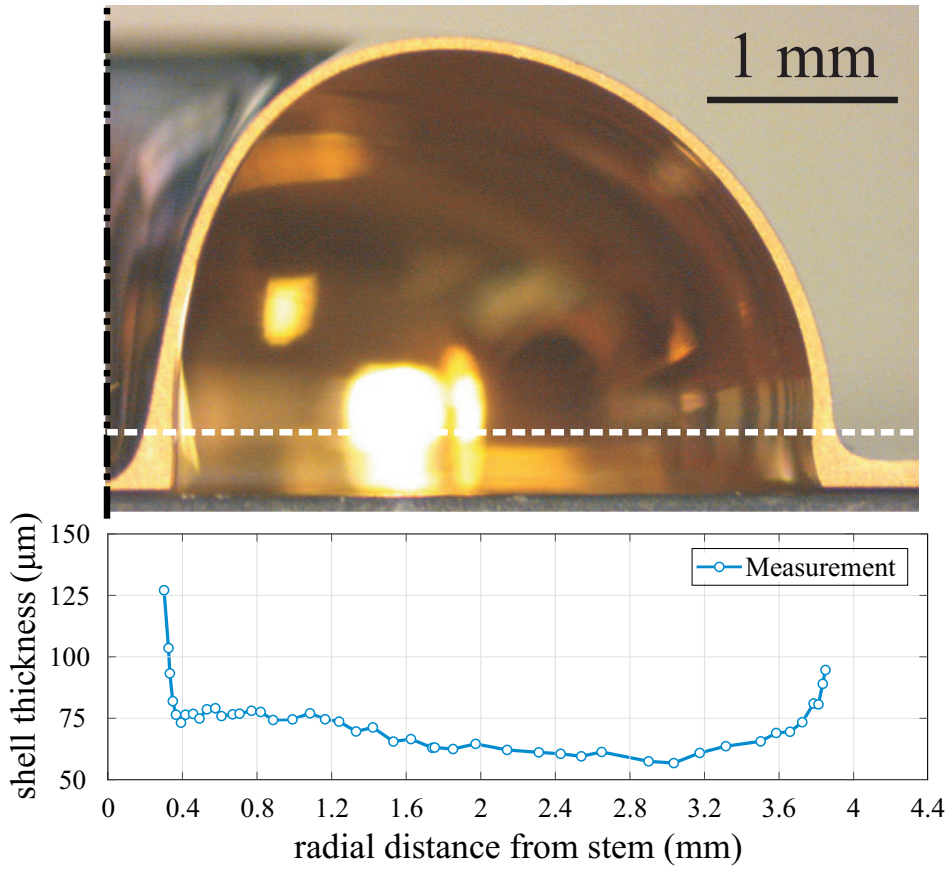

Figure 3.1: (Top) cross-sectional view of an 8 mm shell in diameter with an initial thickness of 110 μm, (bottom) thickness measurement at the cross-section. Due to different deformation rates, the top portion of the shell is ~30% thinner than the rim. (Note: the measurement data was obtained at the cross-section above the dashed white line).

accurate estimation of the n=2 wineglass frequency and modal frequency separation, a model was developed to simulate the micro-glassblowing process and to predict the final geometry. The developed FE model captures the variation in thickness. Therefore, it provides a more accurate geometry of the glassblown shells.

The final shell geometry in the micro-glassblowing process depends on the process parameters as well as geometric design parameters. In this chapter, a Finite Element (FE) model is presented to simulation the process of glassblowing of shell resonators. The presented model was used to predict the final geometry of shell resonators based on the design and process parameters. The knowledge of the final geometry of shell resonators is necessary to optimize the 3D shell geometry, and the fabrication parameters to (1) achieve the desired operational

frequency, (2) reduce the energy dissipation through the optimal geometric design, and (3) reduce the environmental sensitivity through ordering the resonant modes.

In the "flat" 2D MEMS gyroscope development cycle, a layout of structure can be imported to commercially available FE software packages for an estimation of the resonant frequencies and energy dissipation through TED and anchor loss. Although due to the fabrication imperfections, the geometry of a fabricated sensor would slightly vary from the designed layout, it would still serve a useful purpose for design optimization. The lack of such a design optimization workflow for 3D micro-glassblown shell structures had pushed an experimental-based approach for design optimization (ad-hoc methods). Although the micro-glassblowing process is scalable and an array of shell resonators can be fabricated on a wafer-level to reduce the cost and time of fabrication, the experimental-based approach is not viable. A numerical model that simulates the micro-glassblowing process and the glass re-flow was crucial in the design stage of shell resonators. Although a few simplified models were proposed to predict the height of glassblown shells analytically [75], they mostly failed to consider other aspects of a glassblown shell, such as the non-uniform thickness distribution, different stem configurations, and the effect of backside wafer buckling on the final geometry. Once an accurate model is developed to simulate the process, the effect of a variety of processes and design parameters can be investigated without going through trial-and-error experiments. In this chapter, the FE framework for simulation of the micro-glassblowing process, estimation of frequency and damping properties, and estimation of resonator's response to transient dynamic loads are discussed.

3.2 Iso-Thermal Fluid Flow Model

The simulation of micro-glassblowing requires a detailed understanding of the process to include the essential physics of the process and avoid unnecessary complexities into the model. The glass reflow process occurs in a high-temperature furnace at a preset temperature. Fused

quartz dies is transferred into the furnace using a guided flange and placed in the uniform heat zone inside the furnace. The glass undergoes transient and steady-state thermal stages. During the transient process, the temperature rises quickly (> 25 deg/sec) to reach the pre-set furnace temperature, which is above the softening point of the glass. At this stage, we assume that the glass remains in the solid phase and the viscous deformation is negligible. In addition, the pressure inside the encapsulated cavity rises with temperature until it reaches its maximum value. The maximum internal pressure depends on the process temperature and the wafer bonding pressure. In the steady-state thermal condition, the temperature is reached above the softening point of the material, defining the pressure difference between the encapsulated cavity and the pressure within the glassblowing furnace. Thus, triggering the viscous flow of the glass. The glass material deforms and the shell starts to develop. The built-in pressure difference between the internal and external surface, initiates the viscous flow; the surface tension and viscous forces act against the deformation and minimize the surface energy. The steady-state thermal stage is assumed to be isothermal. Unlike glass molding processes where the mold causes a considerable temperature gradient within the glass, and the process should be modeled as a non-isothermal fluid flow [76], the glassblowing in a high-temperature furnace creates a minimal temperature gradient, which makes the iso-thermal model a valid assumption.

The process was simulated with a Newtonian isothermal incompressible fluid flow model using COMSOL Multiphysics FE package. The temperature-dependent material properties of fused quartz were obtained from [77] to explore the effect of glassblowing temperature in the simulations. A 2D axisymmetric model was employed to simulate the micro-glassblowing of shell resonators. Fig. 3.2 illustrates the finite element model of fused quartz die in the initial configuration. The device layer and the substrate layer were modeled as incompressible fluid domains with assigned density and viscosity. The gravity was applied as a volume force to the viscous domains. The outer and the inner boundaries of the cavity were modeled as a free surface with assigned surface tension. A constant ambient pressure (pressure of the

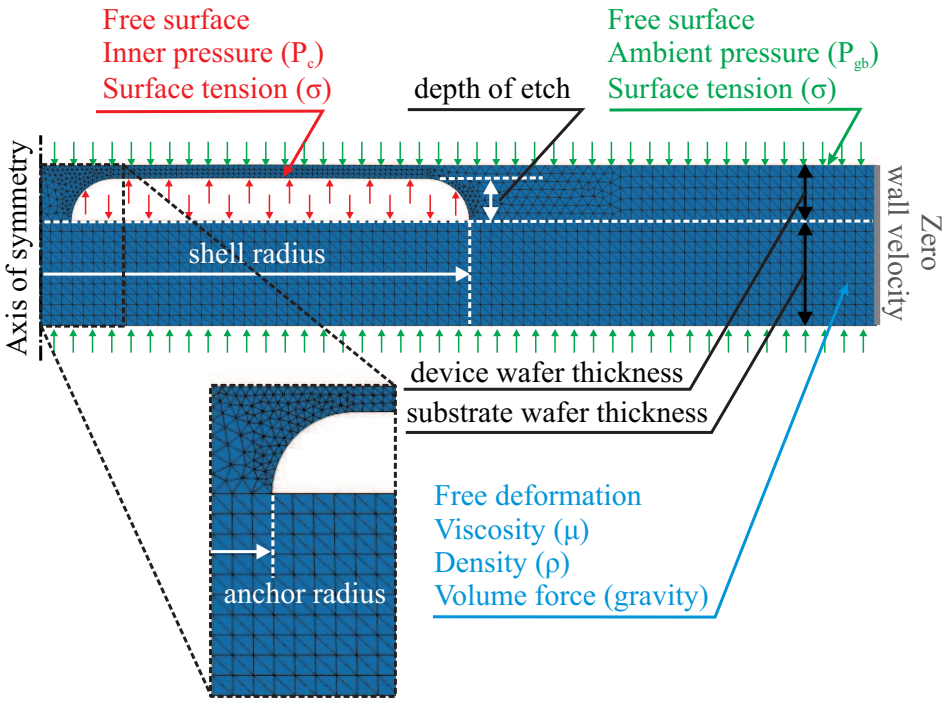

Figure 3.2: Finite element model of the glassblowing process. The device layer and substrate layer were modeled as incompressible fluid domains. The geometric design parameters, including shell radius, anchor radius, depth of etching, and wafers thickness are indicated, as well as the boundary conditions.

glassblowing furnace) was applied on the outer boundaries, and a time-dependent pressure was applied on the inner cavity boundaries. The zero wall velocity was applied to the outer most boundary of the domains. For glassblowing simulation at 1550 ℃, the fused quartz was modeled as a viscous material with viscosity (μ) and surface tension (σ) of 1.58×10^7 [Pa.s] and 0.295 [N/m], respectively.

In the modeling of the glassblowing process, some details were neglected. The radiative and convective heating of the fused quartz die inside the furnace were not considered in the model. In experiments, the fused quartz dies inside the furnace were isolated from the outside environment to minimize the temperature gradient caused by conductive heat transfer. The thermal isolation of the crucible reduces the non-uniformity in the temperature distribution across the fused quartz die. Thus, the heat transfer boundary conditions were not applied in the current model. However, a perfect isolation is not practically feasible,

and a temperature gradient always exists across the loading crucible, which may influence the glassblowing process. Finally, the viscoelastic effect during the heating and cooling of fused quartz dies (when the temperature is near the strain point of glass) was also neglected. Since the viscosity of fused quartz has an Arrhenius-type temperature dependency [77], most of the micro-shell evolution would occur when the temperature has reached its maximum. Thus, neglecting the transient regimes in the simulations would not significantly change the final results. For future simulations, a 3D model has to be developed to account for the non-uniformity in temperature in predicting the asymmetric glassblowing.

3.2.1 Governing Equations

In the isothermal model for incompressible fluid flow, the viscosity and density of the glass were given as constants in the model. The partial differential equations that describe the conservation of mass and momentum (transport equations) form the governing equations of the fluid flow problem [78]. The solution of the transport equations will give the velocity vector ($\mathbf{v}$) and the fluid pressure (p) of the domains at any time instances. The conservation of mass for an incompressible fluid flow problem gives the equation of continuity in the following form:

$$\nabla \cdot \mathbf{v} = 0 \tag{3.1}$$

The conservation of momentum (Navier-Stokes momentum equation) gives the equation of motion in the following form:

$$\rho(\partial \mathbf{v}/\partial t + \mathbf{v} \cdot \nabla \mathbf{v}) = \nabla \cdot [-p\mathbf{I} + \mu(\nabla \mathbf{v} + (\nabla \mathbf{v})^T)] + \rho f, \tag{3.2}$$

where f represents body accelerations acting on the domains such as gravity or inertial accelerations, and ρ is the fluid density.

3.2.2 Boundary Conditions

The "wall" boundary condition with zero velocity was applied to the far-end boundary of the fused quartz die to confine the fluid flow problem. A pressure boundary condition and surface tension were assigned on all free surfaces of the fluid. The normal and tangential stress at free surfaces with an external pressure must be balanced by forces associated with the surface tension gradient. The stress balance equation on the free surfaces takes this form:

$$\mathbf{n} \cdot T = -P_{ext} \cdot \mathbf{n} + \sigma \cdot \mathbf{n}(\nabla_s \cdot \mathbf{n}) - \nabla_s \sigma, \tag{3.3}$$

where, $\mathbf{n}$ represents the unit outward normal vector to the surface, T is the viscous stress tensor ($T = -p\mathbf{I} + \mu(\nabla \mathbf{v} + (\nabla \mathbf{v})^T)$), $\mathbf{n} \cdot T$ represents the stress on the interface (with normal and tangential components), P_{ext} is the applied pressure on the interface boundary, σ is the surface tension, and ∇_s is the tangential gradient operator. The second term on the right-hand side of Equation 3.3 is the normal curvature force (per unit area) associated with local curvature of interface ($\nabla_s \cdot \mathbf{n}$), and the third term is the tangential stress associated with gradients in surface tension.

The boundary value of the pressure on the outer free surfaces of the fused quartz die was a constant pressure, which represents the ambient pressure of the glassblowing furnace (P_{gb}). In the baseline and reverse processes, the glassblowing was performed at the atmospheric pressure. In the vacuum process, the glassblowing was performed at a reduced, but constant, pressure using a vacuum tube and a mechanical roughing pump. A time-dependent pressure boundary condition was applied on the inner boundary of the encapsulated cavity. The initial boundary pressure, P_i, was calculated based on the glassblowing process temperature, wafer bonding pressure, and wafer bonding temperature from Eq. 2.1.

The glassblowing model was numerically solved in COMSOL Multiphysics with zero initial values. User-defined functions and variables were implemented to capture the self-limiting characteristic of the glassblowing process. As the shell deforms due to the differential pressure, the cavity volume, V_c, increases. The internal cavity pressure, P_c, was calculated according to the ideal gas law with an isothermal assumption:

$$P_c = \frac{P_i V_{pc}}{V_c}, \tag{3.4}$$

where, V_{pc} is the volume of the pre-etched cavity, and applied on the inner boundary of the encapsulated cavity. The time-dependent pressure boundary condition required an instantaneous calculation of V_c at every time step. This was done by calculating the surface integral on the enclosed boundary of the cavity. The applied boundary pressure was continuously calculated at each time step. As the shell geometry continues to develop, the pressure difference between the inner and outer boundaries decreases until it reaches an equilibrium state, $P_c = P_{gb}$, and deformation stops. An automatic adaptive re-meshing technique was applied to limit the maximum mesh distortion and to ensure the mesh quality, as the fused quartz layer undergoes large viscous deformations.

3.2.3 Baseline Micro-Glassblowing Process

In the baseline glassblowing process, a pre-etched substrate was bonded to a device wafer at atmospheric pressure and temperature, $P_{wb} = 1$ atm and $T_{wb} = 300$ K, resulting in the internal pressure of $P_i \sim 6.2$ atm (90 psi) at the beginning of the glassblowing. The pressure was applied on the inner surface of the cavity while the outer surfaces of the die (top and bottom) were subjected to atmospheric pressure. Due to the axial symmetry of the cavities, a 2D axisymmetric model was utilized for the simulations. Fig. 3.3 illustrates the applied boundary conditions of the FE model. Fig. 3.4 illustrates the geometry of the simulated and fabricated glassblown shell in the baseline process.

The free surface boundary condition on the substrate surface captures the backside blowing during the process. The time-dependent cavity pressure, the shell height, and the backside blowing height are plotted as a function of simulation time in Fig. 3.5. The shell structure deforms until the pressure inside the cavity reaches an equilibrium state with the furnace ambient pressure, P_{gb}, demonstrating the self-limiting nature of the micro-glassblowing process. The backside blowing would reduce the height of the device shell, and is inevitable in the glassblowing when the same material is used as the substrate and the device wafer. The deformation in the substrate side of the fused quartz die can be reduced if thicker substrates were used to etch the cavities. The inset figure in Fig.3.5 illustrates that the shell would blow 50% higher when a 2 mm thick substrate wafer as used instead of a 1 mm thick wafer. Fig. 3.6 demonstrated the simulation results when a substrate wafer with a thickness up to 4 mm was used for pre-etching 300μm cavities. The thicker substrate mitigates the backside blowing; however, it complicates the subsequent substrate removal to release the shell resonators.

3.2.4 Vacuum Micro-Glassblowing Process

The height of a glassblown shell depends on the volume of the pre-etched cavity, V_{pc}, glassblowing temperature T_{gb}, wafer bonding pressure P_{wb}, and the glassblowing furnace pressure P_{gb}. In the vacuum micro-glassblowing process, the wafer bonding in partial vacuum mitigates the solid stress in a die. Consequently, it reduces the internal pressure during the glassblowing process, hence, reduces the height of the glassblown shells. The glassblowing in the vacuum would increase the pressure difference between the cavity and ambient, recovering the height of glassblowing. Fig. 3.7 illustrates the height of a shell with 200 μm thickness bonded under a reduced pressure, P_{wb} = 0.6 atm, at different furnace ambient pressures, P_{gb}. These results demonstrate that vacuum micro-glassblowing requires wafer bonding and glassblowing in a partial vacuum to fabricate fully-blown FQ shell resonators.

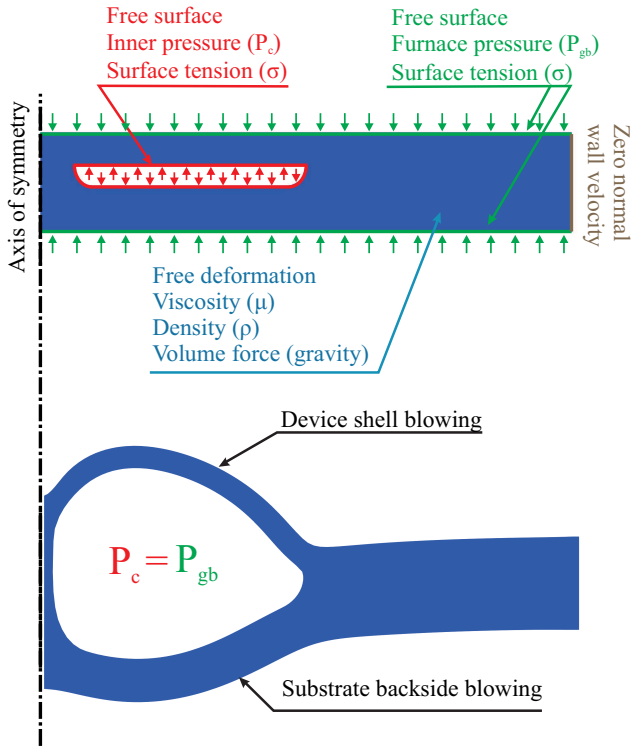

Figure 3.3: Schematics of the FE model for simulation and final geometry of a shell in the baseline glassblowing with anchor radius of 500 μm, shell radius of 4 mm, and cavity etch depth of 300 μm of the substrate wafer.

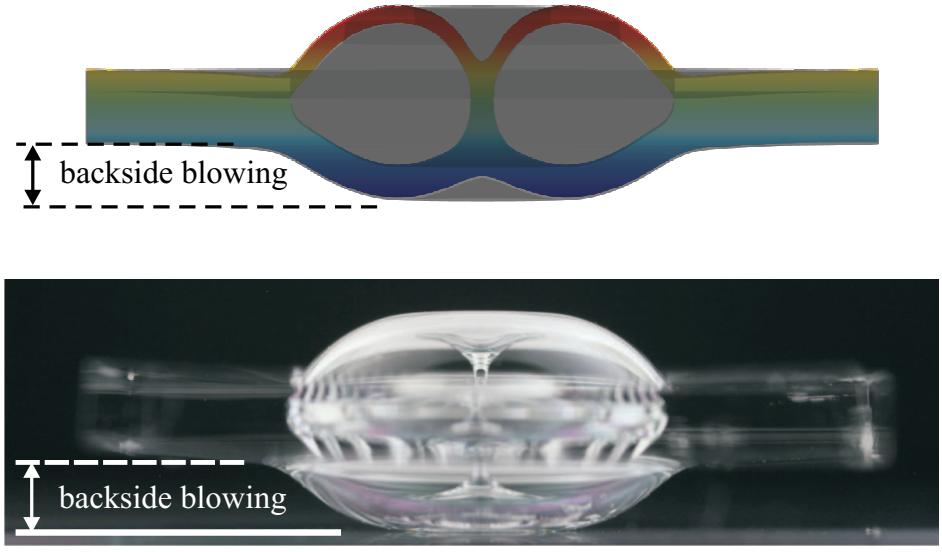

Figure 3.4: Simulation result of the "baseline" glassblowing. The simulation predicts the final geometry prediction of a glassblown shell, as it was shown in Fig. 2.11, with 400 μm anchor radius, 4 mm shell radius, 400 μm device wafer thickness, and 300 μm cavity etch depth.

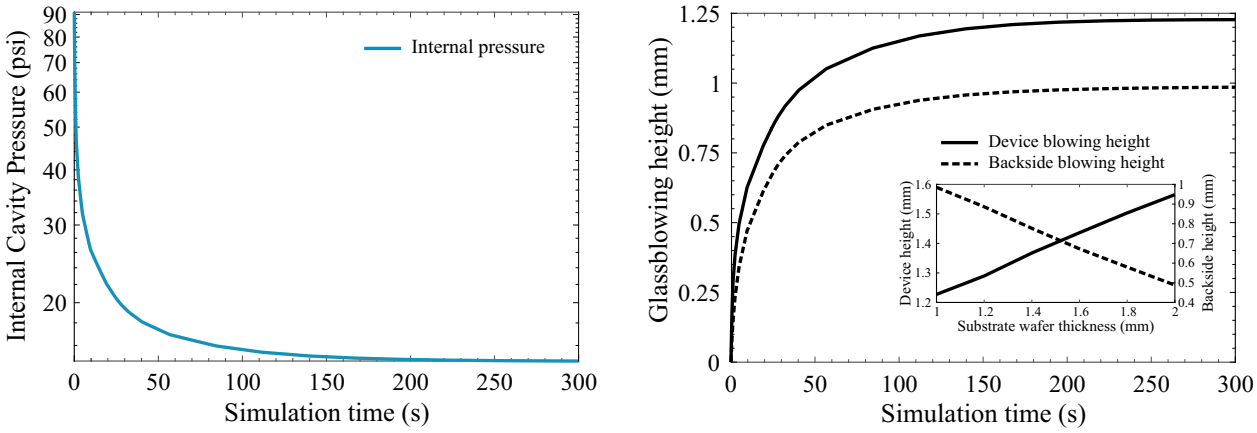

Figure 3.5: Illustration of the self-limiting characteristics of the micro-glassblowing process. As the pressure (solid blue line) drops and reaches an equilibrium state with the ambient, the shell deformation rate decreases and limits the shell height (solid black line). The backside of the substrate also blows (dashed black line). The inset figure shows that by using thicker substrate wafers, the backside blow reduces and the shell height increases. Simulations were performed for an 8 mm diameter shell with 500 μm initial thickness and 500 μm anchor radius.

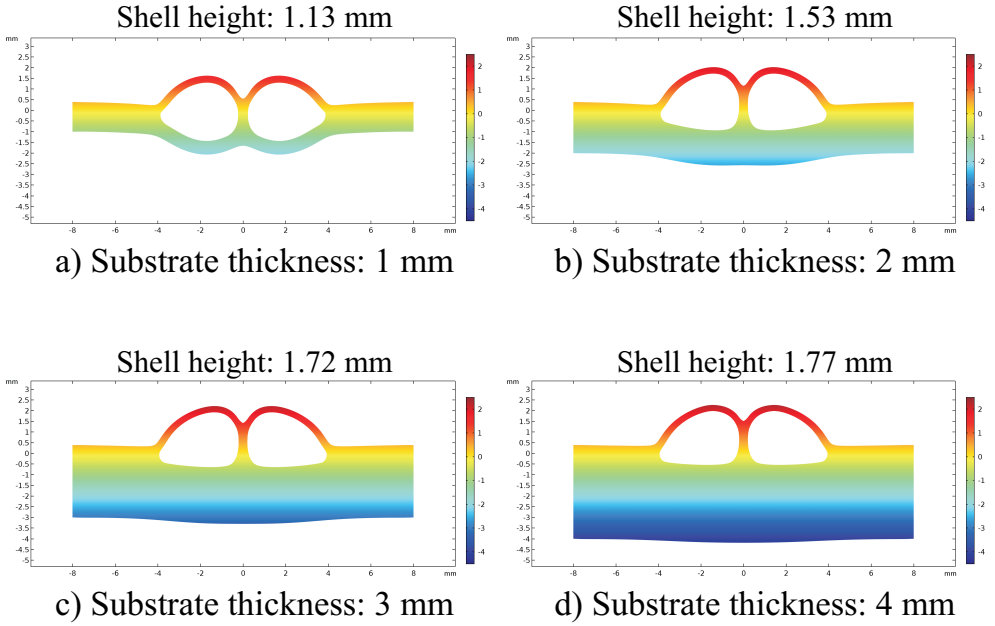

Figure 3.6: Simulation results of backside blowing in the baseline process with different substrate thicknesses. The thicker substrate reduces the backside blowing, which results in higher-blown shell geometries. Simulation parameters are: 400μm device thickness, 300μm cavity depth of, 600 μm anchor radius, and 4 mm shell radius.

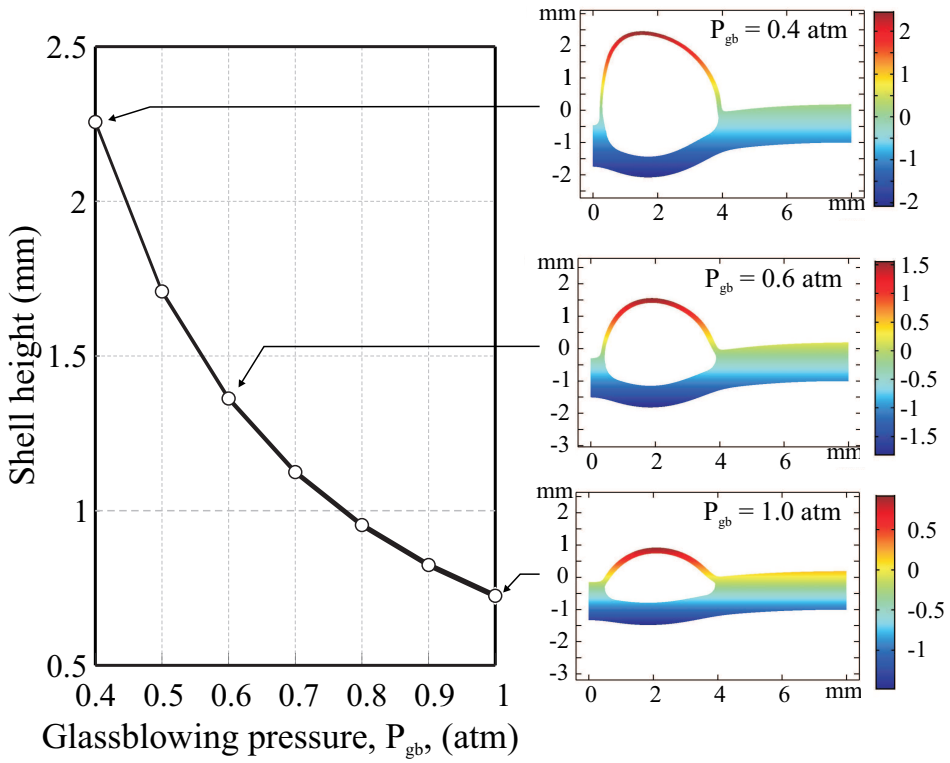

Figure 3.7: Glassblowing height of a 200 μm shell bonded in a partial pressure (P_{wb} = 0.6 atm) under different furnace ambient pressures, P_{gb}. The glassblowing in atmospheric pressure would result in an under-blown shell. The glassblowing should be performed at reduced pressure in a vacuum tube to fabricate fully-developed shells, .

The micro glassblowing furnace was equipped with a vacuum tube and a mechanical roughing pump. The pressure inside the vacuum tube could be controlled using a vent and a gate valve on the sliding flange assembly, Fig. 3.8. The shell resonators can be fabricated in the vacuum glassblowing process at the expense of process complexity.

3.2.5 Reverse Micro-Glassblowing Process

The vacuum micro-glassblowing process reduces the maximum stress concentration and fracture of thin device layers at the cost of increased process complexity. The reverse process enables fabrication of shell resonators without any requirements on controlling the wafer bonding pressure and glassblowing ambient. Fig. 3.9 demonstrates the shell height development in the reverse glassblowing process of a shell with an initial thickness of 100 μm and

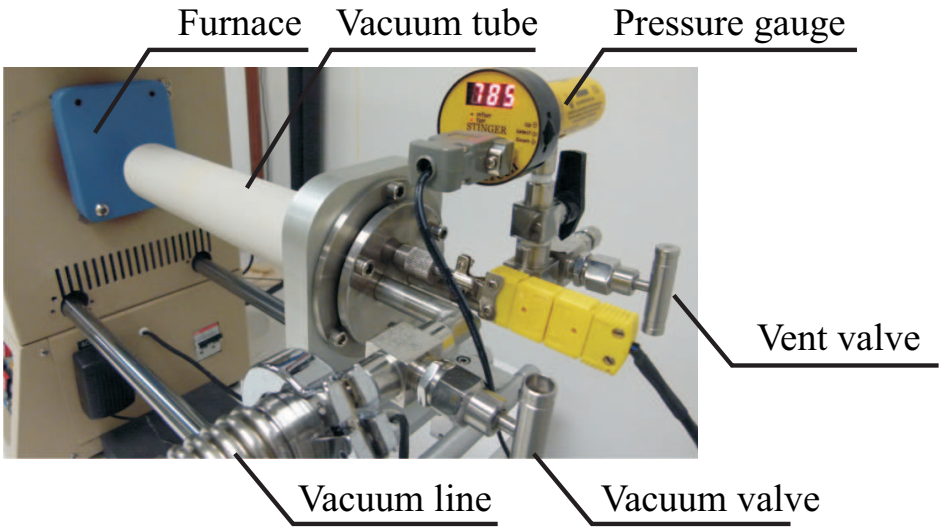

Figure 3.8: A vacuum tube was added to the micro glassblowing furnace with controlled pressure to perform the vacuum glassblowing process.

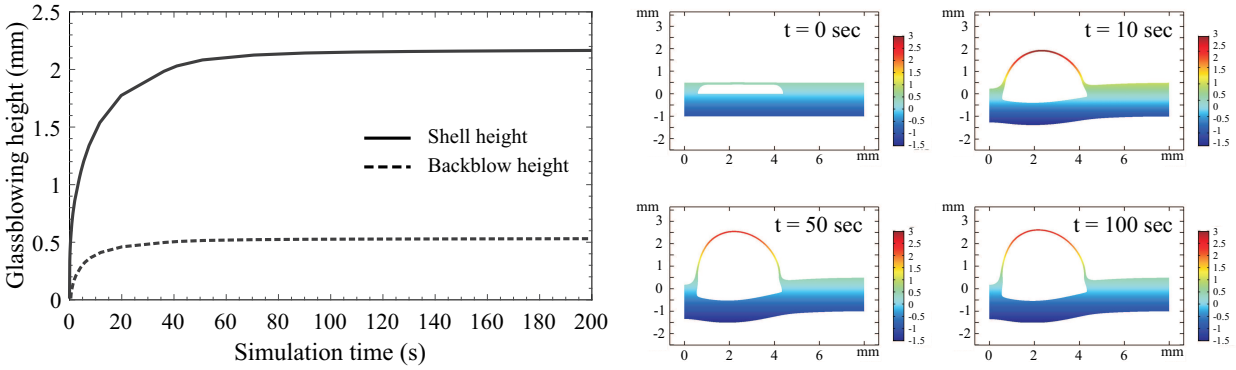

Figure 3.9: Simulation results of shell height development in the reverse glassblowing process in a shell with initial thickness of 100 μm. A higher glassblowing height and lower backside blowing is expected in the reverse process compared to the baseline process.

shell outer radius of 4 mm.

As discussed in Chapter 2, the initial thickness of the device in the reverse process is defined from the wafer thickness and depth of pre-etching, Fig. 2.16. In one configuration, the cavities can be time-etched to achieve different initial device thicknesses. Fig. 3.10 illustrates the final geometry and calculated shell height for the reverse glassblowing process simulation with four different etch depths. The shell with 450 μm depth of etching would blow higher. In the other configuration, for a fixed depth of etching, different wafer thicknesses would

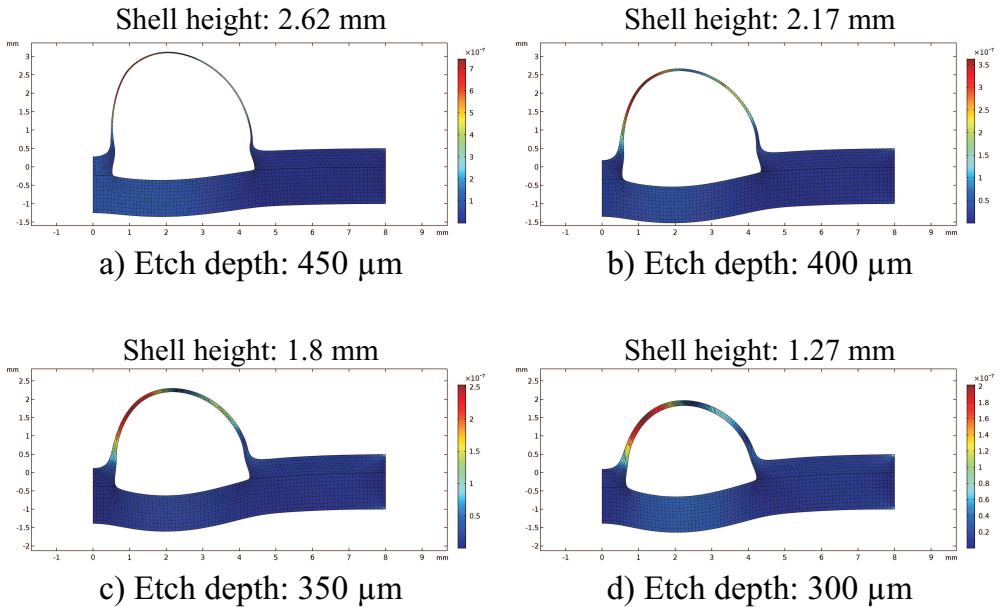

Figure 3.10: Simulation results of the glassblowing height in the reverse glassblowing process with (a) 450 μm, (b) 400 μm, (c) 350 μm, and (d) 300 μm depth of etching on a 500 μm thick device wafer. The volume of the pre-etched cavities can be design to adjusted the height of glassblown shells.

result in the different device initial thicknesses. Fig. 3.11 illustrates the final geometry and calculated shell height for four different cases. The results revealed that the heights of glassblown shells were (nearly) identical. A broad range of shell thickness and height can be selected based on a combination of depth of etching and wafer thickness.

3.3 Post-Processing of Fluid Flow Simulation Results

The post-processing of the results of the fluid flow simulations was performed to reconstruct the 3D geometry of shell resonators. COMSOL Multiphysics was used for post-processing purposes. The results of the fluid flow at the final time step of the simulation were exported to the solid mechanics model. The 3D shell geometry was employed in further numerical simulations, such as modal analysis, estimation of TED and anchor loss, and transient dynamic analysis. Fig. 3.12 illustrates the post-processing steps. First, the fluid dynamics mesh at the final time step of the glassblowing simulation was imported to the geometry editor of

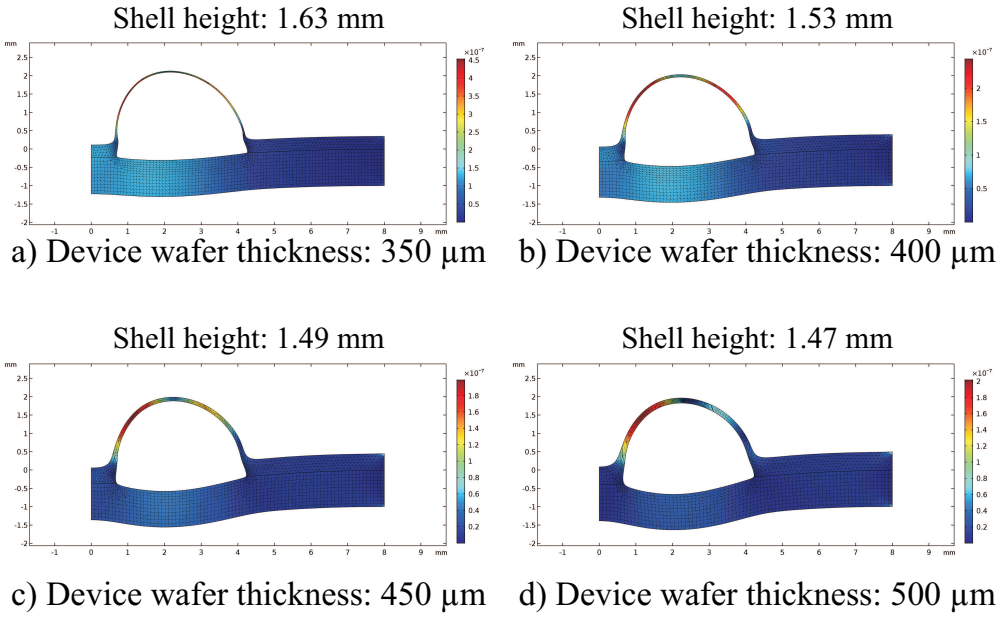

Figure 3.11: Simulation results of the glassblowing height in the reverse glassblowing process with 300 μm depth of etching on device wafers with (a) 350 μm, (b) 400 μm, (c) 450 μm, and (d) 500 μm thickness, the glassblown shell heights are (nearly) identical since the volume of pre-etched cavities were identical. A slightly larger backside blowing occurs in dies with a thicker device side.

the modal analysis module. Second, the substrate part of the mesh was trimmed away using the geometry editing tools in the 2D sketch plane. The 3D geometry was reconstructed by revolving the 2D trimmed mesh around its axis of symmetry. Third, the material properties of solid fused quartz were assigned to the 3D domain, the fixed boundary condition was applied to the central stem, and the geometry was meshed using swept meshing method. Finally, the resonant modes and modal frequencies were solved for the 3D shell model.

Similarly, the transient dynamic analysis was performed on the reconstructed 3D geometry of shell resonators. As an example, an external shock was applied on the shell resonators as a body acceleration using a half-sine function with the amplitude and duration of the shock. The displacement, mechanical stress, and frequency shift of the resonators under different shock amplitude and duration were simulated. Fig. 3.13 illustrates the results of in-plane and out-of-plane shock simulations with 50,000g amplitude and duration of 10 ms. The results of transient dynamics can be employed toward optimization of the geometry of shell

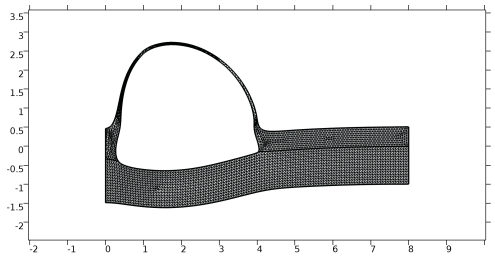

1) Import Fluid Mesh

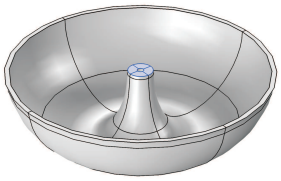

2) Construct 3D Model

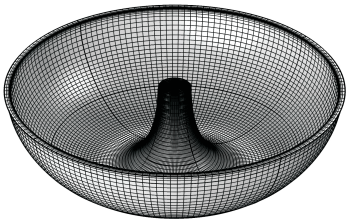

3) Assign Solid Properties and Mesh

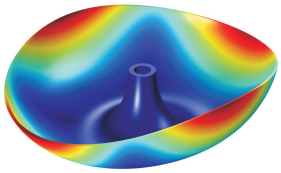

4) Modal Simulation Results

Figure 3.12: The post-processing steps to transfer the results of the fluid flow model to the solid mechanics simulations: (1) import the final mesh of the fluid flow model as a geometry in the geometry editor and trim the substrate, (2) construct the 3D shell geometry and apply fixed boundary condition, (3) assign the mechanical properties of solid fused quartz material and mesh the geometry, and (4) solve for the mode shapes and resonant frequencies.

resonators and the design of capacitive gaps for the electrostatic operation of resonators.

3.4 Design for Ordering of Modal Frequencies

Pre-pattering of the fused quartz device layer before glassblowing was presented as an approach to reduce the resonant frequency of the n=2 wineglass modes while keeping the spurious modes at higher frequencies [79]. A patterned glass layer before shell formation in blowtorch molding process was demonstrated to control the stiffness and mass distribution of shell resonators [76]. To explore the effect of pre-patterned fused quartz device layer on the glassblown shells, an isotropically etched annular ring was added to the FE model of FQ glassblowing, as shown in Fig. 3.14a. In simulations, the shell diameter was 7 mm, stem diameter was 1.4 mm, the cavity depth of etching was 400 μm, and the inner radius of the annular ring, r_r, was 3 mm. The depth of annular etch was changed from 0 to 50 μm. The

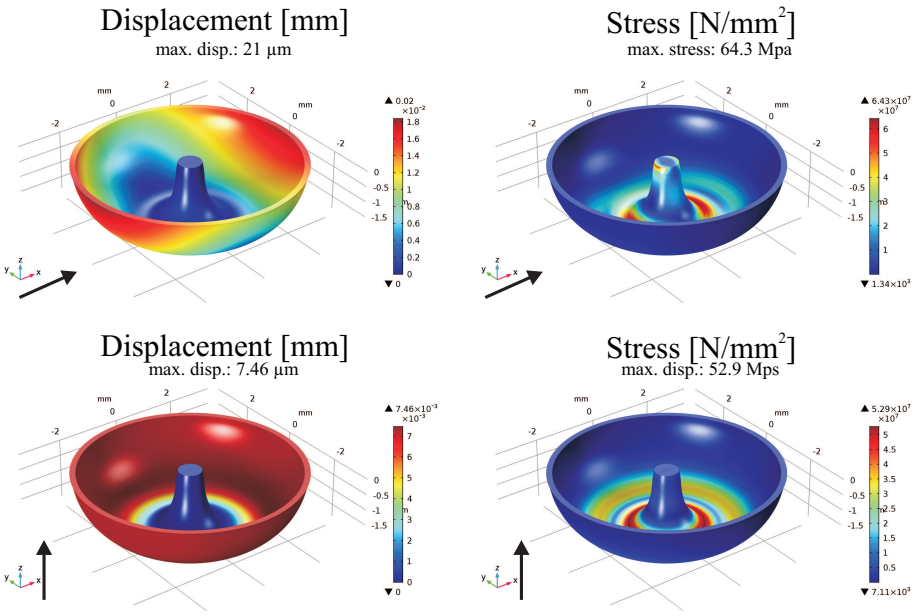

Figure 3.13: An example of shock response of a shell resonator with n=2 resonant frequency of 11 kHz, under a half-sine in-plane and out-of-plane shock input with 50,000g amplitude and 10 ms duration. The black arrow indicates the direction of applied shock.

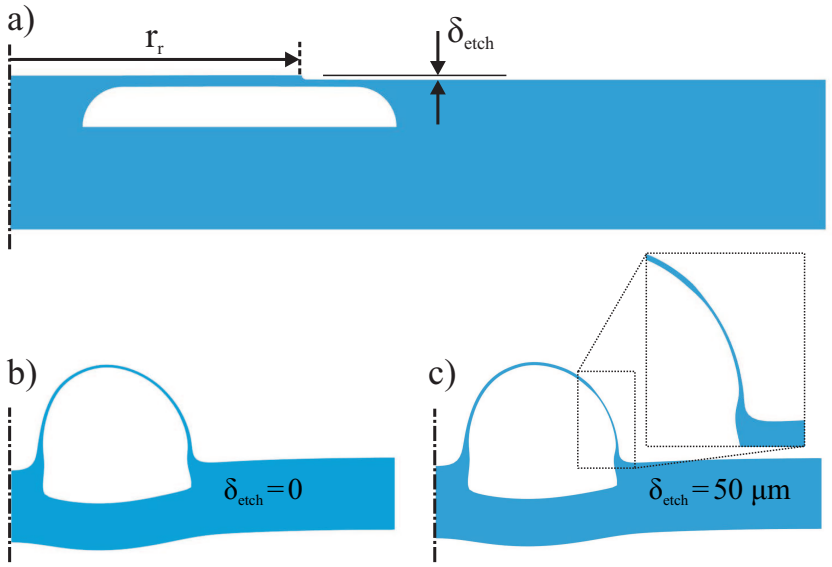

Figure 3.14: The modified model of FQ die with added annular pattern. (a) the final glassblown geometry without patterning the FQ, (b) and pre-patterning with $\delta_{etch} = 50$ μm. The shell thickness distribution changes as the result of pre-patterning of FQ before glassblowing.

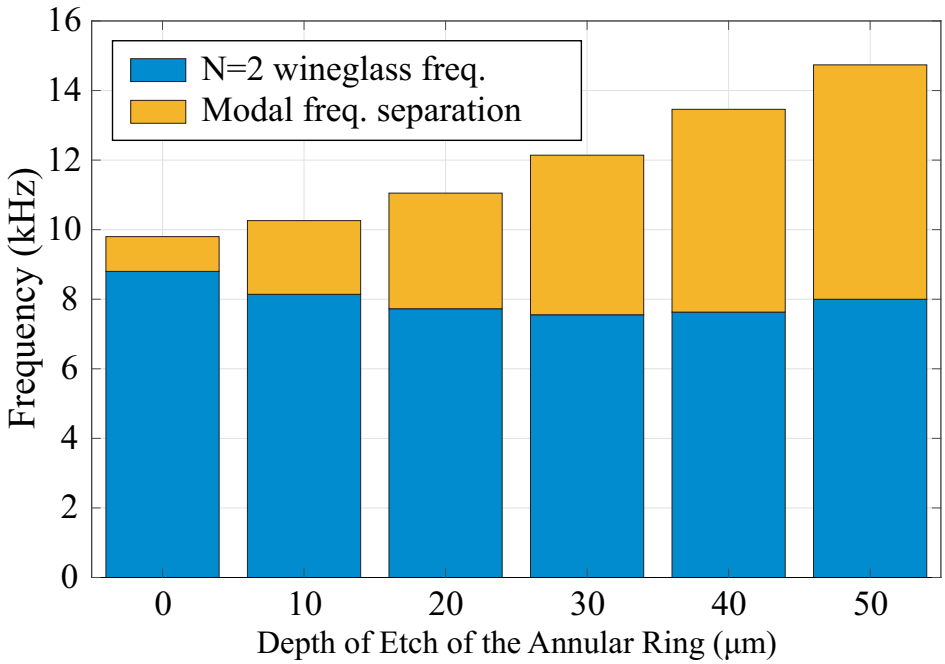

Figure 3.15: n=2 wineglass resonant frequency and minimum modal separation in a micro-glassblown FQ shell resonator with different annular ring designs. A 6× improvement in the modal separation was predicted as a result of geometry modification.

geometry of glassblown FQ shell for the cases of 0 and 50 μm are shown in Fig. 3.14b and Fig. 3.14c, respectively.

Fig. 3.15 demonstrates the effect of patterned fused quartz on the n=2 wineglass resonant frequency and its separation with the closest spurious mode. The selective reduction of shell thickness around the rim area would reduce the wineglass frequency. Moreover, it would change the overall thickness distribution of glassblown shells and stiffen the tilt and out-of-plane modes, which is anticipated to improve environmental immunity of shell resonators operating at low frequencies.

3.5 Conclusion

The glassblowing process was numerically simulated with an isothermal fluid flow model. The primary purposes of the glassblowing simulation were to predict the final geometry of glassblown micro-shells based on the design and process parameters and to perform modal

and transient dynamic analysis to determine the resonant frequencies and response to external shock and vibrations. The simplified model of the glassblowing process only simulated the steady-state thermal stage of the glassblowing and considers the fused quartz at high-temperature as a viscous fluid with constant properties, such as viscosity, surface tension, and density. The predictions of the fluid flow and mechanical simulations were nearly-matched with the experimental results with less than 10% discrepancy. The presented model can be improved by considering the transient thermal before glassblowing and the non-isothermal cooling step after glassblowing. In both cases, a non-isothermal model must be developed, and more experimental data have to be collected to model the heating up and cooling down processes accurately.

Chapter 4

Post-Processing, Characterization, and Integration

4.1 Introduction

The high-temperature micro-glassblowing processes were developed to fabricate 3D axisymmetric micro-shell structures. In this Chapter, we discuss the release process of glass-blown shell resonators. The initial frequency response characterization of shell resonators are presented. An assembly process was developed for electrostatic actuation of the wineglass modes and capacitive detection of the displacement of the rim. Finally, for the first time, the electrostatic tuning of the resonant modes and the gyro operation of fused quartz glass-blown micro-shell resonator gyroscopes in the open-loop rate mode are presented.

4.2 Substrate Removal

The final step in the fabrication process of 3D micro-shell resonators is substrate removal, as shown in Fig. 2.15d. The substrate was removed in a parallel back-lapping step using an

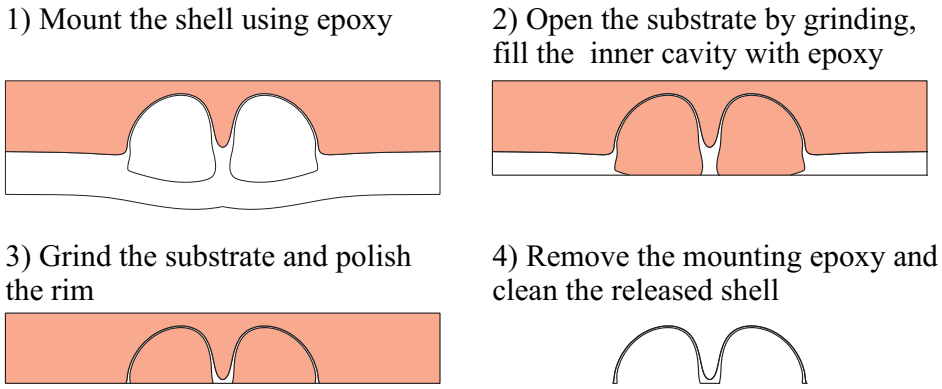

Figure 4.1: Schematics of the substrate removal and polishing process steps. The adhesive epoxy is necessary to support inner and outer surface of thin shells to avoid cracking.

Allied HighTech MultiPrep™ polisher. Figure 4.1 illustrates the lapping and polishing steps schematically. First, the glassblown shell was mounted on a holder using Crystalbond™ 505 temporary adhesive. The adhesive supports the shell and protects it from chipping and cracking. Second, the substrate was lapped until the inner cavity was accessible. The inner cavity was filled with the temporary adhesive to support the thin glass-blown shell from the inside. Third, the bulk of substrate was removed using 30 μm, and 15 μm diamond lapping film and the rim of shell structure was released, and the rim of the shell was further polished using 3.0 μm OpTech™ slurry, followed by 0.5 μm Cerium oxide suspension. Finally, the adhesive was washed-away in a solvent bath, and the shell was cleaned in a Piranha solution after the substrate removal. In some experiments, a thin film chromium layer was deposited on the surface of the shells before mounting them on the adhesive epoxy. In this way, the metal was etched after removing the adhesive to ensure no adhesive residue is left on the shell. An Atomic Force Microscopy (AFM) measurement revealed a surface roughness of 0.21 nm on the polished surfaces, Figure 4.2.

4.3 Initial Characterization

The released shells were attached to a bulk piezo stack for an initial frequency response characterization. An AC signal was applied to the piezo stack, and the amplitude of vibration

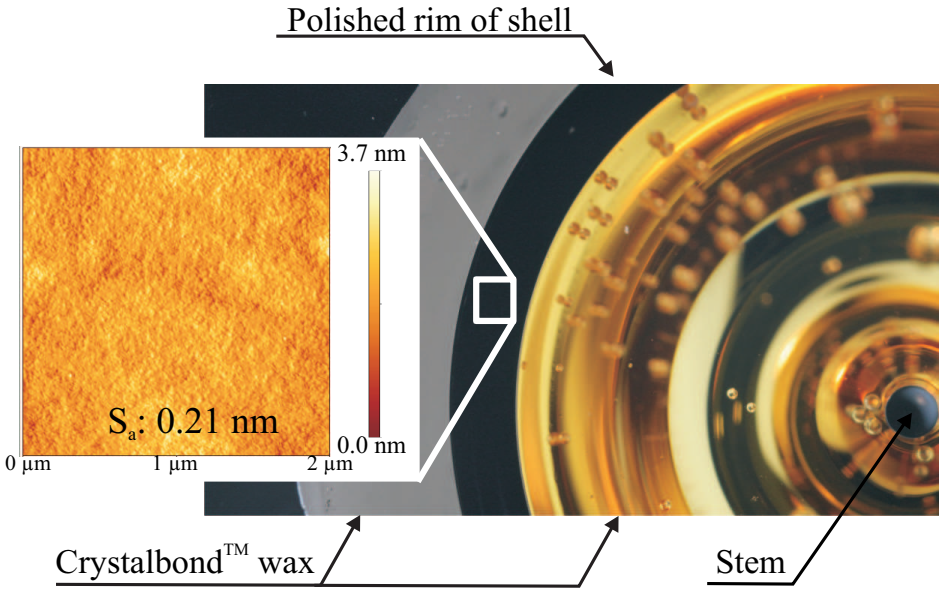

Figure 4.2: The rim of shells was polished after substrate removal. The AFM measurement on a sampling area of 2 μm $\times$ 2μm revealed a surface roughness of 0.21 nm.

was measured using a Laser Doppler Vibrometer (LDV), Figure 4.3. After identification of resonant modes, the ringdown experiment was used to measure the energy decay time and calculate the Q-factor of the fabricated shell resonators in a vacuum chamber. The Q-factor of 0.9 million was measured on the n=2 and 1.33 million on n=3 wineglass mode of an uncoated shell resonator at 20 μTorr, Figure 4.4. The resonant frequency and the Q-factor of the degenerate wineglass modes of the shell are listed in Table. 4.1. The as-fabricated frequency mismatch was 22 Hz and 48 Hz corresponding to the n=2 and n=3 modes, respectively. Damping mismatch ($\Delta Q/Q$) of less than two percent was measured between the degenerate wineglass modes. The comparison between the measured Q-factor and the Q_{TED} of designed resonators revealed that other dissipation mechanisms limited the Q-factor. A non-isothermal and rapid cooling would result in significant thermal stresses which would increase the mechanical energy loss [80]. As viscous fused quartz cools down, the temperature gradient leaves thermally-induced residual stresses [81]. It is technologically challenging to isothermally cool down the glass-blown shells because of different heat transfer modes (conductive cooling from the bottom and convective cooling from top). Also, the pressure difference during the cool down would cause residual mechanical stresses. An optimal ther-

Table 4.1: Comparison between measurement and FE results of wineglass frequencies and Q-factors of a device with 220 μm thickness.

	Axis	Frequency (kHz) (measurement)	Frequency (kHz) (simulation)	Q-factor (measurement)	Q-factor (TED)
n=2	X	22.24	19.49	0.91 M	2.6E8
	Y	22.22		0.9 M	
n=3	X	39.92	40.31	1.3 M	9.6E8
	Y	39.87		1.33 M	

mal annealing was demonstrated to improve the Q-factor by surface dehydroxylation and reduction of internal stresses [80, 82, 83]. The glass-blown shell resonators were thermally annealed in a Thermco 3000 annealing tube furnace with controlled heating and cooling rate. The annealing process was performed as follows:

- Ramping up to 950 ℃ at 3 ℃/min.
- Annealing at 950 ℃ for 9 hours under continuous N_2 flow.
- Cooling down to room temperature at 3 ℃/min.

Fig. 4.5 and 4.6 demonstrate results of the Q-factor improvement after thermal annealing. The Q-factor measurements before and after thermal annealing on four different prototypes are summarized in Table 4.2. Although the annealing process (temperature, duration, and cooling rate) was not optimized for the size of the shell resonator, it provided an evidence that internal thermal stresses were developed in the shell during the glassblowing and cooling. An optimized thermal annealing process parameters such as temperature ramp rate, annealing temperature, dwell time, and cool down rate would significantly improve the Q-factor in glassblown shell resonators. Besides, surface dissipation due to high surface to volume ratio and anchor losses due to unbalanced mass distribution in glassblown shells are other damping mechanisms that contribute to the overall Q-factor of shell resonators.

Lastly, the effect of shell geometric parameters on the modal frequency and order of the

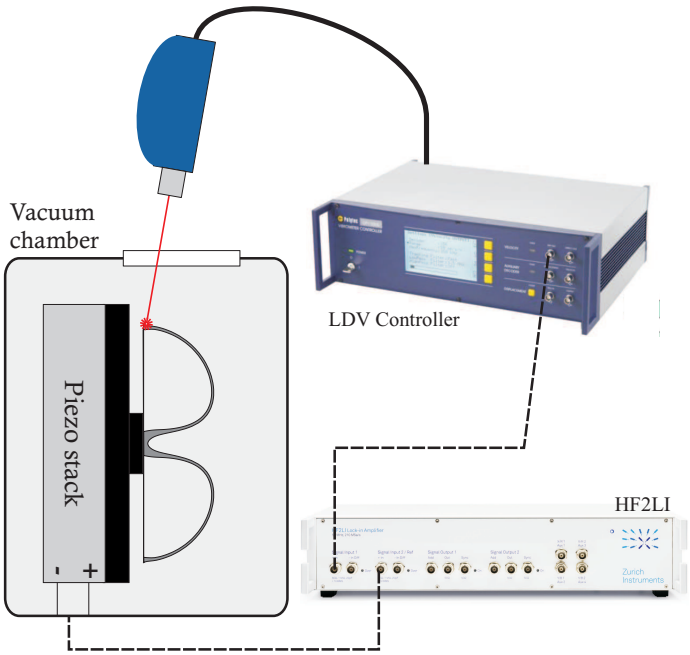

Figure 4.3: Schematics of the Laser Doppler Vibrometer (LDV) setup for an initial characterization of shell resonators. Shells were mounted on a piezo stack using an adhesive for excitation. The velocity at the rim of the resonators were picked up by the LDV and converted to voltage.

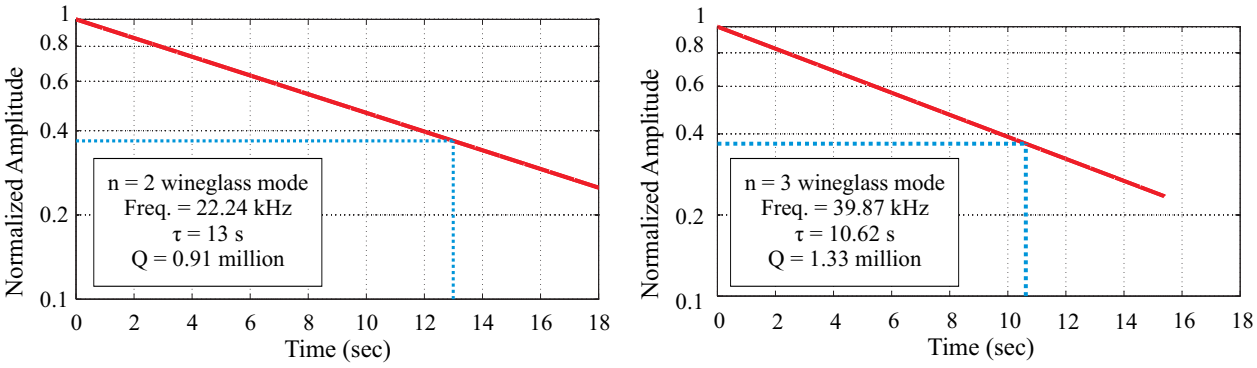

Figure 4.4: Decay time constant of a micro-shell fabricated using the reverse cavity glass-blowing process revealed the Q-factor of over 0.9 million in the n=2 (top) and 1.33 million in the n=3 (bottom) modes, measured at 20 μTorr. The shell diameter was 7 mm with an initial device thickness of 220 μm.

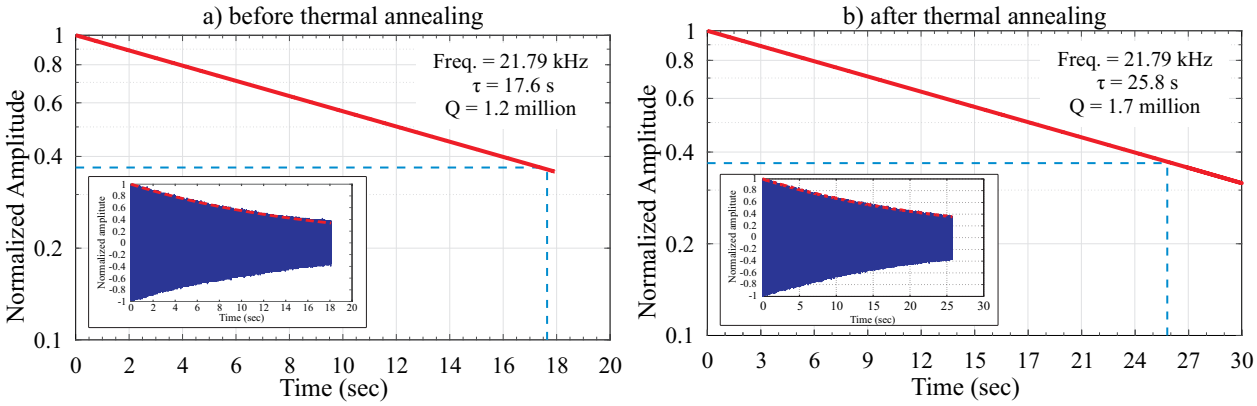

Figure 4.5: Thermal annealing at 950 ℃ for 9 hours improved the Q-factor of a shell resonator (prototype #2 in Table 4.2) from 1.2 million to 1.7 million. No significant change in the resonant frequency was observed.

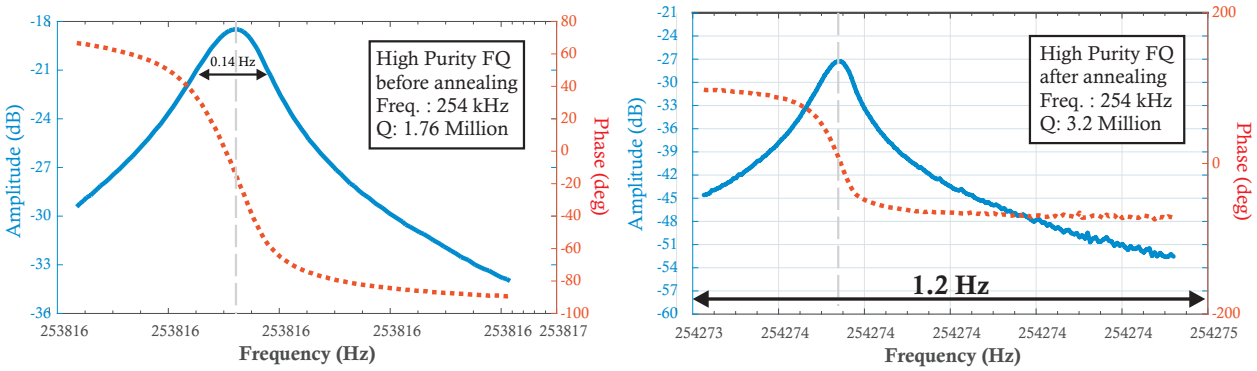

Figure 4.6: Quality factor of the prototype #1 in Table 4.2 was measured from -3dB bandwidth, revealing improvement from 1.76 million to 3.2 million at 254 kHz (n=4) resonant frequency, the highest Q-factor measured so far on micro-glassblown resonators.

Table 4.2: Effect of thermal annealing on the Q-factor of fused quartz glass-blown micro-shell resonators.

	Q-factor (before annealing)	Q-factor (after annealing)
Prototype #1	1.76 M	3.2 M
Prototype #2	1.2 M	1.7 M
Prototype #3	209 K	680 K
Prototype #4	220 K	300 K

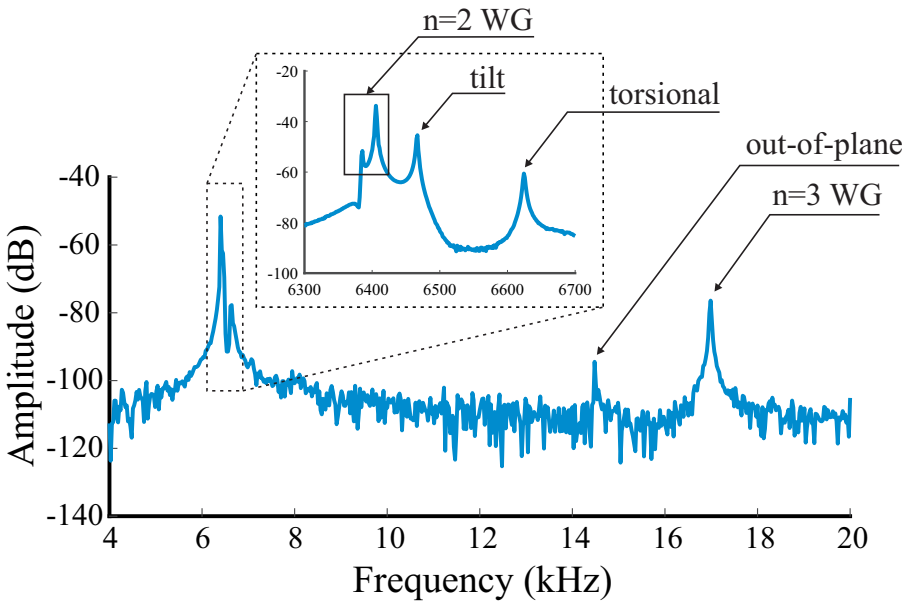

Figure 4.7: An experimental frequency response of a shell resonator with the n=2 wineglass resonance at 6.4 kHz, showing a proximity of spurious resonance mode to the operational mode in a non-optimized design (thickness = 80 μm, shell radius = 5 mm, and anchor radius = 400 μm).

resonance modes were experimentally studied. The mode shape identification was performed using a servo-motor controlled rotary stage to incrementally rotate the shell resonator with respect to the light source. A shell on a piezo stack was mounted on the rotary stage, and the amplitude of vibration was measured using a Laser Doppler Vibrometer (LDV) at incrementally spaced azimuth angles at each peak frequency, to identify the corresponding mode shapes [59]. Figure 4.7 shows the experimental frequency sweep response of a shell resonator, demonstrating the proximity of the resonance modes, less than 200 Hz between the n=2 wineglass mode and the tilt mode in a non-optimized design.

The frequency response of a shell with a thickness of 45 μm, shell radius of 4.25 mm, and anchor radius of 500 μm is shown in Figure 4.8. The n=2 wineglass mode was identified at 5.7 kHz as the first vibrational mode with a minimum frequency separation of 2 kHz to the nearest spurious mode (tilt). The experimental results demonstrated that frequency separation and the mode-ordering could be achieved through parameters of shell geometry,

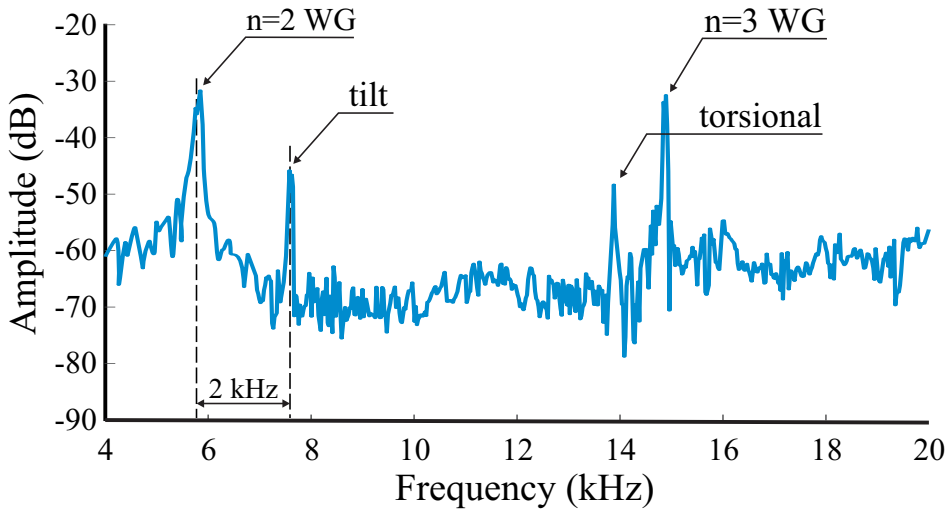

Figure 4.8: A minimum frequency separation of 2 kHz was achieved between the n=2 wineglass and the closest resonance mode (tilt) in one of the design points, with thickness of 45 μm, shell radius of 4.25 mm, and anchor radius of 500 μm. The n=2 wineglass is the lowest resonance mode.

at the operational frequency of interest.

4.4 Controlled Capacitive Gaps

Unlike conventional Silicon MEMS gyroscopes, in which the electrodes are co-fabricated with the sensing elements, and capacitive gaps are defined by the high aspect ratio Deep Reactive Ion Etching (DRIE) process, our current approach for 3D micro-shell device fabrication requires an additional precision assembly step for integration of the shells with an electrode substrate. One of the challenges in the assembly of micro-shell devices is achieving a uniform gap with efficient transduction. On macro-scale, spherical electrodes are machined out of fused quartz and precisely assembled on HRG to make 3D radial capacitive gaps [3]. This process requires a high precision assembly with tight tolerances to avoid electrostatic gap mismatches. An alternative approach is proposed by SAGEM [84], where a planar electrode substrate was utilized to form capacitive gaps between the rim of hemispherical resonators and the electrodes for actuation and detection of the rim of the shell along the axial direction. The planar electrode configuration was adapted for the electrostatic actuation and detection

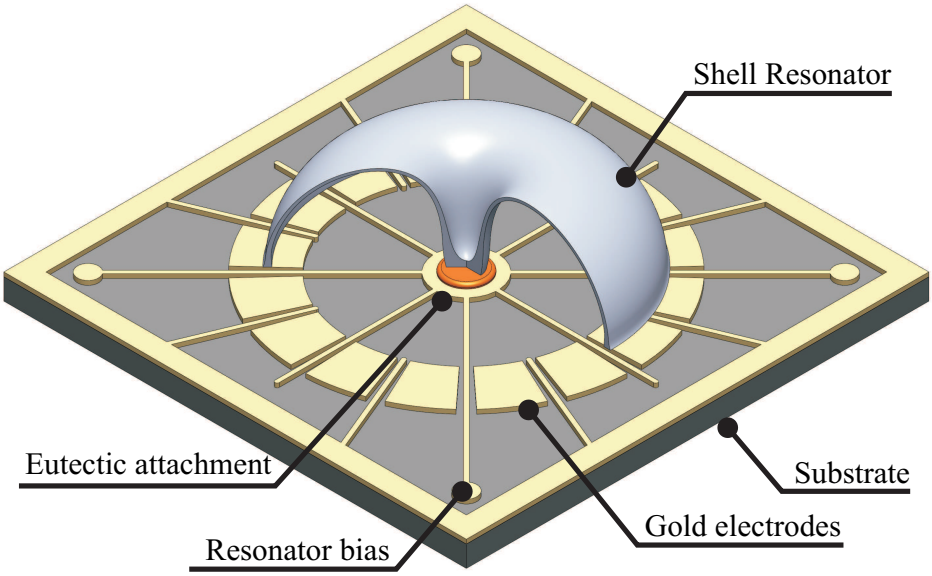

Figure 4.9: Schematics of an integrated shell resonator with planar electrodes [2]

of micro-glassblown wineglass shells [85]. Figure 4.9 illustrates schematics of an assembled shell resonator on a substrate with planar electrodes. Utilization of the planar electrodes make the assembly process less complicated, cost-effective and accommodating to the small off-center error as compared to the peripherally arranged electrodes. However, its main drawback is the limited overlapped area of the shell rim and electrodes when thin shells are used as the sensing element. Thus, the capacitive gaps have to be small to compensate for the limited overlapped area.

In this section, we present the development of assembly processes to reduce the capacitive gaps to smaller than 5μm and to obtain a higher efficiency for the actuation, high-capacitance detection, and a broad range of frequency mismatch tuning.

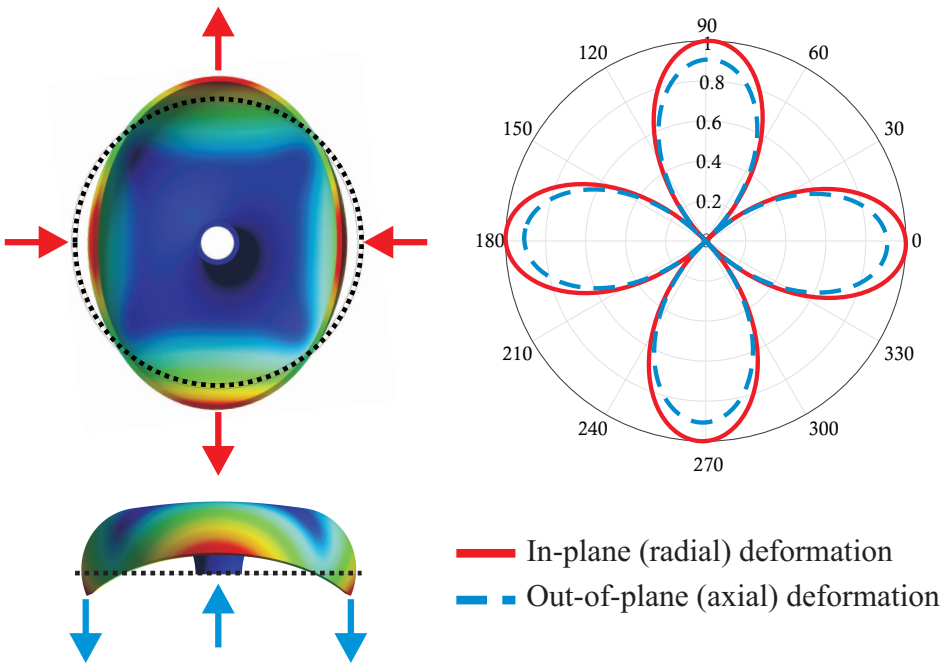

Figure 4.10: In-plane (red) and out-of-plane (blue) components of a wineglass shell resonator. The ratio of out-of-plane to in-plane amplitude is approximately 0.9 on a 7 mm shell with $\sim$110μm thickness

4.5 Electromechanical Modeling of Frequency Tuning

The wineglass mode shape in a 3D shell resonator has three components: in-plane radial, tangential, and an out-of-plane axial displacement. The ratio of the amplitude of axial to radial component depends on the geometry of the shell. Figure 4.10 shows the 3D mode shape of a micro-shell resonator. In hemi-toroidal micro-glassblown shell resonators, with a radius-to-height ratio of around 2, the out-of-plane to in-plane displacement ratio is greater than 3-to-4 [85]. The device under test in this section has 7 mm in diameter and $\sim$100μm in thickness. The normalized radial and axial displacement of the rim vibrating in the n=2 wineglass mode revealed the amplitude ratio close to 1-to-1. Although the axial displacement component is not directly sensitive to the Coriolis force from the z-axis rotation, it can be utilized to actuate the in-plane vibration of 3D shell and detect the Coriolis-induced amplitude along the sense direction.

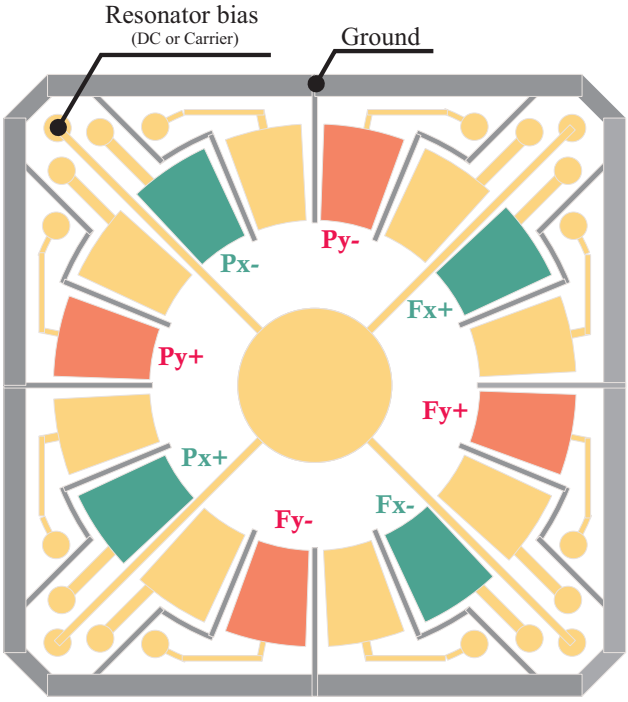

Figure 4.11: The electrode configuration for differential excitation and detection of wineglass modes, green (Fx+. Fx-, Px+, Px-) and red (Fy+. Fy-, Py+, Py-) indicate excitation and detection electrodes for X and Y-mode, respectively. The other electrodes are used for modal decoupling and quadrature cancellation.

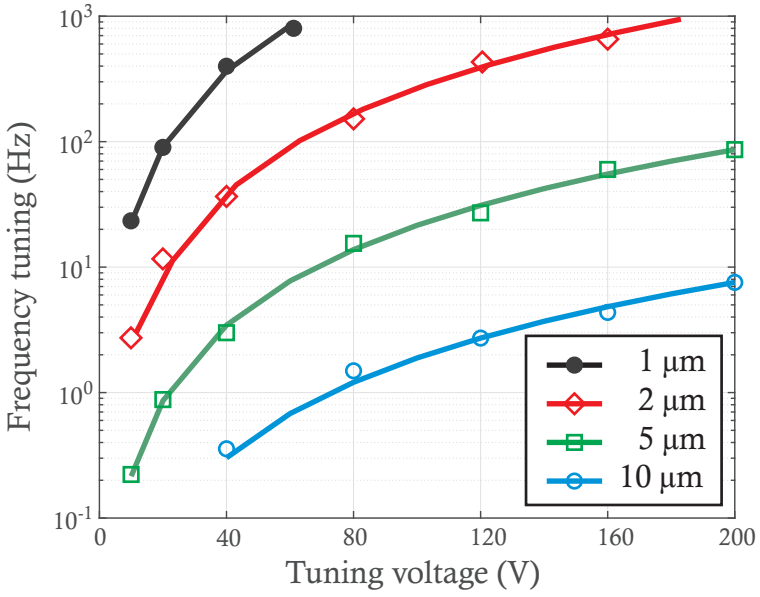

Figure 4.12: Finite element simulation results of the electrostatic frequency tuning of a 17 kHz shell resonator with different capacitive gaps and tuning bias. The results suggests using gap $<5\mu$m for tuning capabilities.

The implementation of planar electrodes forms a parallel-plate type capacitance between the rim of a shell and electrodes. The efficiency of parallel plate capacitive transduction is approximately proportional to the overlapped surface area divided by the square of the gap. The overlapped area is limited by thickness of the micro-shell at the rim. Therefore, the capacitive gaps must be designed for efficient transduction and to compensate for the limited overlapped area. A schematics of the electrodes configuration used in this work is illustrated in Figure 4.11. The 16 discrete electrodes were utilized for the n=2 wineglass mode operation of micro shells. Two orthogonal pairs of electrodes were designated for actuation and detection of each mode. The in-between electrodes were designated for mode decoupling in the presence of mode-to-electrode misalignment. The effect of capacitive gap size on the electrostatic frequency tuning was simulated using a coupled electromechanical model in COMSOL Multiphysics. In the modeling, it was assumed that electrodes are perfectly aligned with the wineglass modes, and DC tuning voltage was applied only to the drive electrodes. The electrostatic frequency tuning results using out-of-plane electrodes at different capacitive gaps on a 17 kHz shell are shows in Figure 4.12. Smaller capacitive gaps would relax the voltage requirements as the negative electrostatic spring is inversely proportional to the capacitive gap cubed. Therefore, reducing the capacitive gap can dramatically increase the frequency tuning efficiency.

4.6 Assembly and Integration

A schematics of the assembly process of micro-glassblown wineglass resonators to form a uniform out-of-plane capacitive gap is illustrated in Figure 4.13. This process includes (1) patterning gold electrodes, traces, and contact pads on a fused quartz wafer, (2) selective deposition/patterning of a sacrificial layer, (3) shell-to-electrode attachment, and (4) removing the sacrificial layer to release the shell and create the capacitive gaps. Three main goals were pursued in the development of the assembly process: (1) vacuum compatibility in material

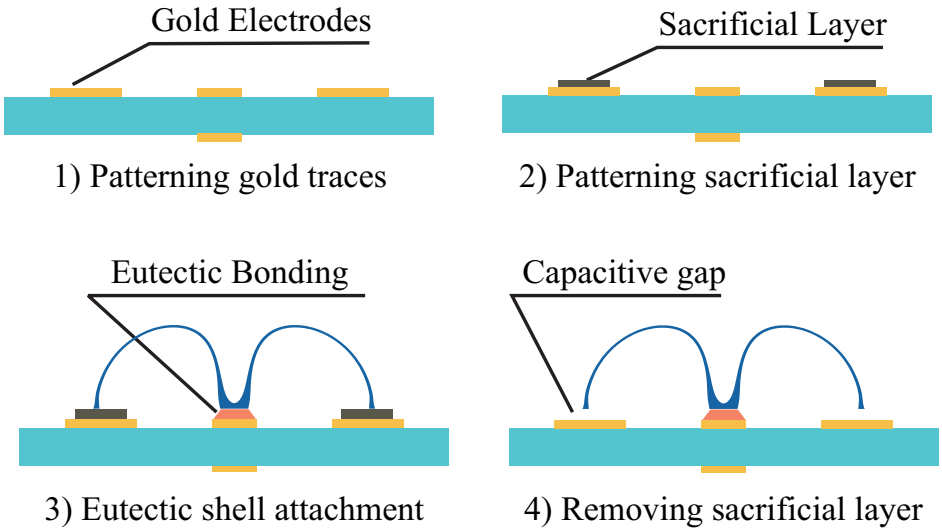

Figure 4.13: The assembly process steps for capacitive gap definition between the planar electrodes and the Fused Quartz shell. A sacrificial layer was deposited and patterned on the substrate wafer, and etched away after shell-to-electrode bonding to create a gap between the rim of the shell and the planar electrodes.

selection for assembly and packaging, (2) compatibility of the materials with the temperature of thermo-compression bonding and vacuum sealing, (3) achieving capacitive gaps smaller than 5μm based on the results of electromechanical simulations.

4.6.1 Electrode Substrate

The planar electrodes and traces were defined on a fused quartz substrate wafer by deposition and patterning of thin-film Cr/Au layers. The planar discrete electrodes for actuation, tuning, and detection, a central contact pad, and metal traces were designed for both electrical biasing and mechanical anchoring the shell. A sacrificial layer up to 5 μm in thickness was selectively formed on the substrate. The thickness of the layer, compatibility of the material with the subsequent shell-to-electrode attachment temperature (for example, $\sim$ 300℃ for AuSn (80-20) eutectic bonding), and scalability to the wafer-level fabrication were considered for this step. Table 4.3 summarizes the trade-offs of the material selection. A thin-film Nickel layer was electroplated, and thin-film amorphous silicon (a-Si) was deposited using the plasma-enhanced chemical vapor deposition (PECVD) and patterned on RIE, on the

Table 4.3: Material selection for sacrificial layer

Sacrificial material	Application method	Removal method	Results
Shim	Manual	Manual	- Die-level - Limited to 10 um (thickness of shim) - Compatible with AuSn process
Photoresisit	Spin-coating	Solvent	- Uniform and wafer-level - Not compatible with AuSn process
Thin film (metal)	Electroplating	Wet etching	- Uniform and wafer-level - Compatible with AuSn process - <5um capacitive gaps
Thin film (a-Si)	PECVD	Isotropic dry etching (RIE/XeF2)	- Uniform and wafer-level - Compatible with AuSn process - <5um capacitive gaps

Table 4.4: Material selection compatibility and the process requirements for shell to electrode attachment process

Bonding type	Temperature compatibility	Outgassing	Electrical conductivity	Mechanical strength
Glass Frit	Yes	Yes	No	Yes
Indium alloy	No	No	Yes	No
Conductive epoxy	Yes	No	Yes	Maybe
Eutectic	Yes	Yes	Yes	Yes

substrate before the shell attachment as the sacrificial layer, Fig. 4.14.

4.6.2 Bonding of Micro-Shell Resonators to Substrate of Electrodes

Shell resonators were attached to the substrate of electrodes through their central stem. The central stem acts as a mechanical anchor point as well as an electrical connection for biasing the shell; thus, imposing the electrical conductivity requirement for the shell attachment. Also, the material has to be low out-gassing, compatible with the temperature of the subsequent vacuum sealing process (maximum temperature of 320℃), and provide high bond strength. Table 4.4 summarizes the process requirements and different types of attachments which were explored in this work.

The low melting temperature of Indium alloy, out-gassing of die attachment epoxies (JM7000 and 84-1LMI) after vacuum sealing, and dielectric properties of glass frit do not meet the

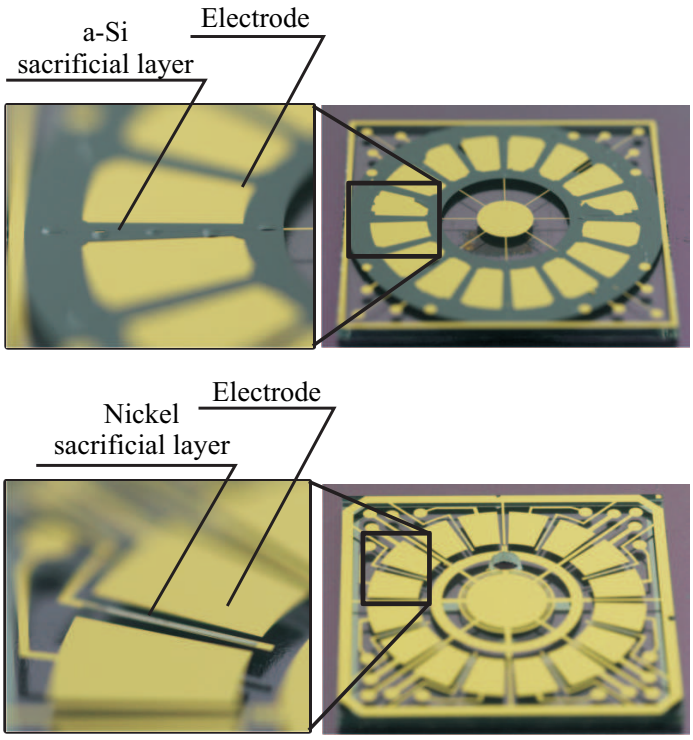

Figure 4.14: An assembled and packaged micro shell resonator gyroscope and SEM image of the capacitive gap. The inset figure shows 4.5 μm gap size measurement.

process requirements. An alternative bonding method to attach shell resonators to the electrode substrate is Gold-Tin (80/20) alloy eutectic bonding. For the eutectic bonding, the inner surface of the fused quartz shell resonators must be coated with a thin-film gold layer. The stack of electrode substrate/AuSn preform/wineglass resonator was heated up to above the eutectic point inside a vacuum reflow chamber. This technique provides a low out-gassing and strong bonding between the shell and the electrode substrate.

4.6.3 Controlled Capacitive Gaps

After the attachment step, the sacrificial layer was etched away to form the capacitive gaps. A compatible Nickel etchant TFG was used to selectively remove the Ni sacrificial layer without damaging Cr/Au electrodes and fused quartz. Figure 4.15 shows an assembled and packaged fused quartz device and an SEM image of the capacitive gap between the rim of the shell and the planar electrodes, demonstrating uniform $<5\mu$m capacitive gaps. The

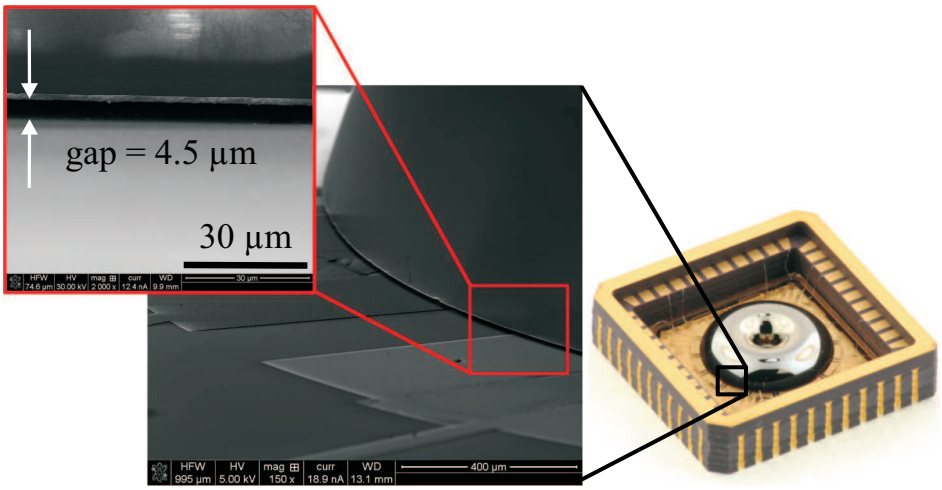

Figure 4.15: An assembled and packaged micro shell resonator gyroscope and SEM image of the capacitive gap. The inset figure shows 4.5 μm gap size measurement.

Table 4.5: Capacitance measurement of the assembled devices

Device No.	Sacrificial layer	Capacitive gap [μm]	Rim thickness [μm]	Total capacitance [pF]
1	Thin film Ni	~5	110	9.6
2	Thin film Ni	~5	175	14
3	Thin film Ni	~5	150	11
4	10 μm shim	~12	150	5.6
5	10 μm shim	~12	150	5.7
6	25 μm shim	~25	500	7.9
7	25 μm shim	~25	500	7.9

measured total rest capacitance of the assembled devices are presented in Table 4.5. The total capacitance of a device assembled using Ni thin film sacrificial layer was as high as ~14 pF, which experimentally confirms a reduction in the gap size.

4.7 Electrostatic Gyro Operation

4.7.1 Electrostatic Frequency Tuning

The planar electrodes and the rim of a shell create parallel-plate type actuation and detection electrodes. The electrostatic spring softening acting on the axial component of the shell oscillation acts indirectly upon the in-plane frequency tuning. Figure 4.16 illustrates the

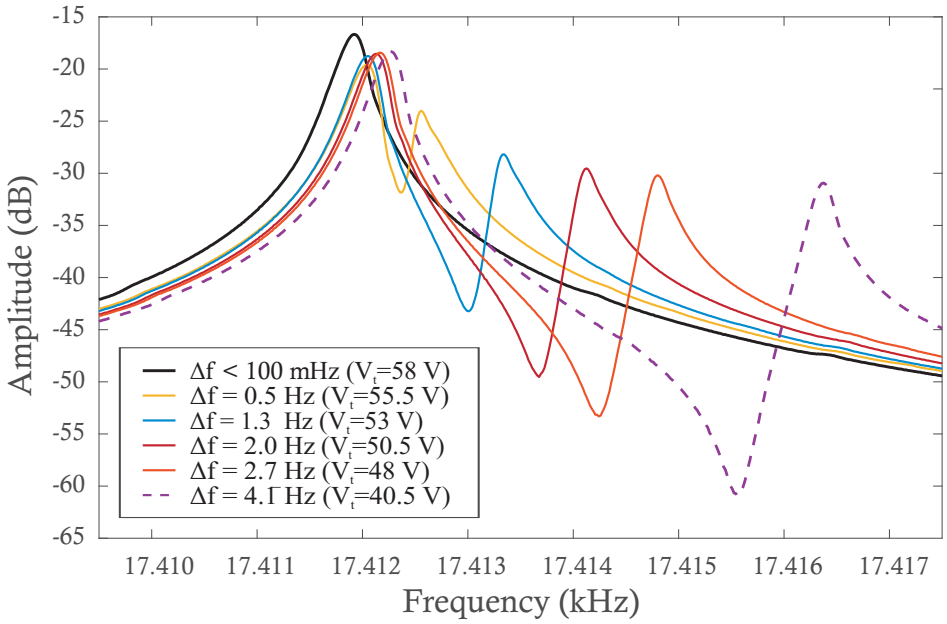

Figure 4.16: Experimental results on electrostatic tuning of the n=2 in-plane wineglass modes using out-of-plane electrodes with 4.5 μm capacitive gaps, 58 V tuning voltage (diagonal + off-diagonal) was required for tuning the as-fabricated frequency split of 7 Hz to <100 mHz at 17.4 kHz center frequency (device no. 1 in Table 4.5).

frequency sweep response of the assembled fused quartz shell with different tuning voltages (V_t). The mismatch between the modes was electrostatically tuned from 7 Hz (as-fabricated) to $<$ 0.5 Hz by applying DC tuning up to 58 V to the diagonal and off-diagonal tuning electrodes.

4.7.2 Open-Loop Rate Response

An open-loop rate response of the assembled fused quartz micro-wineglass gyroscope was characterized by applying a sinusoidal input rotation at different input rates on a rate-table. Figure 4.17 shows the output of the device with respect to input angular rotations. A scale factor of 0.49 mV/(deg/sec) was extracted using Phase-Locked Loop (PLL), and Amplitude Gain Control (AGC) loops on the drive mode without any frequency tuning and quadrature compensation. Figure 4.18 shows the Allan deviation plot of the zero-rate-output (ZRO) of the assembled device for noise performance characterization with a bias

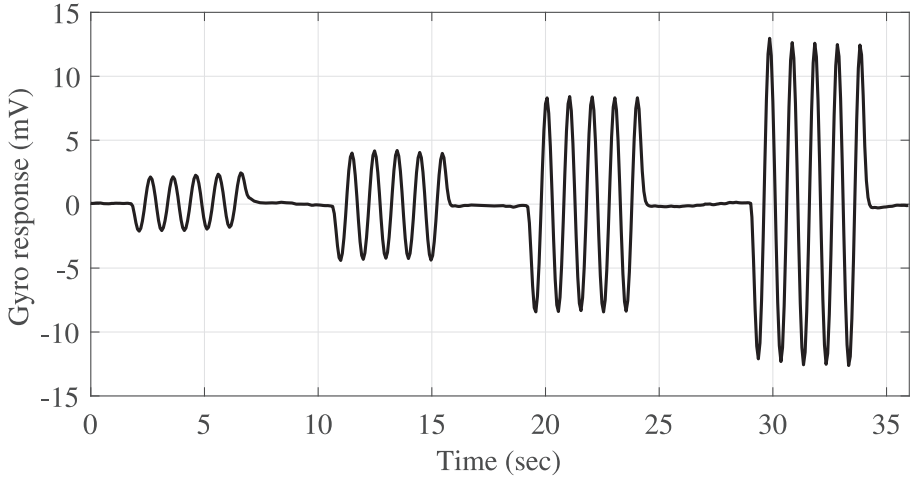

Figure 4.17: Open-loop rate response of a micro-glassblown fused quartz gyroscope (device no. 1 in Table 4.5) under ± 5, 10, 20, and 30 (deg/sec) sinusoidal input rate, revealing an open-loop scale factor of 0.49 mV/(deg/sec).

instability of 22 [deg/hr] and Angle Random Walk (ARW) of 1.84 [deg/rt.hr]. This was the first demonstration of gyro operation on an assembled fused quartz micro-shell resonator with the out-of-plane electrode architecture.

4.8 Conclusion

In this chapter, for the first time, the operation of a glass-blown micro-shell resonator gyroscope in the open-loop rate mode was demonstrated. The post-fabrication assembly process to build a complete operational device was discussed in details. The surface quality of the polished rims and the residual thermal stresses were identified as the energy dissipation mechanisms. An optimized polishing process to achieve sub-nm surface roughness, and a post-release thermal annealing process was shown to improve the Q-factor. The highest measured Q-factor on the n=2 mode was 1.2 million and 1.7 million before and after thermal annealing in an un-coated shell at 21.8 kHz [86]. The highest Q-factor measured in higher-order wineglass mode (n=4) was 1.76 million and 3.2 million before and after annealing at the center frequency of 254 kHz. Also, the effect of shell geometry on the ordering

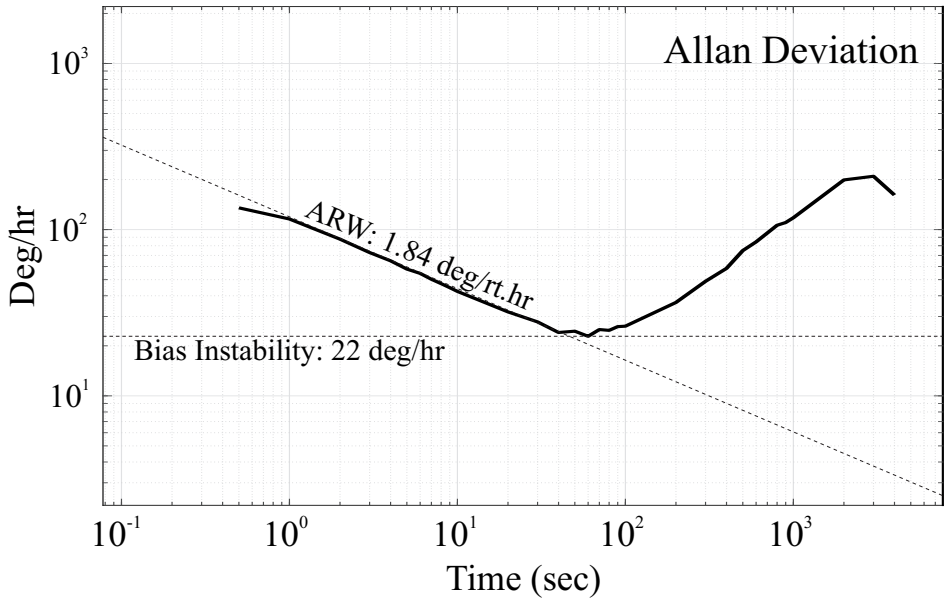

Figure 4.18: Allan deviation plot of the zero-rate output of the assembled shell resonator gyroscope revealed bias instability of 22 [deg/hr] and Angle Random Walk (ARW) of 1.84 [deg/rt.hr].

of resonant modes was demonstrated. A micro-shell resonator was fabricated with the n=2 wineglass resonant frequency of 5.7 kHz, as the first resonant mode, with 2 kHz frequency separation with the closest neighboring mode.

The full-cycle development of a vacuum-compatible assembly process to achieve a uniform $<5\mu$m capacitive gap was presented. The precision micro-assembly is a crucial technological step toward improving the performance of micro-shell resonators. A numerical simulation was performed to estimate the gap and voltage requirements for the electrostatic tuning of frequency mismatch between the orthogonal n=2 wineglass modes. The planar electrode configuration was employed to integrate shell resonators with an electrode substrate for capacitive actuation and detection of wineglass modes. The developed assembly process achieved a uniform capacitive gap with effective transduction for actuation, detection, and electrostatic frequency tuning. A capacitive gap $<5\mu$m (1:20 aspect rate) was demonstrated on 7 mm fused quartz shell resonators, forming the total active capacitance of up to 14 pF for electrostatic operation. For the first time, the gyro rate response of a vacuum-sealed

fused quartz gyroscope operating in the open-loop mode was demonstrated experimentally. The proposed assembly process showed an accurate control over the definition of capacitive gaps, which is critical for tuning and controlling the vibration shape for the rate and rate-integrating modes of operation. The high-vacuum and high-temperature (up to 300 ℃) compatibility of the materials and the processes allow for vacuum sealing of the assembled devices with getter activation, which is an essential step toward operation of high-performance 3D micro-shell resonator gyroscopes.

Chapter 5

Dual-Shell Resonator Gyroscope

5.1 Introduction

The implementation of MEMS gyroscopes in high-performance guidance, navigation, and space exploration applications requires sensitivity to low rates of rotation while maintaining the sensor integrity and providing a high degree of reliability in adverse environmental conditions, such as high-spin rotations, high-g shock, and intense vibrations. The stresses induced by such a harsh dynamic environment would result in the initiation of microcracks at the high stress-concentration locations and fracture of the sensor's structural material. The displacement induced by the external shocks and vibrations during the operation of an electrostatically driven MEMS gyroscope could reduce the threshold of the dynamic pull-in stability and result in snap-down of the resonant structure and electrical shorts.

The design of suspension elements and implementation of over-drive stoppers can improve the in-plane shock resilience of MEMS devices [87]. Integration of MEMS sensors with passive and active vibration isolation stages would be another solution to improve reliability of MEMS sensors under repetitive shock and vibration cycles [88, 89, 90]. Such approaches

may protect sensors during shock or vibrations, but cannot be employed for measurements of rotations during shock events. High-frequency gyroscopes are an alternative implementation when high-g shock tolerance is required. In such design approaches, the operation frequency of devices is selected well above the expected shock spectra for enhanced immunity to environmental shock and vibrations [91]. Among "flat" MEMS devices, Surface Acoustic Wave (SAW) and Bulk Acoustic Wave (BAW) based gyroscopes take advantage of operations at high frequency in addition to a lack of released moving parts. Such devices provide a compromise between increased immunity to shock and vibration, but reduced electrostatic tunability and reduced scale factor.

"Non-flat" Coriolis Vibratory Gyroscope (CVG), like Hemispherical Resonator Gyroscope (HRG), provides a rugged structure with higher out-of-plane stiffness as compared to their "flat" counterparts [3]. The in-plane and out-of-plane stiffness in HRG-type devices depend on the 3D geometry of its core sensing element. In addition, fused quartz as the structural material provides minimum possible losses due to internal friction and absence of precedence directions due to its isotropic mechanical properties. In recent years, the fabrication processes based on bulk deformation of fused quartz at high temperature were developed to realize miniaturized, isotropic, and high mechanical Q-factor 3D shell resonators [1, 92]. These 3D shells were rigidly bonded to a substrate for capacitive actuation and detection using planar electrodes [2] or peripherally distributed electrodes [93]. In both cases, the shells were anchored to the substrate solely through the inner stem. Although the shell geometry provides a rugged structure for harsh environments, the limited bonding area at the stem of micro-shells becomes the weakest point in the assembled sensors.

This Chapter introduces a fused quartz dual-shell microstructure, discussing its design, modeling, fabrication, and instrumentation as a resonator and a gyroscope. The dual-shell resonator, shown in Fig. 5.1, provides a fixed-fixed anchor for resonating shell, stiffening the spurious vibrational (tilt and out-of-plane) modes, as well as providing a larger bonding area

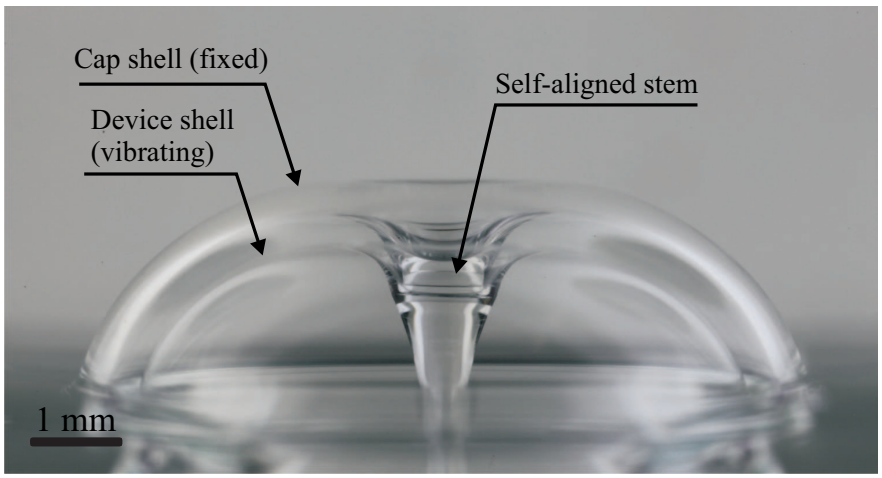

Figure 5.1: A fused quartz dual-shell prototype. The two-layer shell structure was co-fabricated using micro-glassblowing process, providing a sensing element (device shell), a self-aligned fixed-fixed anchor for increased immunity to mechanical shocks and vibrations, and a housing (cap shell) for vacuum encapsulation.

for the shell to substrate integration. A fabrication process was developed, and a Finite Element Model (FEM) framework was presented to study the effect of process parameters on the final dual-shell geometry. Resonator prototypes were demonstrated, validating the proposed approach for fabrication of the dual-shell structure for MEMS resonators. An electrode substrate using silicon-in-glass reflow was fabricated for subsequent integration of the dual-shell resonators. An electrostatic actuation, capacitive detection, frequency mismatch tuning, and open-loop gyro operation of a dual-shell resonator gyroscope were demonstrated experimentally.

5.2 Dual-Shell Resonator Architecture

A dual-shell resonator gyroscope consists of a two-layer micro glassblown shell structure, assembled on a substrate with planar electrodes for (i) capacitive actuation and detection of normal wineglass modes and (ii) vacuum encapsulation of the sensing element, Fig. 5.2. The dual-shell glassblown structure is comprised of an outer (cap) and an inner (device) shell, co-fabricated simultaneously in the micro-glassblowing process [94]. After removing

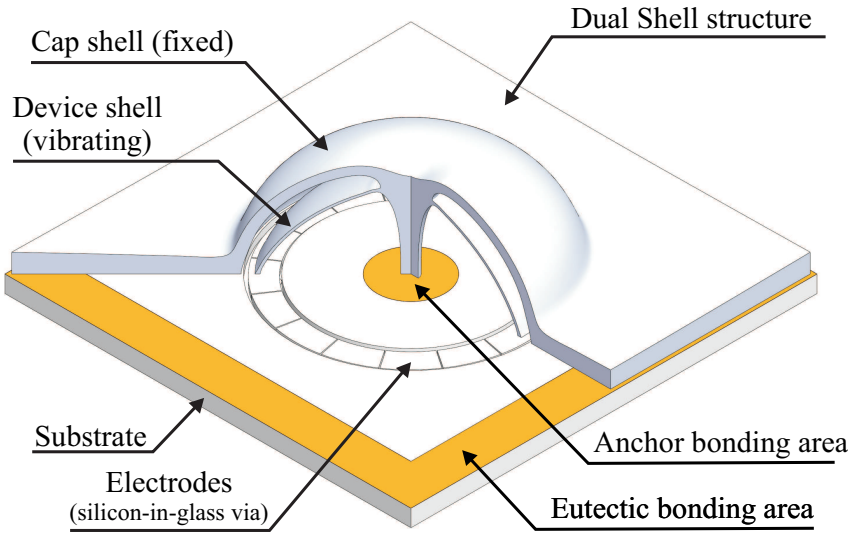

Figure 5.2: Schematics of a 3D dual-shell resonator device, co-fabricated in a single glass-blowing step and assembled on a substrate with planar electrodes. The bonding of cap shell and stem to the substrate forms a fixed-fixed anchor for the vibrating shell. A defect-free eutectic bonding would enable in-situ vacuum encapsulation for the device shell.

the substrate, the device shell is free to vibrate while the inner stem and the outer shell are bonded to a substrate, providing a fixed-fixed anchor for the vibrating shell. The glassblowing forms the dual-shell structures concurrently in a single step, eliminating the post-fabrication alignment and bonding of the cap shell to the device shell.

The principle of operation of the gyroscope is based on inertial properties of elastic waves in solids. When the vibrating inner shell is subjected to an inertial rotation, the vibration pattern would rotate with respect to the gyro case frame [95]. Fig. 5.3 illustrates eight (out of many) resonant modes of a typical dual-shell structure. For the gyro operation, the inner shell would operate in its degenerate wineglass modes (preferably n=2), using an electrostatic excitation and detection scheme. The outer shell and the inner stem are anchored to a substrate, providing a double-end fixed anchor to enhance the structural rigidity and high-g shock resilience, and is anticipated to enable a continuous gyro operation through external shock and vibrations. Moreover, spurious modes, such as tilt, rotation, and

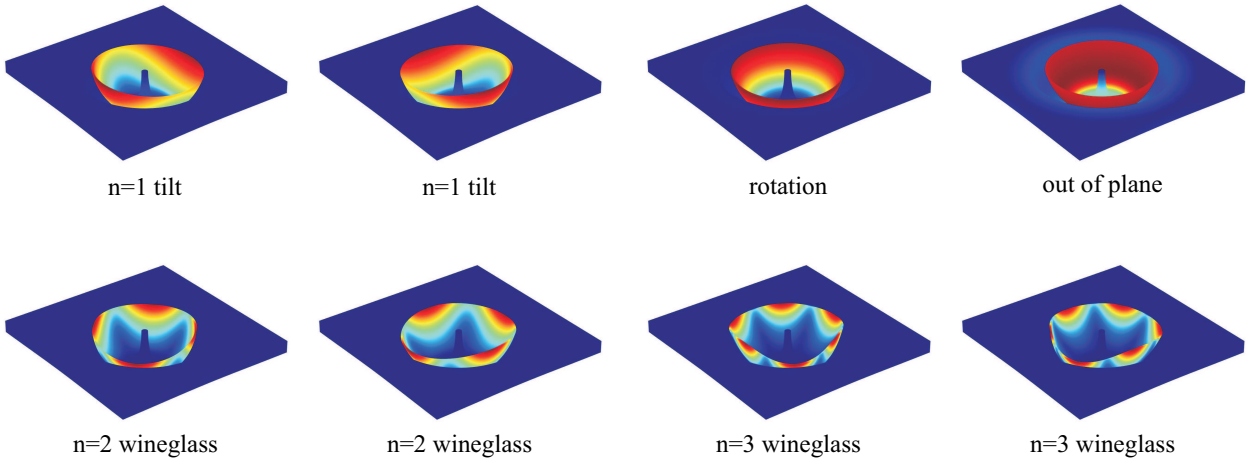

Figure 5.3: Eight vibrational modes of a generic dual-shell resonators. All degenerate wineglass modes can be used for rotation sensing, however the n=2 mode is preferable due to a higher gain in the rate and whole angle modes of operation.

out-of-plane, can be selectively stiffened through geometric design of the inner shell, outer shell, and the inner stem to reduce the environmental sensitivity and energy loss through mode mixing [96].

The substrate of a dual-shell device consists of silicon planar electrodes, fabricated using glass-in-silicon re-flow process, and the bonding area for subsequent hermetic bonding of the inner anchor and the cap shell. The cap shell provides a protective shield for the inner shell, enabling an in-situ vacuum sealing capability when a defect-free bonding is formed in the designated bonding areas. In the current assembly method, a eutectic bonding using Gold-Tin (80-20) alloy is performed. The inner surface of the vibrating shell and the cap shell were selectively coated with Chromium and Gold. The planar extension of the cap shell was designed to accommodate the required area for eutectic bonding. Since eutectic bonding provides electrical conductivity, the inner shell was biased through the anchor using central silicon via. The capacitive gaps for excitation and detection were defined using the silicon DRIE process. The integration process is presented in details in Section 5.6.

5.3 Fabrication of Dual-Shell Resonator

Fabrication of the dual-shell structures was developed based on wafer bonding and high-temperature glassblowing processes for hemi-toroidal shell resonators [97]. The main fabrication steps are demonstrated schematically in Fig. 5.4. High-purity fused quartz wafers (Corning HPFS® 7980) with an initial thickness of 500 μm were used in fabrication of the dual-shell resonators. A 2 μm undoped polysilicon was deposited on the wafers using Low Pressure Chemical Vapor Deposition (LPCVD) as a hard mask for subsequent wet-etching process. After patterning the hard mask in a Reactive Ion Etching (RIE) chamber, the cavities were pre-etched in the isotropic wet etching process using hydrofluoric (HF) acid (48 wt. % in water solution). The cavities were time-etched and the etch rate was monitored to achieve the desired depth of etch, typically 400μm and 100μm on the device and the cap wafer, respectively. The polysilicon hard mask was removed afterwards and wafers were chemically cleaned in a RCA-1 bath prior to the wafer bonding. First, a blank fused quartz substrate wafer was bonded to the device wafer using plasma-assisted direct bonding. Next, the cap wafer was aligned and bonded to the substrate/device wafer pair in an AML-AWB wafer bonder. The substrate/device/cap triple-stacked wafer was annealed after bonding to complete the bond formation. An array of aligned cavities were formed after the three-wafer stack was completed. Fig. 5.5 shows the cross-section of a triple-stack fused quartz die before the glassblowing.

The glassblowing process was performed in a Rapid Thermal Processing (RTP) furnace at 1550 $^{\circ}C$. The glassblowing temperature was chosen above the softening point of the fused quartz when the viscosity drops and fused quartz becomes a viscous fluid. At the same time, the pressure builds up inside the cavities. The combined effect of pressure build-up and viscosity reduction expands the encapsulated cavities and forms a 3D dual-shell structure with a self-centered stem. During the viscous deformation of fused quartz, the surface tension

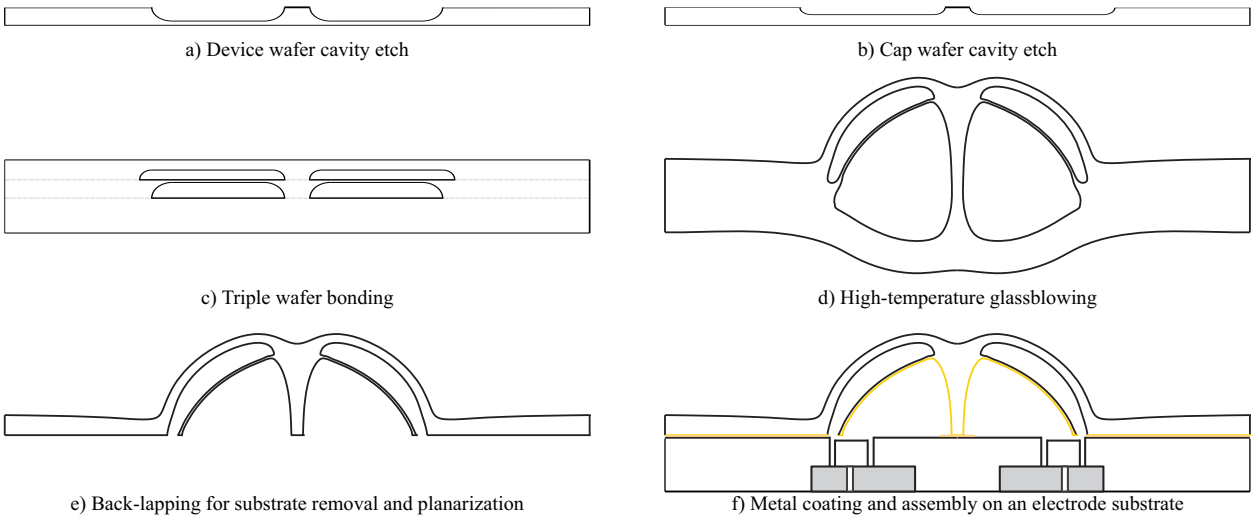

Figure 5.4: Fused quartz dual-shell fabrication process flow: a) cavity pre-etching on the device wafer, b) cavity pre-etching on the cap wafer, c) substrate/device/cap triple stack plasma-assisted wafer bonding and annealing, d) glassblowing in a high-temperature furnace at $>1500\ ^{\circ}C$, e) substrate removal and planarization by lapping, f) assembly on a substrate with through wafer vias.

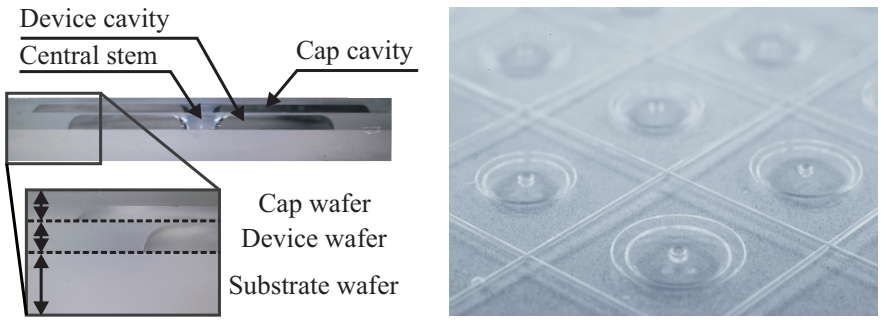

Figure 5.5: (Left) cross-section of a double-cavity triple stacked wafers, (right) a bonded wafer stack showing concentric cavities before the glassblowing.

would minimize the surface area and form an axi-symmetric hemi-toroidal or hemispherical geometry. Using this process, both layers of fused quartz shells (inner and outer) were co-fabricated from concentric cavities, Fig. 5.4d. Fundamentally, the glassblowing process can be performed on the wafer-scale using a high-temperature furnace with a uniform temperature distribution across wafer. In the current fabrication experiments, the wafers were dices after the bonding step, and the glassblowing was performed on the die-level to operate within uniform temperature zone of the furnace. The glassblowing process time was between two to three minutes to fully develop a shell structure.

Fig. 5.6 illustrates a dual-shell prototype after the glassblowing. The inner shell was released by removing the substrate in a parallel back-lapping step using an Allied HighTech MultiPrep™ polisher. The bulk of substrate was removed using 30 μm and 15 μm diamond lapping film. The rim of the inner shell was polished using 3.0 μm OpTech™ slurry and 0.5 μm Cerium oxide suspension. After polishing, shell resonators were chemically cleaned in Piranha solution for 30 minutes, followed by 1 minute dip in a buffered oxide etch (BOE) solution comprised of a 6:1 volume ratio of 40% NH4F in water to 49% HF in water. An Atomic Force Microscopy (AFM) measurement revealed surface roughness of 0.3 nm on the polished surfaces. After polishing, the outer shell rim, inner shell rim, and the inner stem create a reference plane for subsequent integration of the dual-shell resonator with a substrate for planar electrodes for an electrostatic actuation and detection. The mechanism of electrostatic excitation and the integration process are discussed in details in Section 5.6.

Fig. 5.7 shows an optical image of the cross-section of a dual-shell prototype. The inner and outer shell have different thicknesses and share a common stem.

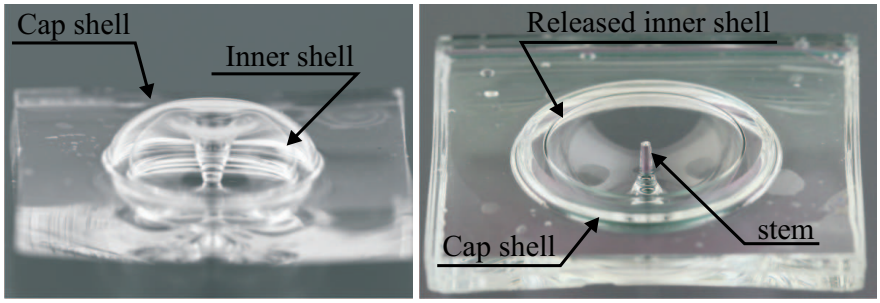

Figure 5.6: (Left) A glassblown dual-shell prototype, fabricated using triple-stack wafer bonding and high temperature glassblowing, (right) a released dual-shell die after substrate removal and planarization using back-lapping.

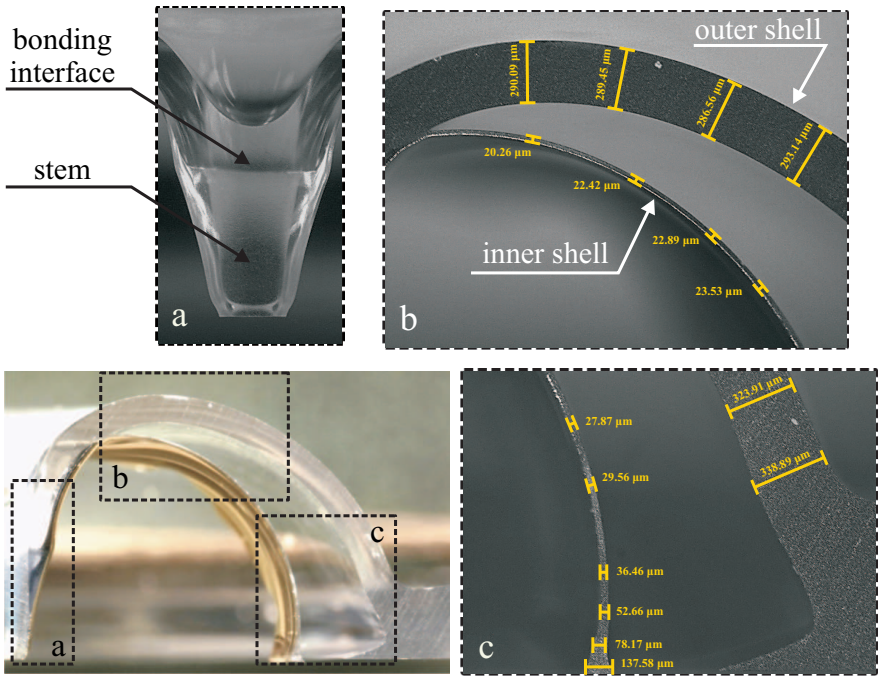

Figure 5.7: An optical cross-section image of a dual-shell structure with initial device thickness of 70 μm and cap thickness of 420 μm, (a) the central stem, (b) the different device and cap shell thickness at the top, (c) the device and cap thickness at the rim.

Table 5.1: Design and process parameters of the dual-shell resonators

Device shell parameters	Cap shell parameters	Process parameters
- Device cavity radius (D_1)	- Cap cavity radius (C_1)	- Glassblowing pressure (P_{gb})
- Device anchor radius (D_2)	- Cap anchor radius (C_2)	- Glassblowing temperature (T_{gb})
- Device cavity etch (D_h)	- Cap cavity etch (C_h)	- Device wafer-bonding pressure (P_{dw})
		- Cap wafer-bonding pressure (P_{cw})

5.4 Finite Element Simulations

The hybrid fluidic-structural multiphysics finite element modeling approach, as described in Chapter 3, was employed to (i) predict the final geometry of the dual-shell structures from initial parameters, (ii) perform a modal analysis to determine the resonant frequency of operational and spurious modes, and (iii) predict the response of different dual-shell designs under transient dynamic loads.

5.4.1 Prediction of Dual-Shell Geometry

The final geometry of the glassblown shells depends on the geometric and process parameters, listed in Table 5.1. The geometric design parameters are the device and cap anchor radius, the device and cap cavity radius, thickness of the substrate, device, and cap wafers, and the etch depth of the device and the cap wafer. The process parameters are wafer bonding pressure of device-to-substrate and cap-to-device bonding, temperature, and pressure of glassblowing [97]. Thus, predicting the final geometry is an essential tool for design of the dual-shell resonators.

A 2D axisymmetric model with triangular elements was built for time-dependent dual-shell glassblowing simulations, combined with a Lagrangian representation, as shown in Fig. 5.8.

In all of the simulations, the thickness of the substrate, device, and cap wafer were 1 mm, 500 μm, and 500 μm, respectively. The dual-shell glassblowing process was simulated for two cases. In the first case, the etch depth of cap wafer was changed in a parametric FE

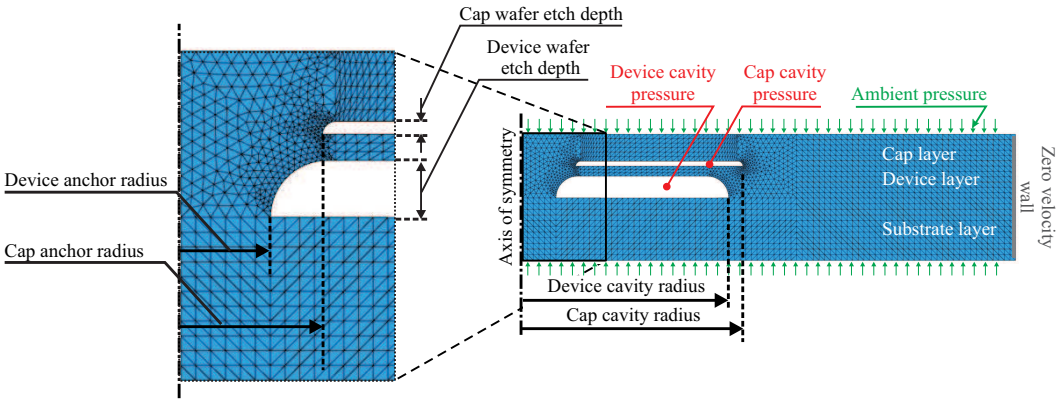

Figure 5.8: Finite element model of the dual-shell glassblowing process. All three layers (cap, device, substrate) were modeled as viscous fluid domains. The geometric design parameters of the device and the cap wafers, listed in Table 5.1, are indicated in the figure.

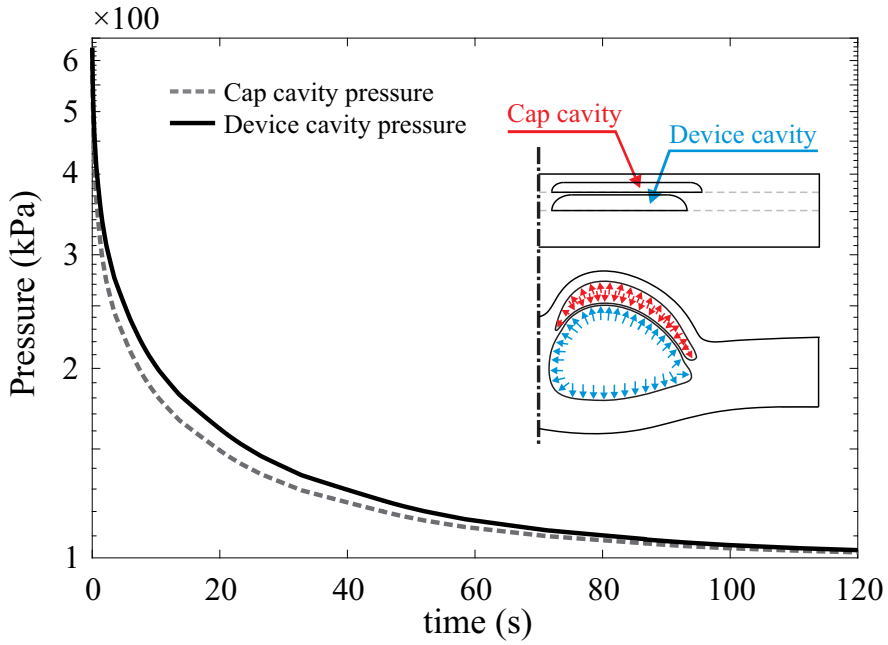

Figure 5.9: Illustration of pressure change in the cap and device cavity in a generic glass-blowing simulation, the pressure drops as cavity volume increases and reaches an equilibrium with the ambient pressure.

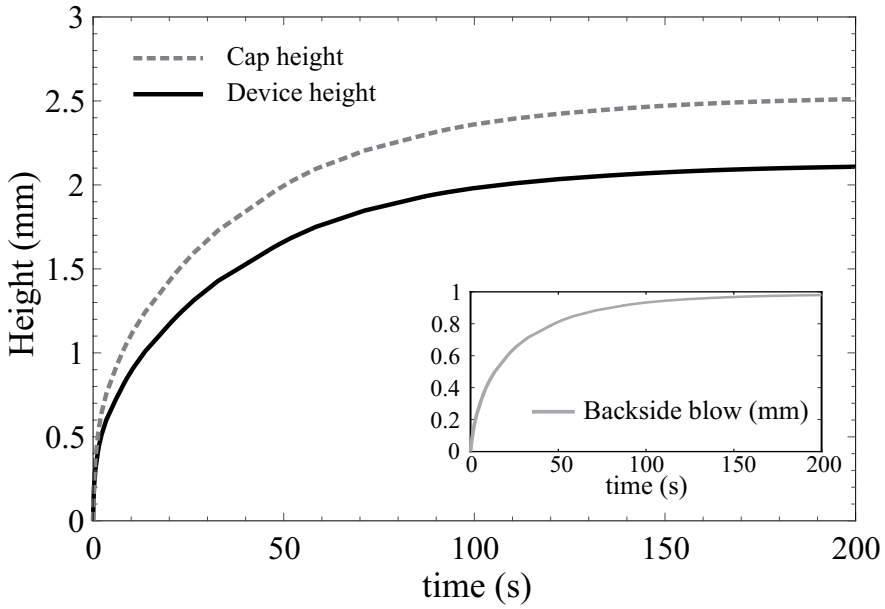

Figure 5.10: Evolution of cap and device shell height in a generic glassblowing simulation, demonstrating the self-limiting nature of the process. As cavity volume increases, the deformation rate reduces. The inset figure shows the deformation due to blowing on the substrate side of the triple stack.

simulation from 100 μm to 400 μm, and the etch depth of device wafer was 400 μm. Thus, the thickness ratio of the cap layer to the device layer was varied from 4 to 1. Fig. 5.11 shows the predicted final geometry for four different thickness ratios. The thinner the cap shell the larger the initial volume of the cap cavity would be, and, subsequently, the cap shell would blow higher. In the second case, the volume of the cap and device cavities were constant. The initial pressure of the cap cavity was varied to provide different cap-to-device pressure ratios, resembling the wafer bonding of the cap layer at different reduced pressures. The cap wafer bonding at a lower pressure would reduce the blowing height of the cap shell, Fig. 5.12. The simulation results revealed that a variety of the dual-shell geometries could be realized by controlling the pressure ratio and thickness ratio of the device and cap wafers.

The simulation's predictions were compared with measurements of a fabricated dual-shell prototype. A comparison between measurements and predictions are summarized in Table 5.2. It was observed that the developed finite element model predictions are closely matched (less than 10% error) with the fabricated prototypes.

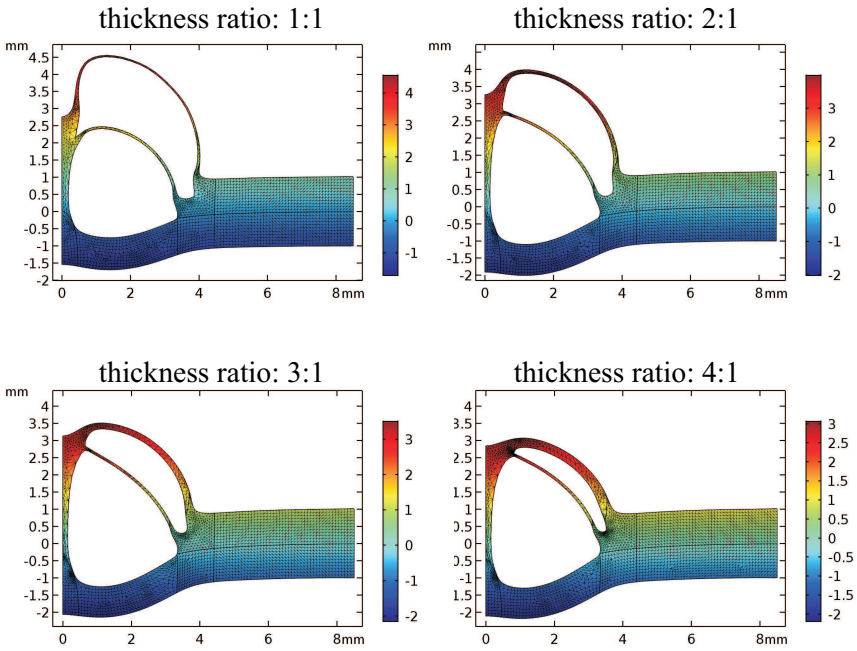

Figure 5.11: Parametric finite element results of the dual-shell glassblowing simulations at different cap/device thickness ratios. The device thickness was 100 μm, the device radius was 4.5 mm, and the cap shell radius was 5 mm in all cases.

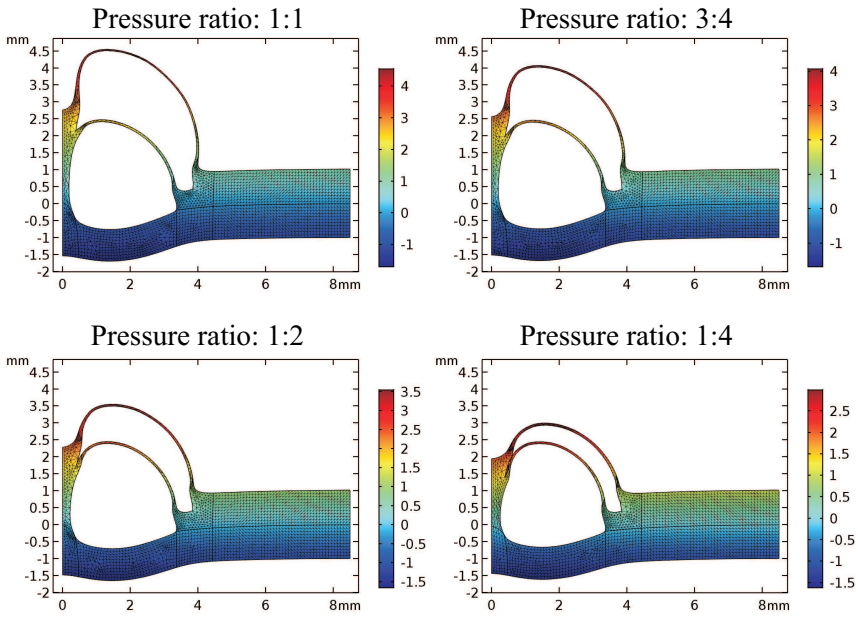

Figure 5.12: Parametric finite element results of the dual-shell glassblowing simulations at different cap/device pressure ratios. The cap and device thickness were 100 μm, the device radius was 4.5 mm, the cap shell radius was 5 mm, and the device cavity pressure was 1 atm in all cases.

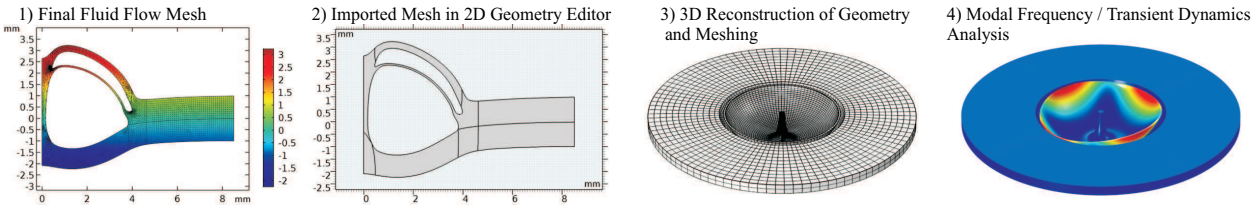

Figure 5.13: Reconstruction of the dual-shell 3D geometry from the final mesh of fluid flow simulation. The imported mesh was edited in geometry editor and the substrate was trimmed to release rim of the inner shell.

5.4.2 Modal Analysis

There are six geometry design and four process parameters in the dual-shell fabrication processes, Table 5.1. For an efficient design of experiment, it is crucial to estimate the modal frequencies of the operational and the spurious vibration modes of the vibrating (inner) shell when designing the dual-shell resonators as opposed to a trial-and-error experiment approach. Since the fluid flow simulations accurately predicted the geometry of glassblown dual-shell prototype, it was employed to construct a 3D geometry for the modal analysis. The mesh from the final time-step of the fluid flow simulations was imported into a CAD editor, the substrate region was trimmed, and the 3D dual-shell geometry was created by revolving the 2D model around its axis of symmetry. The modal analysis module of COMSOL Multiphysics was used to perform the frequency simulations. The fixed boundary conditions were applied to the inner stem and planar extension of the outer shell, the material properties of solid Fused Quartz (Young's modulus (E) of 73 GPa, Poisson's ratio (ν) of 0.17, and density (ρ) of 2220 (kg/m^3) were assigned to the solid domains, and the 3D geometry was meshed with swept meshing technique. Fig. 5.13 illustrates the steps of simulation from the fluid flow mesh to the modal analysis results. This framework provides a full cycle to design the operational frequency of the dual-shell resonators from geometry and process parameters.

Table 5.2: Comparison of FE prediction and measurements on the fabricated dual-shell prototype.

Parameter	**FE Simulation**	**Measurement**
Rim thickness (um)	86.2	86.2
Stem radius (mm)	0.32	0.48
Inner shell radius (mm)	3.33	3.24
Outer shell radius (mm)	4.06	3.9
Total dual-shell height (mm)	2.57	2.67
Resonant frequency (kHz)	8.7	9.6

5.4.3 Design Considerations for Robustness to High-g Shock

One of the primary advantages of the dual-shell resonators is an enhanced the robustness of micro-shell resonator gyroscopes by providing additional support through the anchored cap shell. The fixed-fixed anchoring of the device shell increases the bending stiffness of the stem, thus the resonant modes which are sensitive to in-plane linear acceleration would shift to higher frequencies. The design of cap anchor radius, referring to Fig. 5.8, dramatically influencing the stiffness of tilt as well as out-of-plane, and rotation modes. Indeed, the cap shell stem radius defines the anchoring condition for the resonating shell. Fig. 5.14 demonstrates the results of glassblowing simulations for different cap anchor radius. All other design and process parameters were constant in these simulations. The simulations show that a larger cap anchor radius results in a larger fixed area on top of the resonating shell. In this configuration, the n=2 wineglass mode can be designed to operate at relatively low frequency (5 kHz to 20 kHz), while the bending, tilt, out-of-plane, and rotation modes will shift to higher frequencies (above 50 kHz). The transient response of dual-shell geometries in Fig. 5.14 was simulated using the method described in Section 5.4.2. An extreme shock load with an amplitude of 50,000g and shock duration of 10 ms was modeled with a half-sine acceleration and applied to the dual-shell geometries along the in-plane (horizontal) and out-of-plane (vertical) direction. The maximum displacement and tensile stress for each case are presented in Table 5.3. The response of a single shell geometry to the similar transient dynamic load was also listed for comparison. The transient dynamics simulation

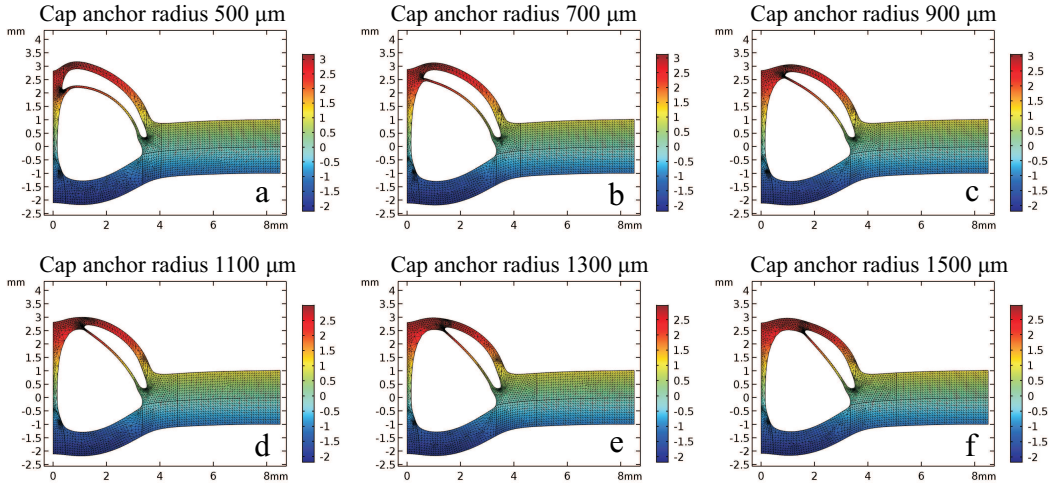

Figure 5.14: Parametric finite element results of the dual-shell glassblowing simulations with different cap anchor radius. The cap anchor geometry stiffens the environmentally-sensitive resonant modes.

Table 5.3: The transient dynamic simulation results of the dual-shell geometries shown in Fig. 5.14 under 50,000g shock amplitude with 10 ms duration.

	n=2 mode frequency [kHz]	Lowest parasitic mode/frequency [kHz]	Vertical shock max. disp. [μm]	Vertical shock max. stress [MPa]	Horizontal shock max. disp.[μm]	Horizontal shock max. stress [MPa]
Single Shell	12.4	tilt / 9,930	7.4	52.9	21.4	64.3
Case a	10.7	tilt / 9.4	5.3	59.3	30	112
Case b	10.9	tilt / 16.9	0.92	39.5	10.6	110
Case c	14.1	n=3 / 25.5	0.5	16	4.03	52.8
Case d	21.7	n=3 / 25.5	0.36	14.6	1.89	23.6
Case e	32.1	n=3 / 28.1	0.29	14.2	1.1	16.2
Case f	45.4	n=3 / 34.3	0.23	14.2	0.73	14

results revealed that the maximum stress will be reduced by an order of magnitude and the maximum displacement will be reduced to sub-micron level, which allows a continuous operation under high shock events without causing a dynamic pull-in instability or physical contact between the sensor and electrode structures.

5.5 Characterization of Dual-Shell Resonators

The frequency response of the released dual-shell resonator prototypes was characterized using a bulk piezo stack for excitation and a Laser Doppler Vibrometer (LDV) for detection. The piezo stack was attached to the outer shell to excite the resonant modes of the dual-shell structure, and velocity of the inner shell at the rim was captured using LDV. The

Table 5.4: Frequency response data of the n=2 and n=3 wineglass modes of the fabricated dual-shall prototypes. Prototypes were fabricated from 3 different wafers denoted by letters A, B, and C.

	n=2 mode			n=3 mode		
Prototype	f (kHz)	df (Hz)	Q-factor	f (kHz)	df (Hz)	Q-factor
#A1	9.671	47.9	262,530	23.263	68.8	1,321,700
#B1	4.905	26.5	945,607	14.581	4.4	1,169,392
#B2	5.499	65.1	1,129,969	16.223	87.6	1,237,700
#B3	4.782	30.9	721,161	13.953	12.7	797,887
#C1	7.914	8.2	313,600	15.638	15.1	1,613,136
#C2	5.456	65.7	1,252,811	15.836	61.6	1,533,332
#C3	6.261	68.2	141,969	16.354	67	862,521
#C4	6.958	30.7	<50,000	19.306	45.1	1,540,475

quality factor of the inner shell was measured in a vacuum chamber at <10 μTorr. The amplitude ring-down time was measured by exciting the wineglass mode at its resonant frequency and abruptly removing the excitation signal. The time that takes the amplitude of vibration to decay to $1/e$ of its initial amplitude in free vibration was recorded as the amplitude decay time constant and used to calculate the Q-factor of the corresponding mode. The resonant frequency, frequency mismatch, and the Q-factor of n=2 and n=3 wineglass modes of four un-coated prototypes with different geometries were listed in Table 5.4. As an example, Fig. 5.15 shows the frequency response of a dual-shell prototype (#B1 in Table 5.4) with the center frequency of 4.9 kHz and an as-fabricated frequency split of 26.5 Hz on the n=2 wineglass mode. The higher-order modes (n=3 and n=4) demonstrated a smaller frequency mismatch. The primary sources of frequency mismatch in micro-glassblown shells are non-uniform heating of the dies inside the furnace, initial thickness variation across a die before glassblowing, and misalignment in the back-lapping step. The unbalanced mass can be compensated using chemical etching, selective ablation using femtosecond laser, or directional lapping [59].

Fig. 5.16 shows the results of Q-factor measurements on a dual-shell resonator. We believe the Q-factor of the un-coated shells were limited by surface losses which originated from the

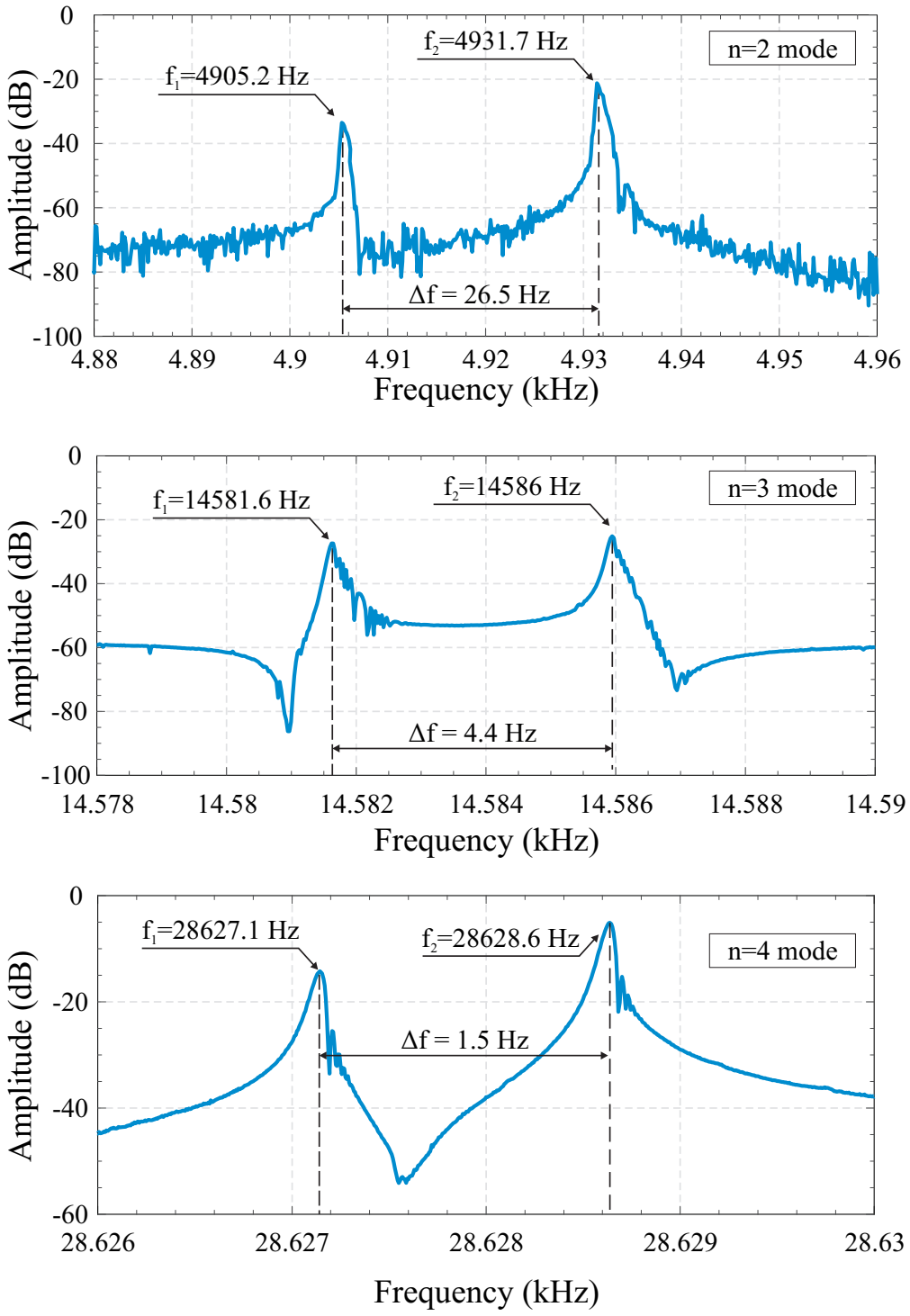

Figure 5.15: Frequency response characterization of a dual-shell prototype (#B1 in Table 5.4) using a bulk piezo stack excitation and LDV for detection, the n=2 wineglass frequency was 4905 Hz with 26.5 Hz frequency split between n=2 orthogonal modes. Smaller frequency mismatches were observed in the higher-order wineglass modes (n=3 and n=4).

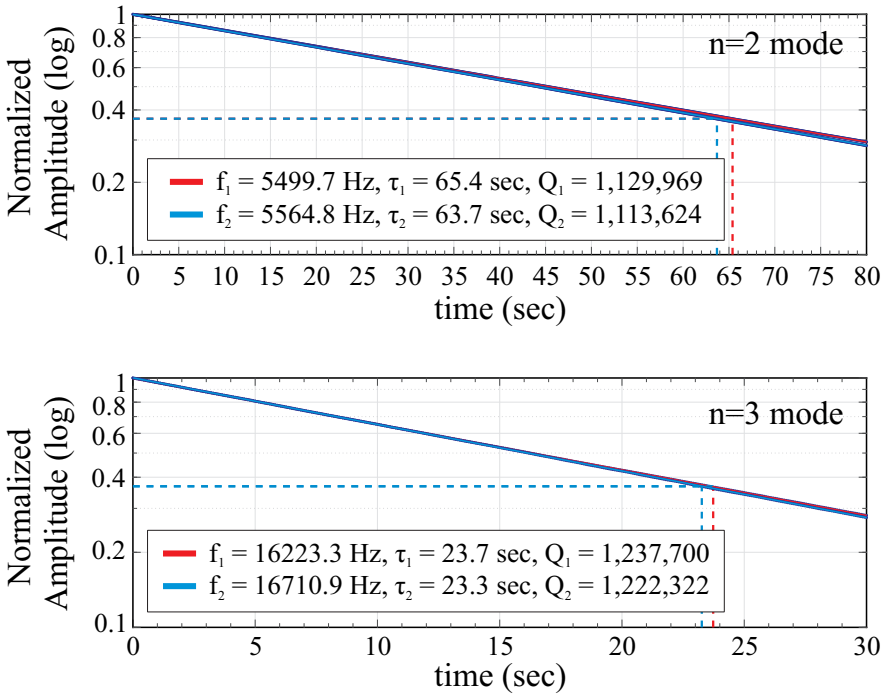

Figure 5.16: Experimental Q-factor measurement of a dual-shell prototype (#B2 in Table 5.4) revealed more than 1 minute of ring-down time on n=2 mode.

quality of the polished surfaces as well as the large surface-to-volume ratio in thin shells and by the residual thermal stresses in the dual-shell resonators which originated from non-isothermal fast cooling after micro-glassblowing.

In some designs, #C3 and #C4, low Q-factor was observed in the n=2 modes and high-Q was observed in the n=3 modes. The energy dissipation through mode-mixing was identified as the limiting mechanism in n=2 modes. It was observed that the wineglass modes were is a close proximity of the higher energy dissipating tilt mode. Fig. 5.17 shows the frequency response of prototype #C4, where the tilt and the n-2 wineglass modes have <300 Hz frequency separation.

Effect of thermal annealing on the Q-factor

As previously discussed in Section 4.3, the thermal annealing of micro-shell resonators reduces the thermal stresses induced by non-isothermal fast cooling after the micro-glassblowing

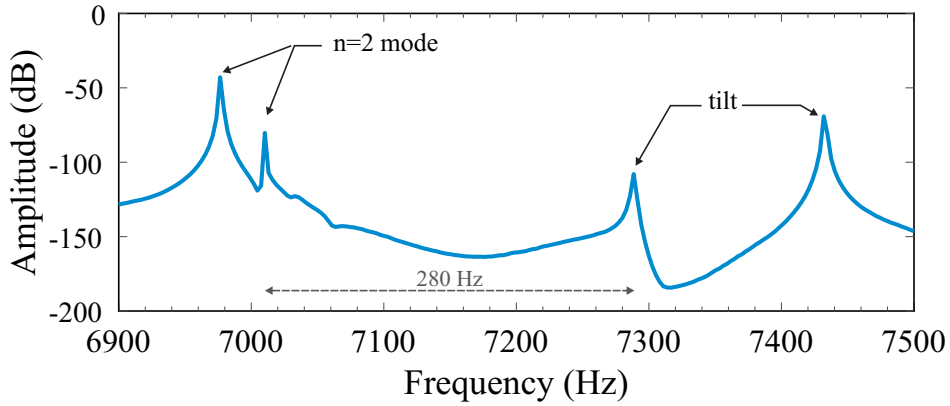

Figure 5.17: Frequency response of the dual-shell prototype #C4, the tilt mode is in a close proximity of the n=2 wineglass mode with <300 Hz frequency separation.

process. An improvement was observed in the Q-factor of micro-shell resonators after thermal annealing. The dual-shell resonators were thermally annealed in the following process:

- Ramping up to 950 ℃ at 0.5 ℃/min.
- Annealing at 950 ℃ for 12 hours under continuous N_2 flow.
- Cooling down to room temperature at 0.5 ℃/min.

Fig. 5.18 shows the amplitude ring-down time in n=2 and n=3 modes of prototype #B3 after the thermal annealing. A ∼2.5x and ∼2.9x improvement was observed on the Q-factor of n=2 and n=3 mode, respectively. Q-factor higher than 1.8 million was measured at 4.7 kHz which corresponds to the amplitude ring-down time of slightly more than 120 seconds. The comparison between Q-factor before and after thermal annealing is given in Table 5.5. Similar to prototype #B3, the Q-factor improvement in the n=3 wineglass mode was observed in prototypes #C3 and #C4. However, Q-factor of the n=2 mode was not noticeably changed. Similar results were observed in prototype #C5 which was annealed directly after fabrication. The Q-factor results after thermal annealing revealed that the limiting mechanism in n=2 mode of prototype #C3, #C4, and #C5 was the mode-mixing. Similar to the discussions in Section 2.2.2, the design parameters of the dual-shell resonators

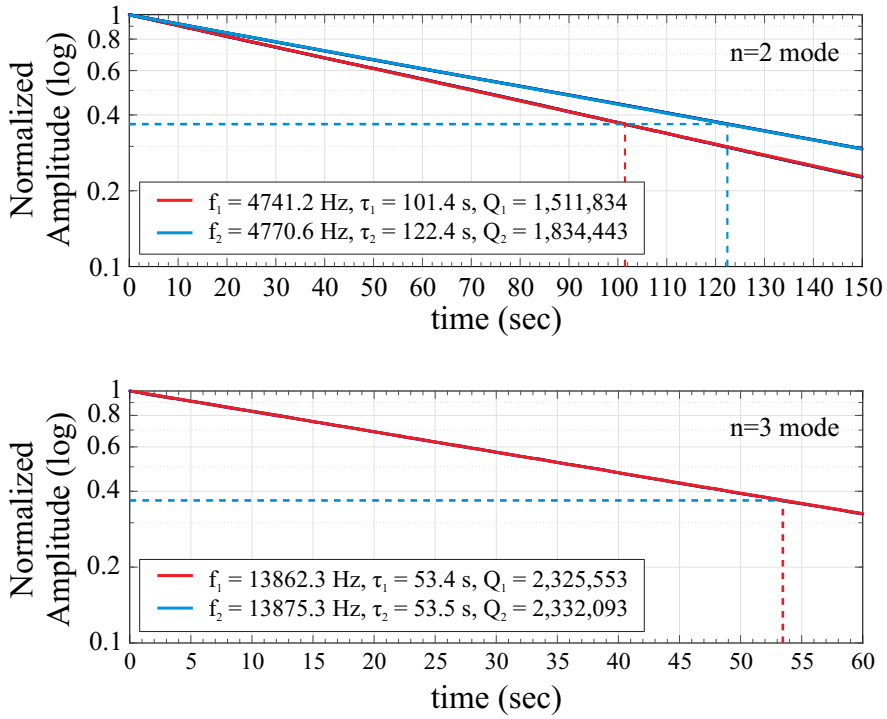

Figure 5.18: Experimental Q-factor measurement of a dual-shell prototype #B3 after thermal annealing. More than 100 seconds ring-down time was measured on n=2 mode.

should be optimized to maximize the modal separation for the operational frequency of interest,

5.6 Integration with Electrode Substrate

The inner shell in a dual-shell resonator is the sensing element, which would respond to an inertial rotation input. The inner shell operates in its fundamental wineglass resonant modes, preferably in the n=2 mode. An electrostatic capacitive excitation and detection schemes were implemented based on the concept of out-of-plane electrodes for excitation of in-plane wineglass modes [2]. In this section, the design and fabrication of the electrode substrate for a dual-shell resonator are discussed.

Table 5.5: Q-factor measurement on thermally annealed prototypes

Prototype	n=2 mode		n=3 mode	
	Q-factor (before annealing)	Q-factor (after annealing)	Q-factor (before annealing)	Q-factor (after annealing)
#B3	721,161	1,834,443	797,887	2,332,093
#C2	1,252,811	1,531,367	1,533,332	3,754,295
#C3	141,969	114,484	862,521	2,392,354
#C4	<50,000	<50,000	1,540,475	2,112,667
#C5	NM*	<50,000	NM*	2,444,735
#C6	NM*	169,539	NM*	2,444,714

*NM: not measured

5.6.1 Electrostatic Excitation and Detection

The configuration of electrodes for the excitation, tuning, and detection of the n=2 wineglass modes on the inner shell is shown in Fig. 5.19. An array of 16 planar electrodes provides 4 electrodes for differential actuation (Fx+, Fx-, Fy+, Fy-), 4 electrodes for differential detection (Px+, Px-, Py+, Py-), and 8 electrodes (Q+,Q-) for off-diagonal electrostatic softening and frequency tuning. The electrode substrate provides a connection to bias the resonator through the central stem and a bonding frame for hermetic bonding and vacuum encapsulation of the inner shell.

The electrode substrate was fabricated using the glass-in-silicon re-flow process, Fig. 5.20. A 500 μm thick double-side polished 4-inch p-type silicon wafer with 0.005-0.02 Ohm-cm resistivity was used for through glass silicon via substrate fabrication. The silicon via structures were fabricated by etching 300 μm deep cavities in a Deep Reactive Ion Etching (DRIE) using a Surface Technology System (STS) Inductively Coupled Plasma (ICP) system. After the chemical cleaning step, the etched silicon wafer was anodically bonded to a 300 μm Schott Borofloat 33 under 10μTorr vacuum condition using the AML-AWB wafer bonder. The re-flow process was performed in a Thermco Ranger 3000 furnace with 10 $^{\circ}C/min$ temperature ramp-up followed by 4 hours dwelling at 850 $^{\circ}C$. The re-flown wafer was cooled down to room

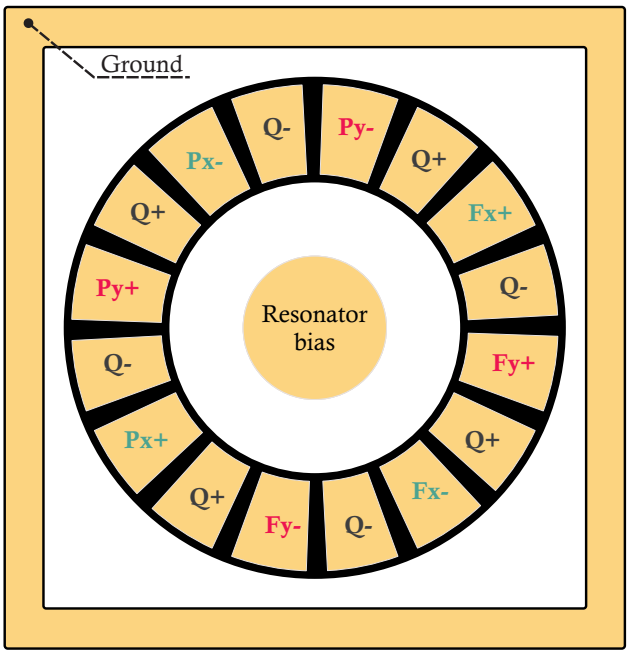

Figure 5.19: The electrode configuration for differential excitation and detection of n=2 wineglass modes, green (Fx+, Fx-, Px+, Px-) and red (Fy+, Fy-, Py+, Py-) indicate excitation and detection electrodes for X- and Y-mode, respectively. The Q+ and Q- electrodes are for frequency tuning and mode decoupling.

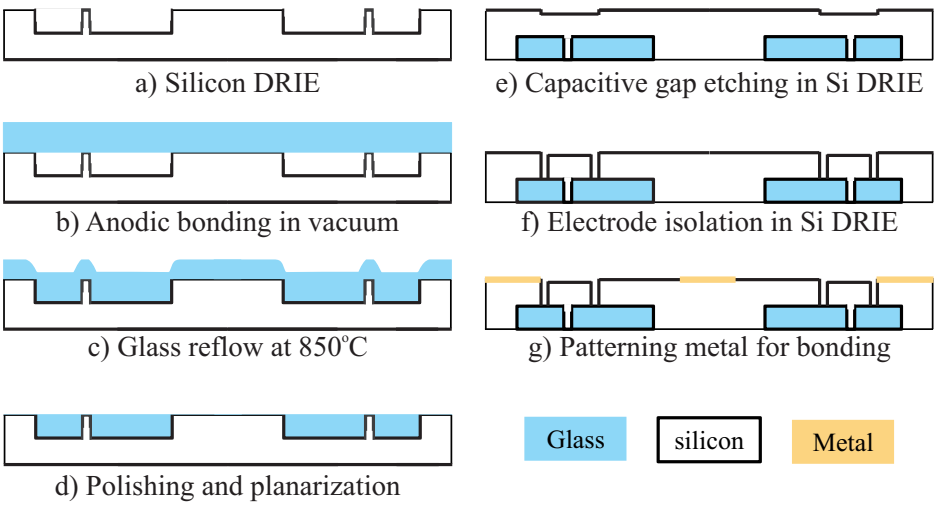

Figure 5.20: Process flow for electrode substrate using silicon-in-glass re-flow. The electrodes were isolated using DRIE of silicon. The out-of-plane capacitive gap was formed by shallow etching of the top electrode surface in an RIE process. The designated bonding areas were coated with Cr-Au for eutectic bonding.

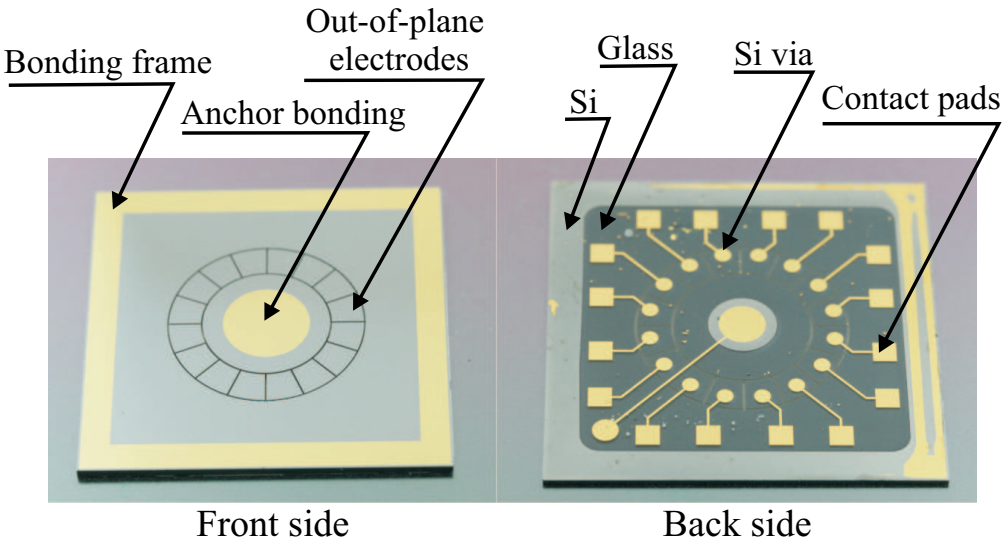

Figure 5.21: The front- and back- side of a planar electrode substrate. The electrodes were isolated by etching trenches in DRIE process to carry the signal through the silicon vias in the re-flown glass. The eutectic bonding areas (outer frame and anchor) are coated with Cr/Au thin films.

temperature at $1°C/min$ rate. The wafer was planarized and the excess glass was ground and polished with the 12-inch Allied HighTech Multiprep polisher. The capacitive gaps for the planar electrodes and isolation trenches were etched using the DRIE process. The wafer was coated with 50 nm chromium (Cr) and 500 nm gold (Au) in an e-beam evaporator, and was patterned to define the anchor and the bonding frame for a subsequent eutectic bonding step. Fig. 5.21 illustrates the front- and back- side of an electrode substrate.

5.6.2 Dual-shell assembly

The fused quartz dual-shell was coated for electrostatic operation and eutectic bonding. The device (inner) shell was coated to bias the resonator through the central anchor. A thin conductive coating consisting of 20 nm Cr and 50 nm Au was deposited on the inner shell. The designated areas for the eutectic bonding, such as the bonding frame and the central anchor, were coated with 50 nm Cr and 500 nm Au, Fig. 5.21.

The eutectic bonding process for assembly with vacuum encapsulation was performed in a

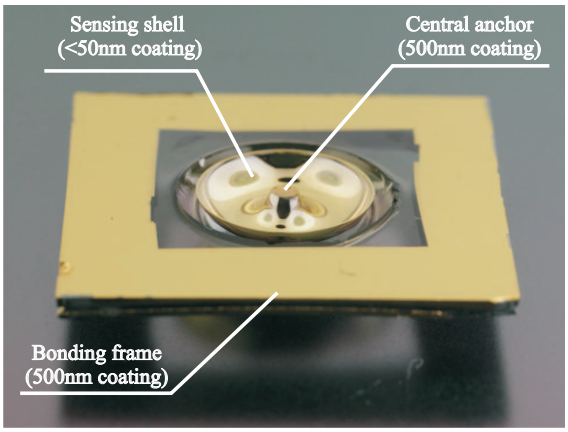

Figure 5.22: A metal coated dual-shell prototype (#A1 in Table 5.4) for the electrostatic operation and eutectic bonding. The shell resonator was coated with (20/50) nm Cr/Au, the bonding frame and the central anchor were coated with (50/500) nm Cr/Au layer using a shadow mask.

SST 3150 furnace. A pre-bake step at 220 $^{\circ}C$ for >24 hours was added before the eutectic bonding of the substrate and the dual-shell. This step was performed in order to reduce the out-gassing after vacuum encapsulation. For an active pumping of residual gasses after vacuum sealing, a getter activation is required. This likely important processing step was not attempted in this study. The getter material can be deposited in the open area of the silicon substrate in future process iterations. Fig. 5.23 illustrates the temperature and pressure profile of the vacuum encapsulation process of a dual-shell device. This parameter optimization study was outside the scope of this work.

Fig. 5.24 shows an assembled dual-shell device on the electrode substrate. The Q-factor of n=2 wineglass mode after assembly and encapsulation was ~92,000. While a reduction in the Q-factor was expected due to metal coating, the measured Q-factor was most-likely limited by air damping. A more effective pre-baking and integration of getter on the electrode substrate would improve the vacuum level and enhance the Q-factor.

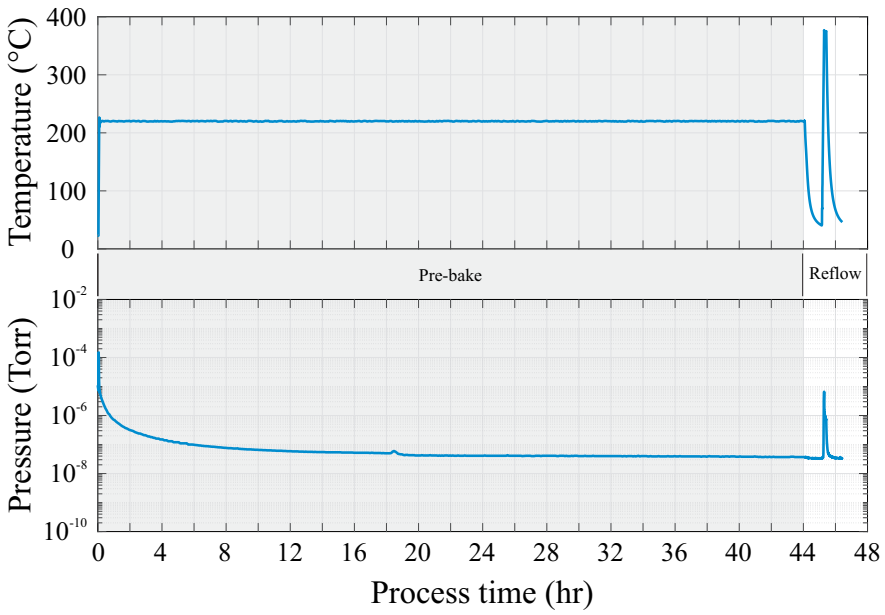

Figure 5.23: The temperature (top) and pressure (bottom) profiles of the eutectic bonding process for dual-shell to electrode substrate assembly in SST 3150 furnace. The process included 40 hours of pre-bake at 220 $°C$ to effectively remove surface-absorbed gases, followed by 10 minutes re-flow at 375 $°C$.

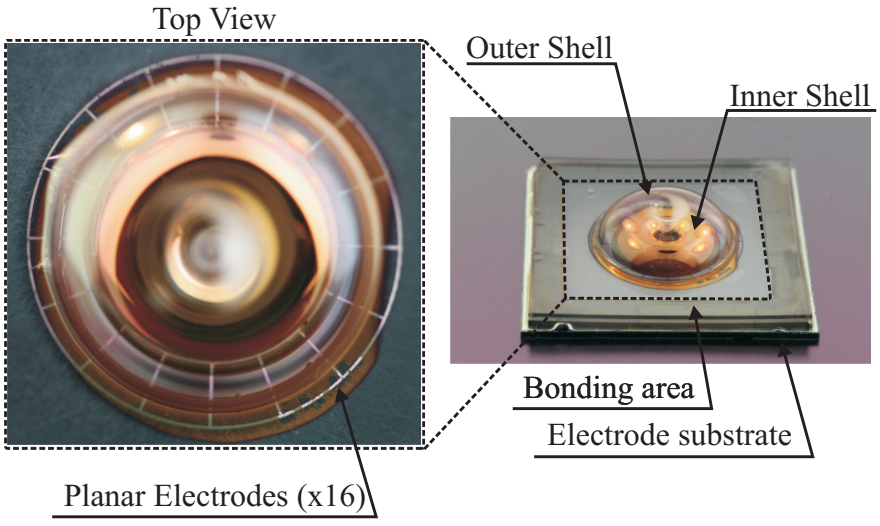

Figure 5.24: An assembled fused quartz dual-shell device (#A1 in Table 5.4)). An array of 16 out-of-plane silicon-in-glass electrodes with $\sim$ 10μm capacitive gap were utilized for electrostatic excitation, capacitive detection, and tuning of n=2 wineglass mode.

5.7 Electrostatic Operation

Electrostatic actuation and capacitive detection were implemented with Electromechanical Amplitude Modulation (EAM) technique to eliminate the feed-through parasitics [98]. An AC carrier signal of 5 V at 200 kHz was applied to the inner shell through the central stem. A differential actuation circuit was implemented on a custom Printed Circuit Board (PCB) to apply DC+AC signal to Fx+ and DC-AC signal to Fx- (similarly to Fy+/Fy-) drive electrodes. A two-stage differential trans-impedance amplification circuit was implemented on the sense channels to detect the signal from Px+ and Px- (similarly Py+ and Py-). Fig. 5.25 illustrates a dual-shell gyroscope mounted on the PCB for electrostatic frequency response characterization.

The AC drive signal of 0.5 Vrms and the DC bias voltage of 5 V were used for the initial frequency response characterization. Fig. 5.26a shows the electrostatic frequency response sweep of the dual-shell gyroscope. Due to the misalignment of the wineglass modes with the orientation of electrodes, two peak frequencies appear in the response plot. The DC voltage of 69.5 V was applied to the Q+ electrodes for off-diagonal tuning. The off-diagonal tuning was used to align the wineglass modes with the drive electrodes, Fig. 5.26b. Finally, to tune the frequency mismatch between the n=2 wineglass mode, a DC voltage of 71 V was applied to the drive electrodes of the Y-axis. A combination of off-diagonal and diagonal tuning voltages reduced the frequency mismatch below 1 Hz (600 mHz), Fig.5.26c.

Testing of the device in the open-loop rate gyroscope operation was performed using an FPGA-based Zurich Instrument HF2LI lock-in amplifier. After carrier demodulation, the Automatic Gain Control (AGC) and Phase-Locked Loop (PLL) control loops were implemented on the drive axis to maintain the drive amplitude, track the frequency of the drive signal, and generate a reference signal for demodulation of sense signal and estimation of rate output, Fig. 5.27. The sensor and the front-end PCB assembly were mounted on a

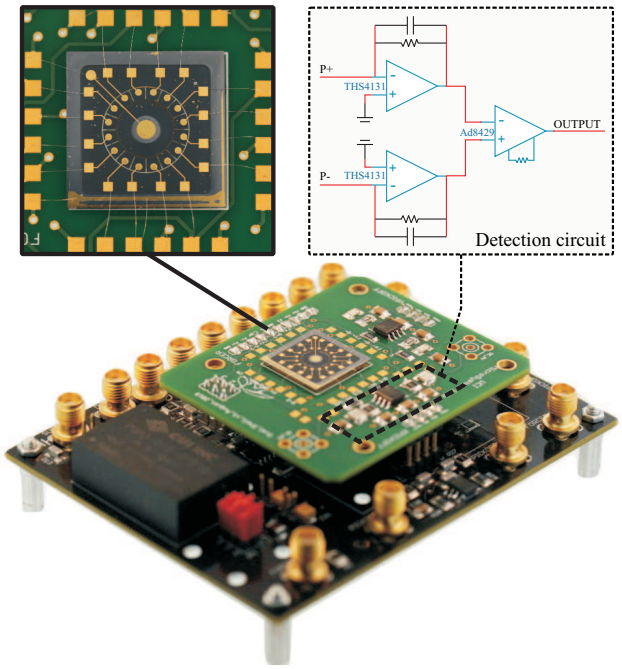

Figure 5.25: An assembled dual-shell resonator mounted (up-side down) on a two-stage signal conditioning PCB assembly. The bottom stage (black PCB) provides the differential drive signals, tuning voltages, and 2nd stage amplification of sense signals. The top stage (green PCB) provides contact pads for wirebonding to silicon-in-glass via electrodes and 1st stage amplification of sense signals.

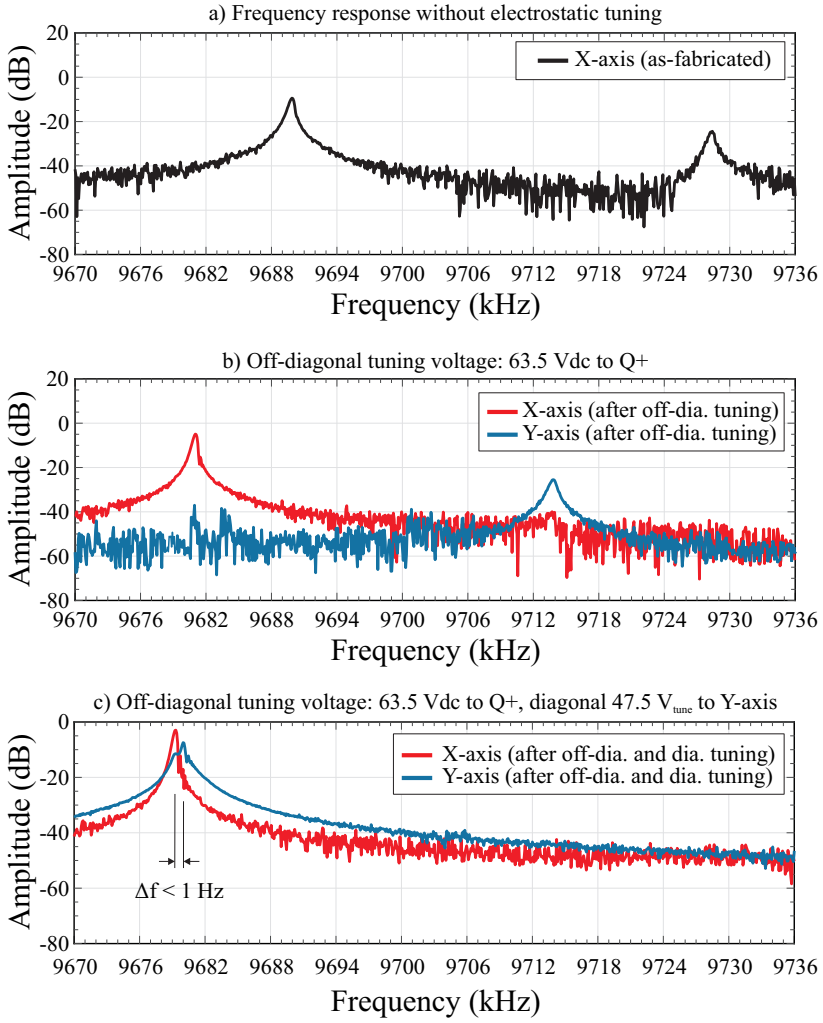

Figure 5.26: (a) An electrostatic frequency response characterization of the as-fabricated dual-shell resonator, (b) off-diagonal tuning voltage applied to Q+ electrodes for mode alignment, (c) electrostatic frequency tuning to less than 1 Hz mismatch using off-diagonal and diagonal tuning.

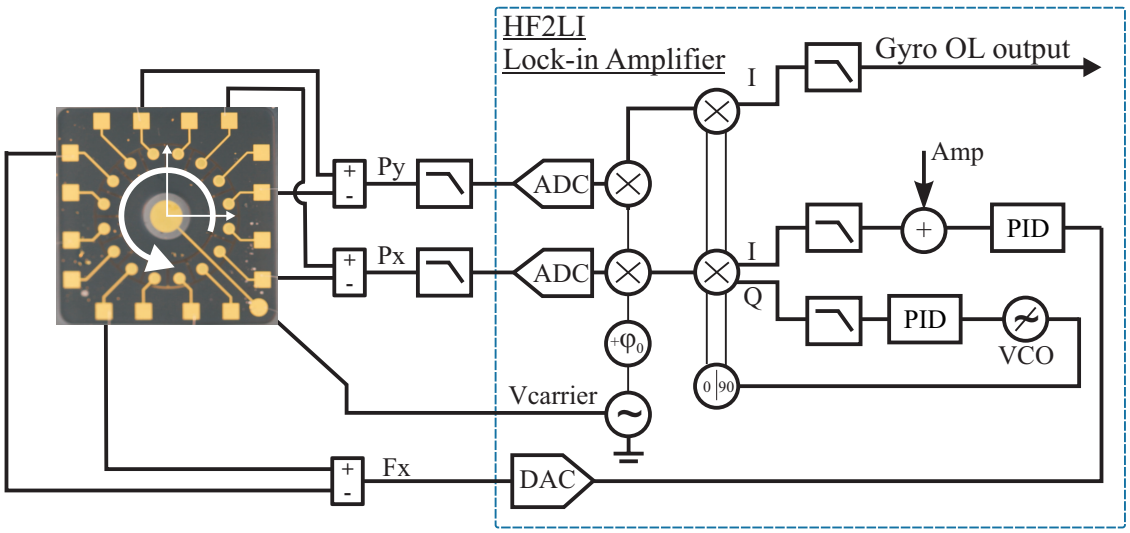

Figure 5.27: Schematics of the primary control loops AGC and PLL established along the drive axis (indicated as X-axis) of the dual-shell resonator gyroscope for the open-loop gyro operation.

2102 Ideal Aerosmith precision rate table. A sinusoidal rotation with a constant frequency of 0.25 Hz at different amplitudes (1, 2.5, 5, 7.5, and 10 [deg.]) was applied, and the output of the dual-shell gyroscope was measured, Fig. 5.28. The linear fit to the input-output plot revealed a scale factor of 1.41 [mV/deg/sec] in a nearly-mode-matched condition with frequency mismatch of $\tilde{6}00$ mHz. An improvement in the scale factor is anticipated with a smaller capacitive gap and improvements in the vacuum-level of encapsulation in future iterations of the dual-shell resonator gyroscopes.

5.8 Conclusion

3D fused quartz dual-shell structures were introduced for microresonators and gyroscopes. The full-cycle development of the dual-shell resonator gyroscopes, including the design, simulation, fabrication, integration, and device operation was presented. The fused quartz dual-shell structures were fabricated using high-temperature glassblowing process. The fabrication of dual-shells using this technique can be scaled to the wafer-level in a high-temperature furnace with a larger uniform temperature zone. A finite element model was developed to

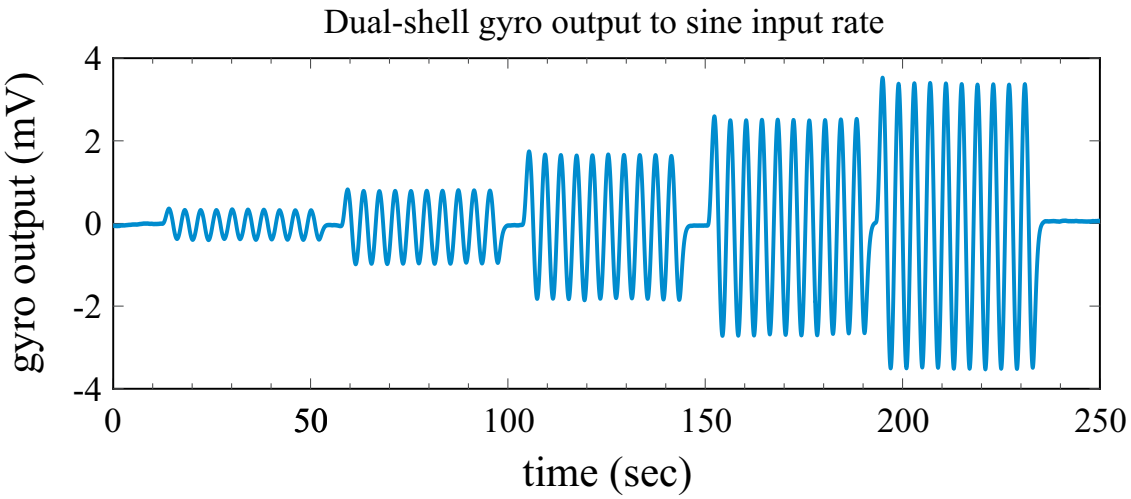

Figure 5.28: An open-loop response of the dual-shell resonator gyroscope to a sinusoidal input rotation with constant frequency of 0.25 Hz at different amplitudes (1, 2.5, 5, 7.5, and 10) revealed a scale factor of 1.41 mV/deg/sec.

simulate the dual-shell glassblowing process. The model predicts the final geometry based on the design and process parameters. The design and process parameters were discussed, and their influence on the final glassblown dual-shell was studied in parametric simulation. The design strategies to improve the shock resilience by reducing the mechanical stress and displacements were discussed, and transient dynamic response simulations were performed to study the different geometries. The dual-shell structure is anticipated to improve the shock resistance and, ultimately, enable gyro operation in harsh environments by enhancing the rigidity of micro-shell resonators and selectively stiffening the spurious resonant modes. A design strategy to improve the robustness of dual-shell resonators under an extreme adverse condition was discussed, and simulation results were presented to confirm the possibility of continuous operation of the dual-shell resonator gyroscope in harsh environments. Several dual-shell resonator prototypes with different geometries were fabricated. A Q-factor of 1.13 million, corresponding to more than 65 seconds amplitude ring-down time was demonstrated on a dual-shell resonator operating at 5.5 kHz. The thermal annealing process was performed to reduce the residual stresses in the dual-shell resonators.An improvement in the Q-factor was observed in the n=2 and n=3 modes after annealing, achieving a maximum Q-factor of 3.75 million at the frequency of 15.9 kHz. An assembly process was developed to

integrate the dual-shell resonators with planar electrodes for electrostatic actuation and capacitive detection. An electrostatic frequency mismatch tuning of n=2 wineglass modes was demonstrated using planar electrodes. Finally, the operation of dual-shell resonator gyroscope in an open-loop rate mode was demonstrated experimentally. The proposed dual-shell architecture can be implemented as a core sensing element with a compact form factor in microresonators and gyroscopes operating through shock and vibration. In this Chapter, we presented the full-cycle development of dual-shell resonator gyroscopes, however geometry optimization, investigation of energy loss mechanisms, and optimization of capacitive gaps have to be performed in future design iterations of the dual-shell devices to experimentally demonstrate the noise performance and shock resilience.

Chapter 6

Study on Quality Factor

6.1 Introduction

In this Chapter, a die-level ultra-high-vacuum sealing process to suppress viscous damping in high-performance MEMS inertial sensors is presented, emphasizing restrictions on materials and temperature compatibility, thus providing the complete information for adapting the process to other MEMS devices. The presented ultra-high-vacuum sealing process can be used as a standalone approach for performance evaluation of dynamic MEMS devices. Silicon-on-Insulator (SOI) Quad Mass Gyroscopes (QMG) [99], were utilized as test structures in the vacuum sealing process development. This chapter also discusses the design and performance characterization of a novel 2D "flat" mode-matched SOI MEMS gyroscope.

6.2 Ultra-High-Vacuum Packaging of MEMS Inertial Sensors

The MEMS resonators and vibratory gyroscopes could reach their fundamental thermoelastic damping (TED) limit in an ultra-vacuum condition where the viscous damping is eliminated. The high-Q and high-performance MEMS gyros, such as Disk Resonator Gyroscopes (DRG) [100], silicon tuning fork resonators and gyroscopes [101, 102, 103], and fused silica 3D shell resonators [1, 86, 104], must operate at high vacuum level for higher sensitivity. Operating in a vacuum chamber or using on-board vacuum techniques, discrete vacuum packaging [100, 102] and wafer-level packaging [105, 106, 107] are the approaches to reduce the viscous damping in dynamic MEMS devices.

High vacuum stability is also required to avoid performance drift in the long run. The pressure inside a sealed cavity evolves during the lifetime of the device. The primary sources of vacuum degradation are the desorption of gas from the internal surfaces (outgassing) and the leakage in the sealing [108, 109]. The outgassing is an unavoidable phenomenon and, from the thermodynamic point of view, is a result of a complex gas-solid interaction inside a hermetically sealed package [110]. The outgassing rate highly depends on the initial concentration of physically adsorbed gas molecules on the solid surface. Thus, selecting vacuum compatible and low outgassing materials for fabrication and packaging, and including the pre-baking step is shown to reduce the outgassing rate. However, the pressure, caused by outgassing in the long run, can only be compensated by integration and activation of getter inside the sealed cavities. An effective activation of getter increases its pumping efficiency, resulting in long-term vacuum stability. Besides, defects in the sealing area, such as air voids or micro-cracks on interfaces, would allow gas molecules entering the cavity, evolve the pressure during the lifetime of the device. A defect-free sealing can be obtained by appropriate treatment of packaging components and suitable parameters selection of the sealing process.

In a successful MEMS vacuum sealing, it is critical to adjust the temperature profile of pre-bake, getter activation, and solder reflow processes to achieve long-term vacuum stability. An ultra-high vacuum sealing requires a long pre-baking of components to sufficiently reduce the concentration of trapped gases and water vapor molecules from the internal surfaces. The number of remained molecules depends on the temperature and duration of the pre-baking process. Integration of non-evaporable getter enables pumping of residual gas molecules, maintaining a stable vacuum level during the lifetime of the device.

6.2.1 Material Selection and Handling

In this work, Ceramic Leadless Chip Carrier packages, Kovar lids with a thin film deposited getter (PaGeLid SAES), and Gold-Tin (AuSn 80/20) eutectic alloy solder preforms were used for vacuum packaging of QMG devices. Fig. 6.1 shows an exploded view of all the parts of a vacuum packaged MEMS sensor. A 2 μm thin-film PaGeLid getter was deposited on the inner surface of the Kovar lids, forming the total getter area of 140 mm^2. All the packaging parts were stored in desiccating cabinets before the sealing process to reduce any surface adsorption. The cleanliness and vacuum compatibility of materials used for the device packaging dramatically influence the yield of vacuum packaging process.

6.2.2 Eutectic Die Attachment

LCC packages were initially baked at 400 ℃ for 7 to 10 hours in high vacuum (<1E-5 Torr) to remove the gas molecules trapped during the production of packages. The sensors were attached to LCC packages using AuSn eutectic preform in a UniTemp RSS-160 reflow chamber. A 2-mm diameter circular Cr/Au (50nm/300nm) was patterned on the backside of SOI dies for eutectic die attachment [111]. The eutectic die attachment was performed at 375 ℃ for 20 minutes under 15 kPa pressure applied to the bonding area. The process was optimized to obtain a void-free attachment. Otherwise, the trapped air voids in the die

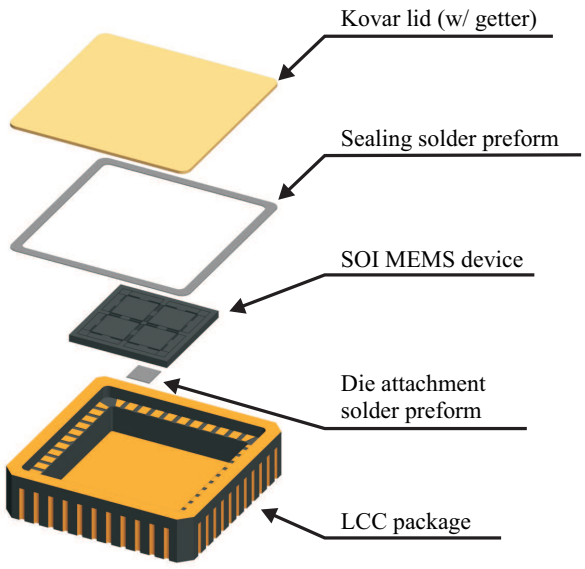

Figure 6.1: Exploded view of materials used for vacuum sealing process.

attachment area would act as an outgassing source after vacuum sealing.

6.2.3 Sealing Solder Preform Tack-Welding

The sorption capacity of the getter is directly related to the getter activation temperature. A higher relative pumping capacity can be reached at higher getter activation temperatures. The getter activation temperature is higher than the sealing solder eutectic point. The preforms were tack-welded to the LCC package seal ring using low-power resistive welding with parallel electrodes. This step was critical to activate the getter at high temperatures without interfering with the sealing solder preforms. For each tack-welding spot, 25 watts power was applied for 25 milliseconds. Fig. 6.2 shows the tack-welding setup (left) and a packaged device with solder preform attached to the package with three welding spots on each side (right).

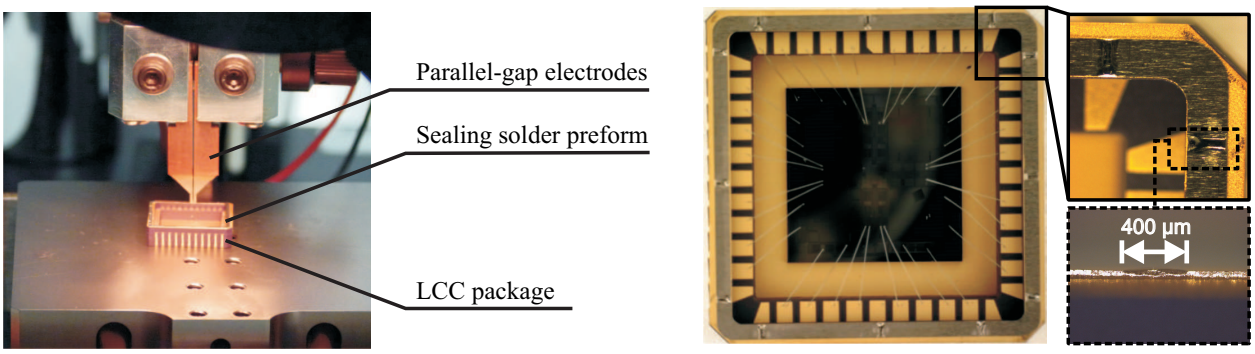

Figure 6.2: (Left) a low power tack-welding setup to attach AuSn sealing solder preform frame to the seal ring of an LCC package. (Right) an LCC package with sealing solder preform attached using tack-welding, a magnified view of welding spots (top-right), a side view of a welding spot showing ~ 400 μm width of the heat affected zone.

6.2.4 Vacuum Sealing Process Development

An SST 3150 high-vacuum furnace was utilized for vacuum sealing of MEMS sensors. This furnace is equipped with a turbomolecular drag pump and a cryogenic water pump and can reach a base pressure of 1E-8 Torr. A customized graphite fixture assembly was used to accommodate LCC packages and Kovar lids. A schematic of the graphite fixture is illustrated in Fig. 6.3. Lids were placed on the boat" plate, with getter facing up. The boat plate temperature rises with the amount of current passing through the plate; the main thermocouple of the furnace was inserted into the boat plate for the thermal feedback control loop. LCC packages were loaded upside down on the "lift" plate. Two additional thermocouples were attached to an LCC package and a Kovar lid for temperature monitoring of parts during the process development. A lift mechanism, inside the furnace, controls the separation between the boat plate and the lift plate.

Fig. 6.4 illustrates the separation of the boat and the lift plate at each step of the sealing process. During the pre-bake step, the lift plate was placed close to the boat plate. The temperature during the pre-bake step was adjusted to ensure effective desorption of gas and water molecules from the surfaces while avoiding a pre-mature activation of the getter. The

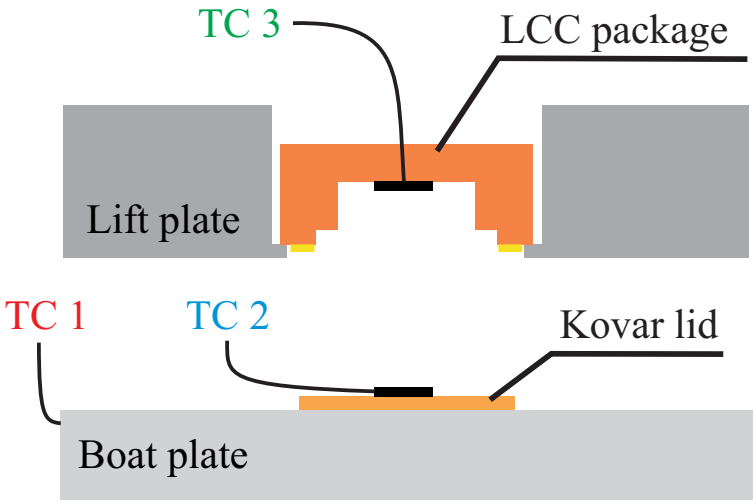

Figure 6.3: Schematics of the graphite tooling assembly and temperature reading setup; additional thermocouples (TC) were used during the process development.

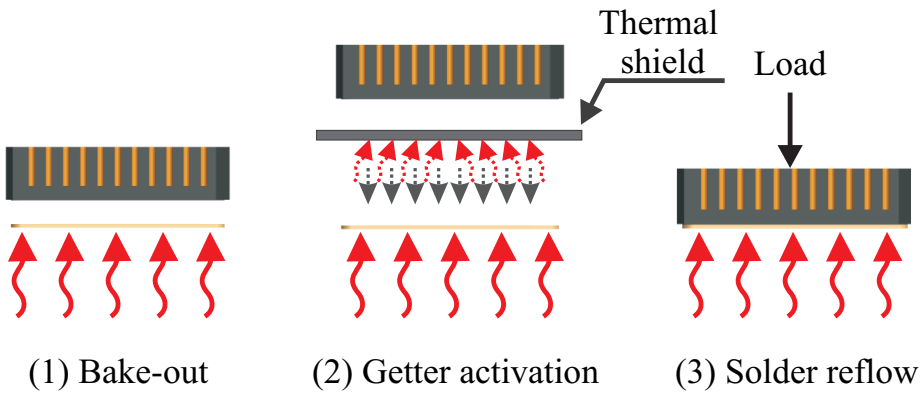

Figure 6.4: Configurations of lids and packages throughout the sealing process, with in-situ getter activation; (1) packages are near the heat source during bake-out, (2) a thermal shield isolates the package and solder frame from overheating during getter activation, and (3) package is pressed against the lid during eutectic bonding.

target temperature for pre-bake was chosen to be 200 ℃, for a prolonged duration of more than 24 hours.

Fig. 6.5 illustrates the temperature profile of the sealing process accompanied by direct temperature readings from Kovar lid and LCC package. An in-situ getter activation followed the pre-bake step, before the lid sealing. The minimum getter activation temperature was 300 ℃. However, the activation of getter at higher temperatures would improve its gas sorption performance [110]. Increasing the getter activation temperature may cause reflow

Table 6.1: Vacuum sealing process parameters (using SST 3150)

Parameter	Pre-bake	Getter activation	Solder reflow
time	>24 [hr]	40 [min]	8 [min]
Process temperature [℃]	225	445	360
Lid temperature [℃]	205	348	344
LCC temperature [℃]	185	231	315

of the sealing solder preform on the package before bringing it in contact with the lid. Thus, temperature of the package during the getter activation should be maintained with a margin of safety below the reflow temperature of AuSn eutectic alloy, which is 278 ℃. Under the high-vacuum condition, thermal radiation is the main heat transfer mechanism. Radiation of heat from the boat plate would increase the temperature of the lift plate and could thermally damage the solder preform at higher temperatures. A shutter mechanism, integrated inside the furnace, thermally shields the packages from overheating. The thermal shielding, combined with tack-welding of solder preforms to the packages, protects the reflow of sealing solder preform and enables activation of the getter at a higher temperature. The getter was activated at 350 ℃for 40 minutes. Fig. 6.6 shows the chamber base pressure readings at the getter activation and the sealing steps. The pressure spikes to 20 μTorr during the getter activation. After the getter activation, the chamber was cooled down by forced convection to reduce the base pressure to less than 0.1 μTorr before lid sealing.

The temperature profile of the solder reflow step was adjusted to achieve a defect-free eutectic bond between the lids and packages. X-ray imaging was utilized to inspect the seal ring after vacuum sealing and detect any air voids. The void formation and growth was reduced by modifying the temperature-time profile of the pre-bake and lid sealing. Formation of many air voids in the sealing area indicates an insufficient pre-bake of package and lids. Excessive time and temperature of solder reflow step form large and grown air voids, which eventually causes leakage in the sealing area. The optimum time and temperature of the sealing step were adjusted in our process to fully reflow the eutectic solder frame with the minimal air void formation. The parameters of each step are summarized in Table 6.1.

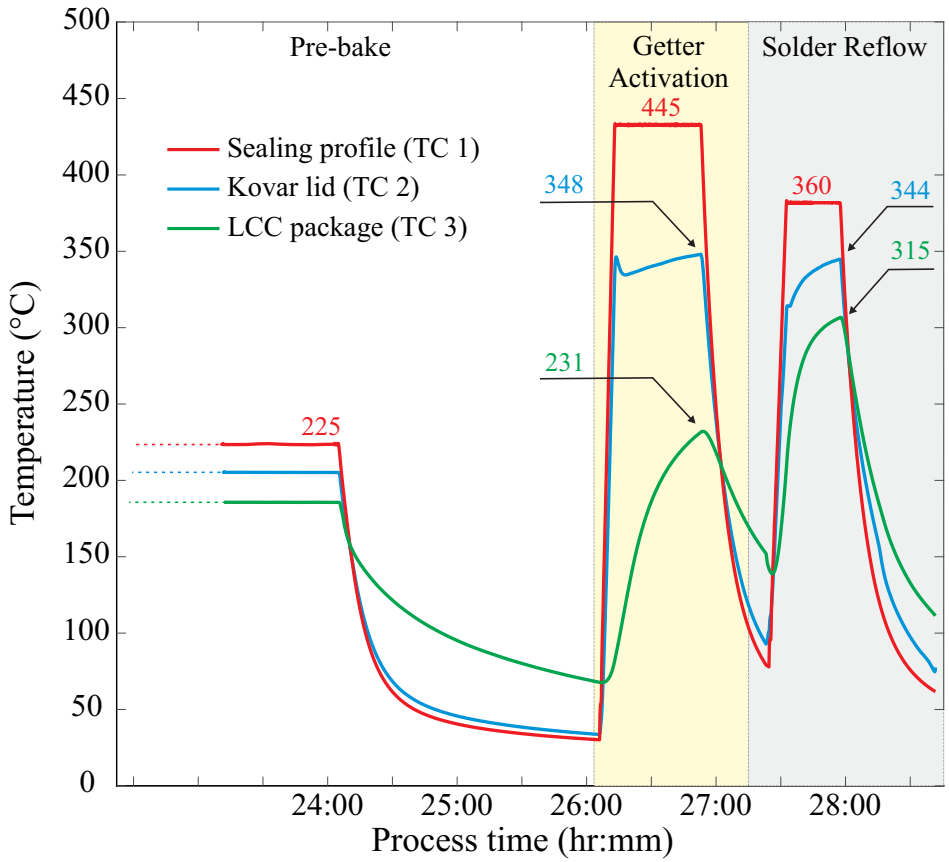

Figure 6.5: Temperature profile of the sealing process (red) with simultaneous temperature recording from the package (green) and the lid (blue).

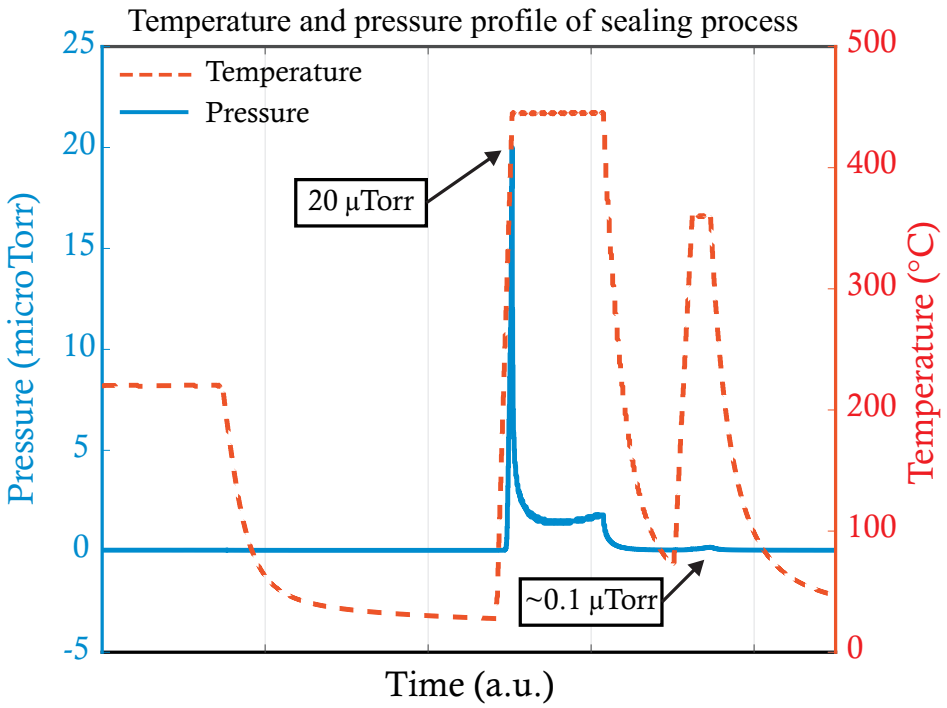

Figure 6.6: Chamber base pressure of 20 μTorr and 0.1 μTorr at getter activation and lid sealing step, respectively.

It should be noted that devices undergo a thermal cycle during the sealing process. Indeed, the temperature compatibility of materials with the process temperature should be considered for adapting this process for other MEMS structures.

6.2.5 Q-factor Measurement Over Time

QMG sensors were initially characterized in the vacuum chamber before vacuum sealing. The Q-factor was measured using energy decay time at different vacuum levels and was used as a reference for vacuum assessment after sealing. The Q-factor was monitored after vacuum sealing. Fig. 6.7 demonstrates the Q-factor evolution of two sensors sealed with different pre-bake durations. It was observed that the Q-factor after sealing reached over 2 million for sensor No. 1 with 24 hours pre-baking, whereas the maximum Q-factor on the same sensor in the vacuum chamber was 0.5 million at 0.2 millitorr.

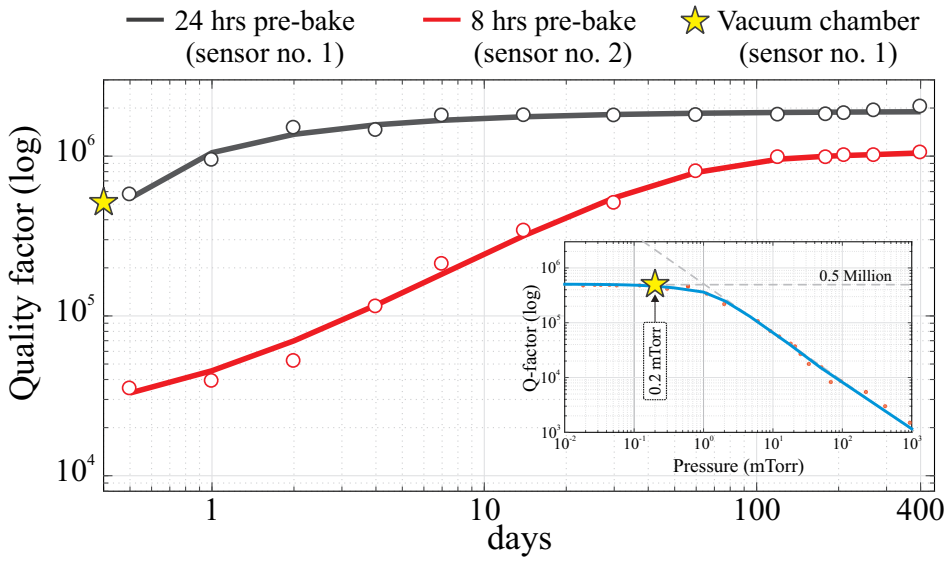

Figure 6.7: The Q-factor measurement over a period of one year after vacuum sealing of two devices with different pre-bake durations. Inset: the Q-factor of sensor #1 was measured in the vacuum chamber, showed maximum Q of 0.5 million at 0.2 millitorr.

This results also revealed an improvement of the Q-factor over time in both cases, which indicates continuous sorption of residual gas molecules by the activated getter. Besides, these results demonstrated that longer pre-baking reduces residual gas molecules inside the hermetically sealed package, enabling a more effective getter pumping and achieving a higher vacuum level after sealing. This phenomenon is discussed and numerically simulated in [110], showing a similar trend with the experimental results in Fig. 6.7. The results also showed a stable high Q-factor over one year, revealing long-term stability of ultra-high vacuum level after sealing.

Fig. 6.8 shows the ringdown time experiment of a sealed sensor, one year after sealing, demonstrated over 380 seconds of energy decay time, revealing over 2 million Q-factor, approaching the TED limit of the sensor structure (2.9 million from FEA for this design), thus demonstrating the effective elimination of air damping. The high Q-factor in the QMG devices is attributed to: 1) its balanced anti-phase mode of vibration, [99], 2) mode ordering, 3) sufficient separation of operational and parasitic modes, [112], and 4) ultra-high-vacuum device sealing, [113]. These are the conditions required to reach the near-navigation grade

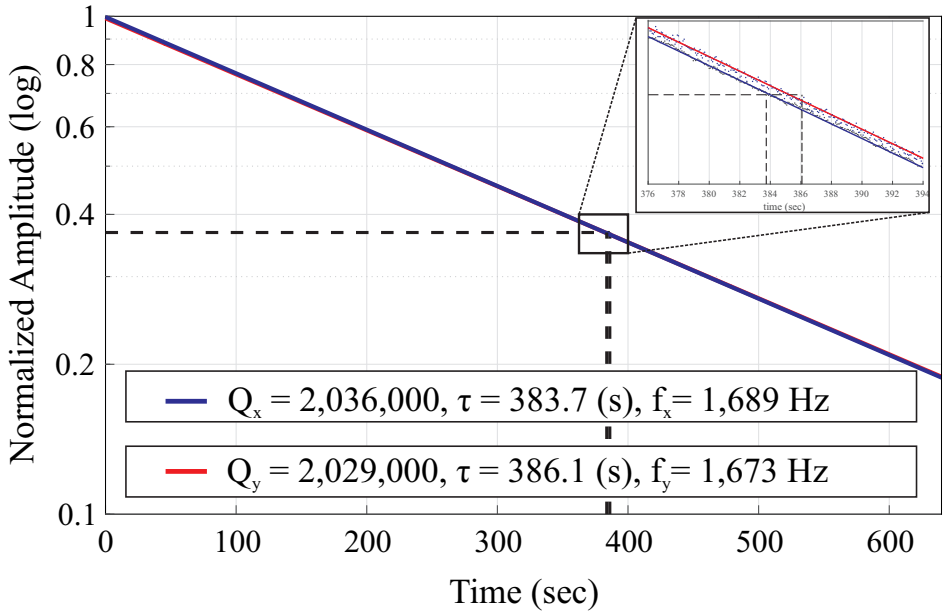

Figure 6.8: Ringdown time measurement of a sealed QMG sensor one year after vacuum sealing, revealing a Q-factor higher than 2 million on both modes.

performance of gyroscopes. Details of the tested device were published in [4]. The hermeticity of the seal was tested according to MIL-STD 883 method 1014. Sealed packages were bombarded by Helium (He) gas for 5 hours at 60 psig. The detected leak rate was ∼3.1E-8 (mbar l/s), which was at the limit of the testing equipment. The Helium leak test results demonstrate the hermeticity of the seal.

We demonstrated a reliable and repeatable μTorr vacuum level in a Ceramic Leadless Chip Carrier (CLCC) packages and achieved the Q-factor over 2 million on a Quad Mass Gyroscope (QMG) and the Q-factor over 1 million on a mode-ordered Dual Foucault Pendulum, approaching the TED limit of both devices by effectively eliminating the viscous damping. The long-term vacuum stability was characterized over three years and demonstrated the Q-factor does not degrade over time, and even continues improving after vacuum sealing until it reaches a stable steady-state vacuum level. The long-term ultra-high vacuum condition was enabled by surface desorption before sealing, pumping of residual gas molecules by passive getters, and defect-free solder reflow in the sealing area. The experimental results confirmed the reliability and repeatability of the proposed sealing procedure, which can be

adapted for other MEMS sensors with ultra-high vacuum requirements.

6.3 Mode-ordered Dual Foucault Pendulum

In this Section, we present the design, implementation, and characterization results of a modified design of the Dual Foucault Pendulum [114]. The test structure was designed to study the sources of energy dissipation mechanisms in compact size SOI MEMS gyroscopes.

6.3.1 Introduction

In the tuning fork microresonators and gyroscopes, two (or more) proof masses are mechanically coupled by flexural springs and driven in anti-phase motion [115]. The tuning fork MEMS gyroscopes operated in a degenerate mode (mode-matched), demonstrated high sensitivity to the input rotation and low-noise performance [116, 117, 118, 102]. The anti-phase motion of the dynamically-balanced tuning fork structures assures cancellation of reaction forces and moments on the anchors, reducing the energy loss through the substrate. However, the additional degrees of freedom in devices with multiple lumped masses introduce spurious frequency modes in addition to the operational mode. These spurious modes can cause leakage of the vibrational energy or be excited by common-mode linear acceleration and vibration.

In this work, a coupling mechanism is implemented on a Dual Foucault Pendulum (DFP) [116] structure that provides large frequency separation between anti-phase and spurious in-phase modes with the anti-phase mode ordered as the lowest frequency mode.

MEMS gyroscopes with multi-degrees of freedom can be implemented in different configurations to improve sensitivity, bandwidth, and vibration immunity [119]. The MEMS vibratory gyroscopes with two (or more) masses and operating in the anti-phase resonance mode, would mitigate the energy dissipation through the substrate by balancing the total

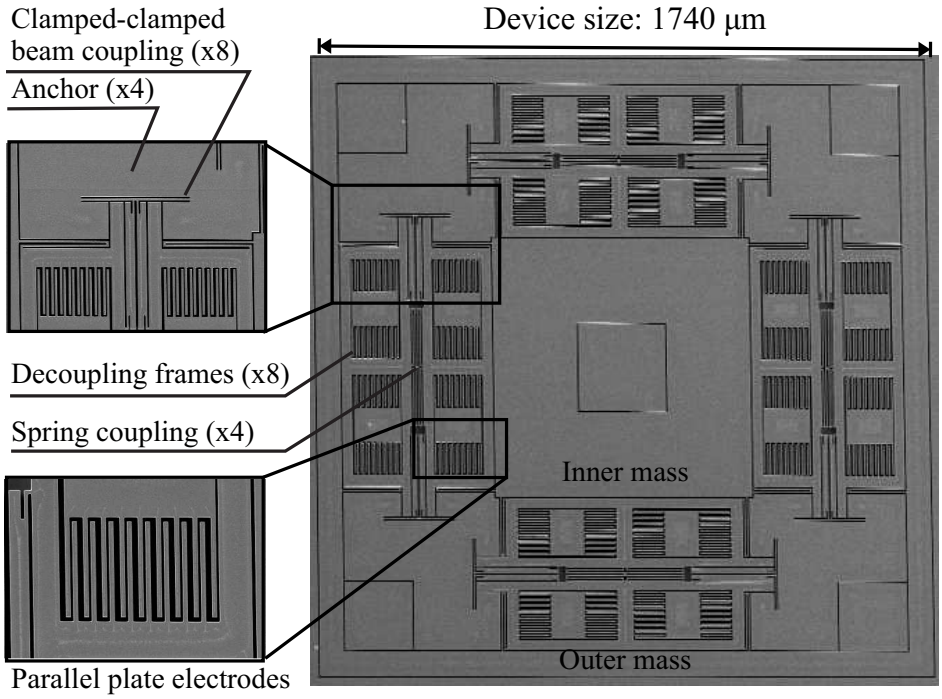

Figure 6.9: Mode-ordered DFP with fully differential parallel plate drive and sense electrodes fabricated using silicon epitaxial encapsulation process. The device footprint is $< 1.8 \times 1.8\ mm^2$.

forces and moments acting on the anchors. Thus, dynamically balanced designs improve the Q-factor, resulting in a higher sensitivity and improved in-run noise performance. Moreover, a large separation between the operational mode and spurious modes minimizes the mode conversion losses from mode coupling due to fabrication imperfections [11]. The TED and mode conversion losses can be mitigated by the geometric and structural design of suspension elements and arrangement of coupling mechanisms.

A Dual Foucault Pendulum (DFP) is a lumped mass-spring type gyroscope which consists of two identical masses and four pairs of identical suspension elements, providing X-Y structural symmetry [120], as well as the ordering of the in-phase and anti-phase resonance modes [103]. The DFP is believed to provide the minimal realization of a mode-matched dynamically balanced lumped mass gyroscope.

In this Section, the mode-ordered DFP device, fabricated on a Silicon-on-Insulator (SOI) wafer using the epitaxial silicon encapsulation process (EpiSeal), was utilized for identifi-

cation and characterization of energy dissipation mechanisms. The device under test was vacuum sealed with getter activation, as described in [103].

6.3.2 Design of Suspension Element for Mode-Ordering

The mode ordered DFP MEMS gyroscope was fabricated on a Silicon-on-Insulator (SOI) wafer with 40 μm device thickness in a wafer-level epitaxial silicon encapsulation process with fully differential parallel-plate electrodes [121]. The X-Y symmetric design of the device consists of two identical proof masses, mechanically coupled using four folded beam springs and anchored through four pairs of internal beam elements. The beam elements clamped at both ends to the anchors, isolating the proof mass motion from the substrate, Fig. 6.9. The parallel plate electrodes were designed with 1.5 μm capacitive gas and 4.5 μm anti-gap, forming an active capacitance of 1.5 pF at each drive and pickoff channel. The parallel-plate electrodes provide fully differential excitation and detection as well as electrostatic frequency tuning. Four pairs of decoupling frames were implemented to restrict the motion of electrodes in one direction and reduce the cross-coupling between the X-axis and the Y-axis.

Fig. 6.10 schematically demonstrates the coupling mechanisms in a regular and a mode-ordered configuration with the clamped-clamped beam element designs. The resonance frequency of the in-phase, ω_{in}, and anti-phase, ω_{in}, in a regular dual mass resonator with two identical proof masses, M, and two identical spring elements, k, and a coupling spring, k_c, are:

$$\omega_{in} = \sqrt{\frac{k}{M}},\ \omega_{an} = \sqrt{\frac{k+2k_c}{M}}. \tag{6.1}$$

The coupling stiffness acts upon the anti-phase mode of vibration, resulting in a higher resonance frequency in anti-phase motion compared to the in-phase motion. The low-frequency in-phase mode makes the gyroscope susceptible to the linear acceleration. Moreover, weak

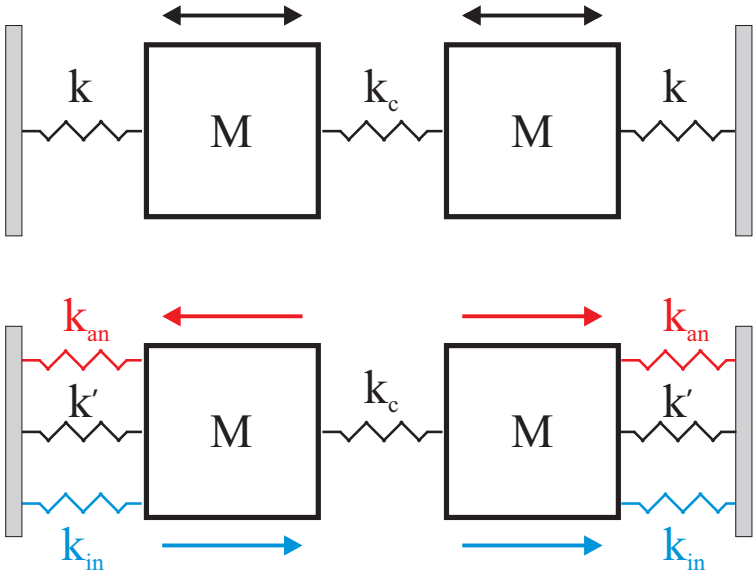

Figure 6.10: (top) Schematic of mass-spring coupling in dual mass gyroscope with a weak spring coupling (k_c), (bottom) a clamped-clamped beam provides different coupling stiffnesses for in-phase and anti-phase modes ($k_{in} > k_{an}$), both cases represent one axis of a dual mass tuning fork gyroscope.

coupling stiffness, $k_c << k$, would bring the resonant frequency of the two modes in close proximity and result in the mode mixing losses.

The concept of using an internal clamped-clamped beam element was implemented in a Quad Mass Gyroscope (QMG) as a negative coupling stiffness between the proof masses in the anti-phase mode [73]. Here, a similar concept was implemented by anchoring the proof masses through a clamped-clamped beam element to impose a different in-phase, k_{in}, and anti-phase stiffnesses, k_{an}. Thus, ordering the anti-phase and in-phase modes of the device. The internal beam resonates at its first flexural bending mode when proof masses move in opposite directions and at its second flexural bending mode when the proof masses move in the same direction, Fig. 6.11. In this case, the resonance frequencies are:

$$\omega_{in} = \sqrt{\frac{k' + k_{in}}{M}}, \ \omega_{an} = \sqrt{\frac{k' + k_{an} + 2k_c}{M}} \tag{6.2}$$

In a clamped-clamped beam, the equivalent stiffness of the beam at its fundamental modes

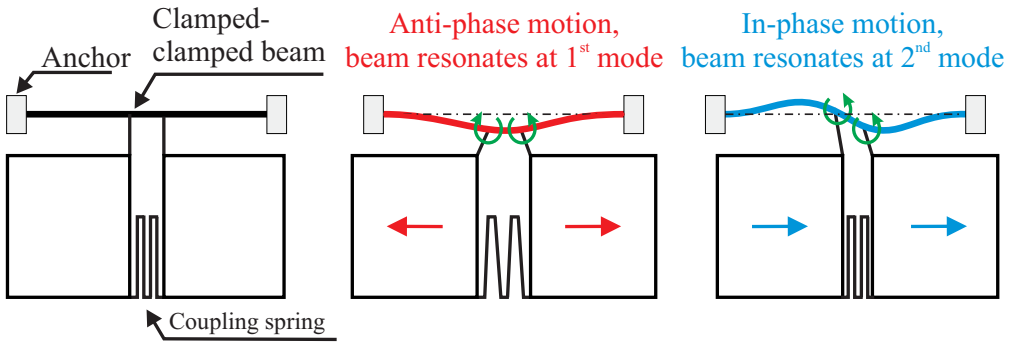

Figure 6.11: The anti-phase and in-phase motion of proof masses excite the first and second flexural bending modes of the internal beam element, respectively.

of vibration are:

$$k_n = C_n^2 \times \frac{EI}{L^4}, \tag{6.3}$$

where n is the mode number, E is Young's modulus of the material, I is the 2nd moment of area, L is the beam length, and C_n is the mode shape parameter of the beam. For a clamped-clamped beam, $C_1 = 22.37$ and $C_2 = 61.67$ impose a different stiffness on the in-phase and anti-phase motion ($k_{in} > k_{an}$). According to Eq. 6.2, the condition for mode ordering, $\omega_{an} < \omega_{in}$, is

$$k_c < \frac{k_{in} - k_{an}}{2}. \tag{6.4}$$

A weak coupling stiffness was configured to provide a large frequency separation between the anti-phase and the in-phase modes. Fig. 6.12 shows the complete layout of the mode-ordered DFP device with the beam coupling element for mode-ordering.

The mode ordered DFP was designed with anti-phase resonance frequency of 20 kHz, as the first operational mode, separated by 12 kHz from the in-phase resonance mode, Fig. 6.13. The device was wire-bonded to a Leadless Chip Carrier (LCC) for characterization. A fully differential drive architecture (push-pull) was implemented using parallel-plate drive electrodes. Electromechanical Amplitude Modulation (EAM) at 300 kHz was implemented to

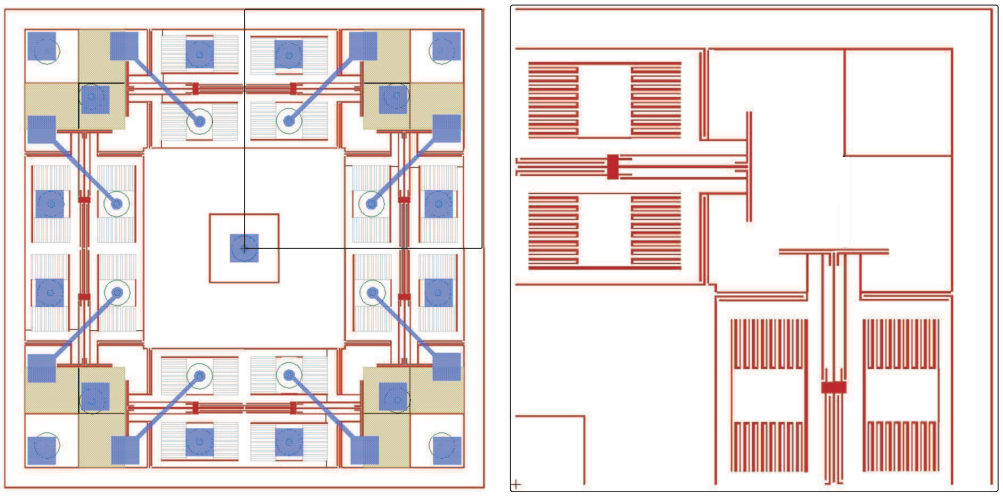

Figure 6.12: (Left) the complete layout of mode-ordered DFP device, the blue color indicates the contact pads and metal traces, the gray color indicates the mechanical anchor points, and the red color indicates the silicon trenches. (Right) A quarter of the device illustrating the beam couplings for mode-ordering.

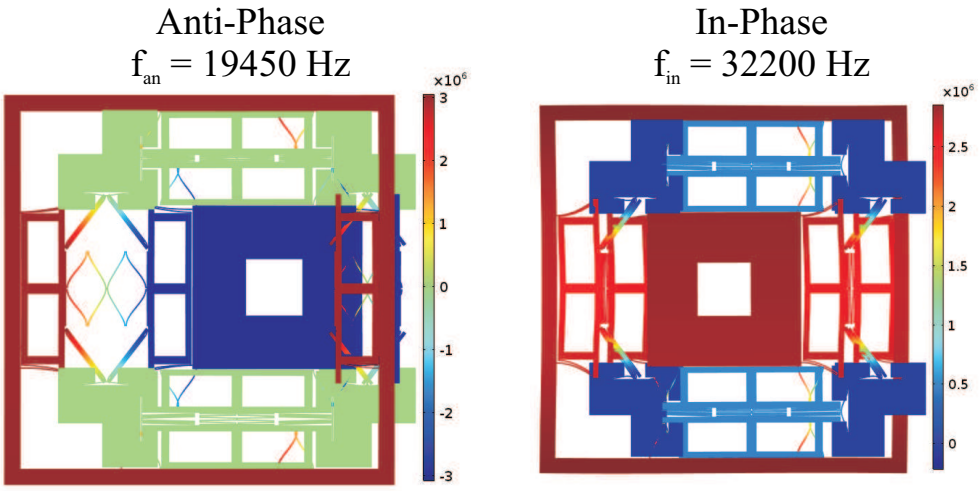

Figure 6.13: Finite element simulation results of anti-phase and in-phase resonance modes of a mode ordered DFP with a clamped-clamped beam element.

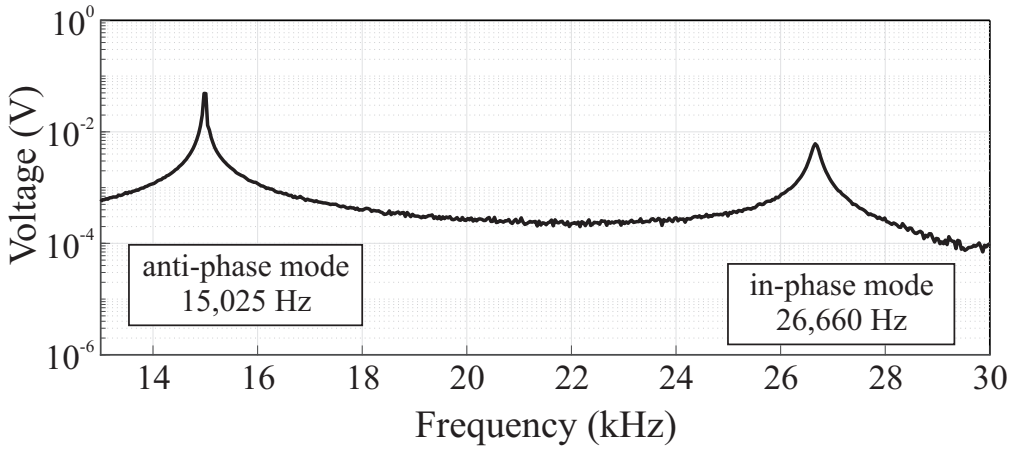

Figure 6.14: Frequency sweep response shows the mode-ordered anti-phase and in-phase resonances with $\sim$ 11.5 kHz frequency separation.

eliminate the feed-through parasitics on the sense electrodes. The AC drive signal of 12 mV and the DC bias voltage of 1 V were used for the initial frequency response characterization. The mode-ordering was experimentally verified from the frequency sweep response, Fig. 6.14. A single-ended output channel was used to detect the in-phase resonance peak. The fabricated device revealed an anti-phase resonance frequency of 15 kHz, which is 5 kHz lower than the designed frequency.

6.3.3 Energy Dissipation Mechanisms

Viscous damping

A ringdown time measurement revealed a time constant of 3.7 seconds, corresponding to a Q-factor higher than 170,000 on both modes. The encapsulated MEMS gyroscope was vented by defining an eight μm vent hole through the cap wafer using Focused Ion Beam (FIB) milling. The characterization of the vented device in a vacuum chamber showed the ringdown time of 17.52 (s) and 17.24 (s) along the X- and Y- axes, corresponding to the Q-factors higher than 820,000 at 20 $\mu Torr$, approaching the Q_{TED} of 1.2 million derived from finite element simulations. The vented device was vacuum sealed with an activated getter for better vacuum stability and rate-table characterization. A thin layer of Cr/Au

Table 6.2: Q-factor of Mode Ordered DFP gyroscope

	Episeal (as-fabricated)	Vented in vacuum chamber at 20 μTorr	Vacuum sealed with getter
X-axis	τ = 2.7 s Q = 127,000	τ = 17.22 s Q = 812,000	τ = 24.5 s Q = 1.16 M
Y-axis	τ = 2.8 s Q = 133,000	τ = 17.52 s Q = 833,000	τ = 23.8 s Q = 1.14 M

(500Å/3000Å) was deposited on the backside of the dies and Gold-Tin (Au80/Sn20) alloy was used for the eutectic die-attachment in the vacuum. The device was re-wire-bonded and vacuum-sealed with getter in an ultra-high vacuum sealing process [113]. The Q-factor reached to the maximum value of 1.15 million after vacuum sealing with getter activation, Fig. 6.15. The Q-factor measurement results are summarized in Table 6.2.

Thermoelastic damping (TED)

A finite element simulation of TED predicted a Q-factor of 1.2 million for the anti-phase mode at the design frequency of 19 kHz. The air damping limited the as-fabricated Q-factor to 130,000 at the encapsulation cavity pressure (0.3 mTorr [122]). The viscous damping was effectively suppressed by vacuum packaging using an ultra-high vacuum sealing process, resulted in achieving the Q-factor at the TED limit.

According to a simplified cantilever beam model by Zener [123], the Q_{TED} strongly depends on the Coefficient of Thermal Expansion (CTE) of the resonator's material. Since the CTE of Silicon depends on temperature, TED can be controlled by temperature and can be effectively eliminated when the CTE crosses zero [15].

A cryogenic probe station (Lake Shore FWP6) was used for the measurements at low temperature. The sealed DFP device was cooled down to 80K, and the Q-factor was measured along both X- and Y- axes of the gyroscope. Fig. 6.17 demonstrates that Q-factor increases at low temperature and approaches its peak value near 110K. At this temperature, where the

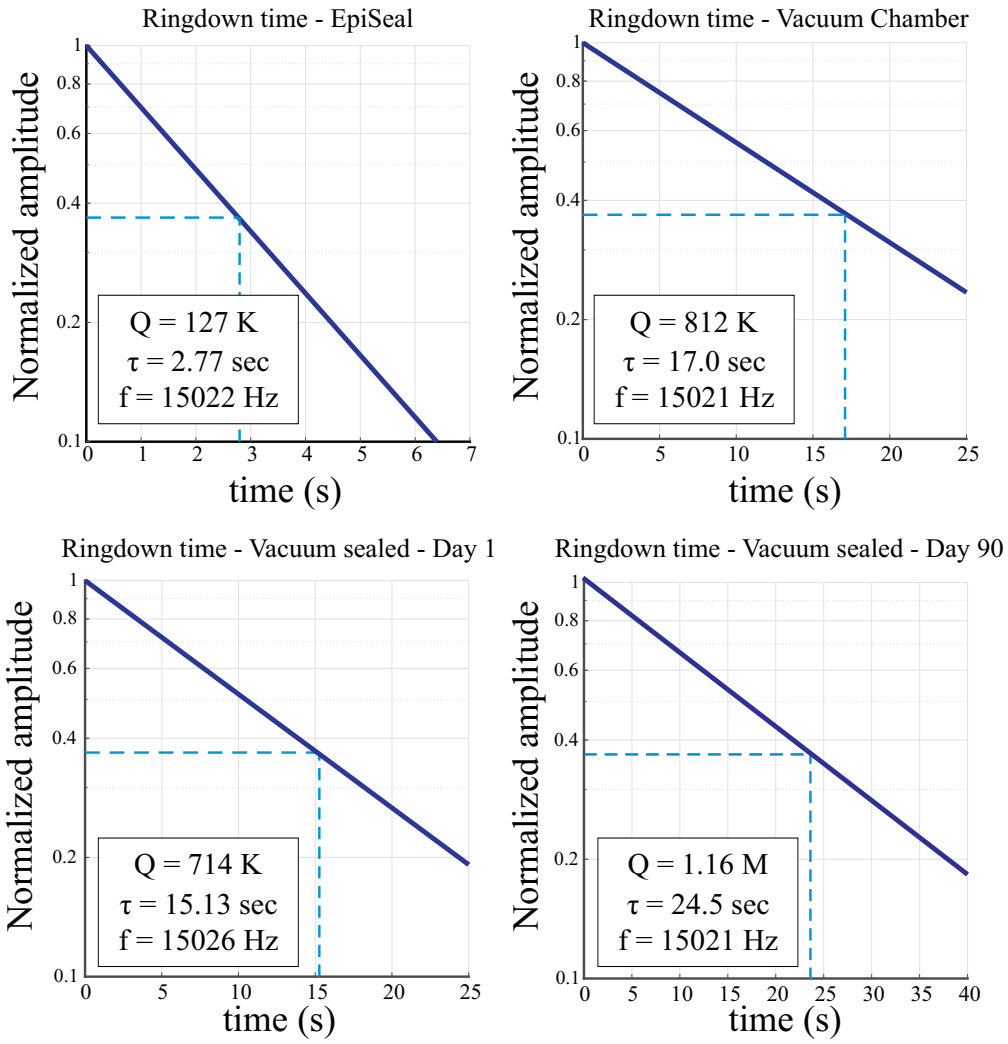

Figure 6.15: Experimental measurement of the amplitude decay time demonstrating 1.15 million Q-factor in a vacuum sealed (with getter) mode-ordered DFP gyro, approaching the theoretical TED limit of the design.

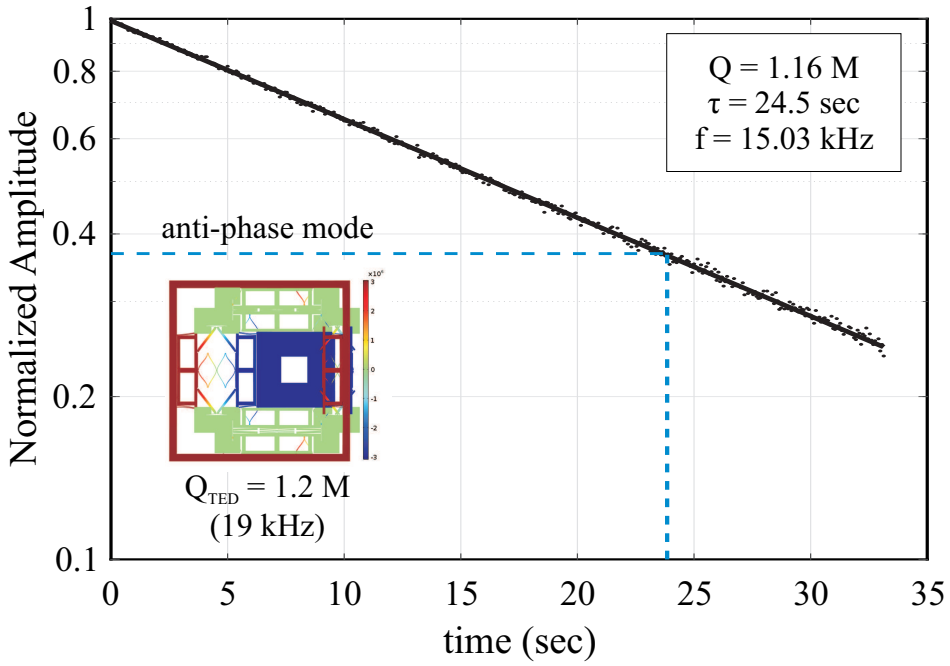

Figure 6.16: Experimental measurement of the amplitude decay time demonstrating 1.15 million Q-factor in a vacuum sealed (with getter) mode-ordered DFP gyro, approaching the theoretical TED limit of the design.

viscous damping and the TED are eliminated, the Q-factor reaches 9.29 million. Moreover, the Q-factor measurements for X- and Y-axis demonstrate the inherited damping symmetry in the DFP device.

Anchor loss

In an ideal DFP gyroscope, the proof masses move in the opposite direction with the same amplitude in the anti-phase mode along each axis, minimizing the reaction forces and moments on anchors. However, fabrication imperfections would disturb symmetry of the structure and increase the dissipation of energy through the substrate. Fig. 6.18 illustrates a schematics of one axis of a non-ideal DFP, where masses (m), stiffness (k), and capacitance (C) of two proof masses are not identical. The capacitance mismatch imposes an unbalanced electrostatic softening, deteriorating the balanced anti-phase motion. Fig. 6.19 demonstrates the effect of the drive DC bias on the amplitude ratio at different mismatch conditions due

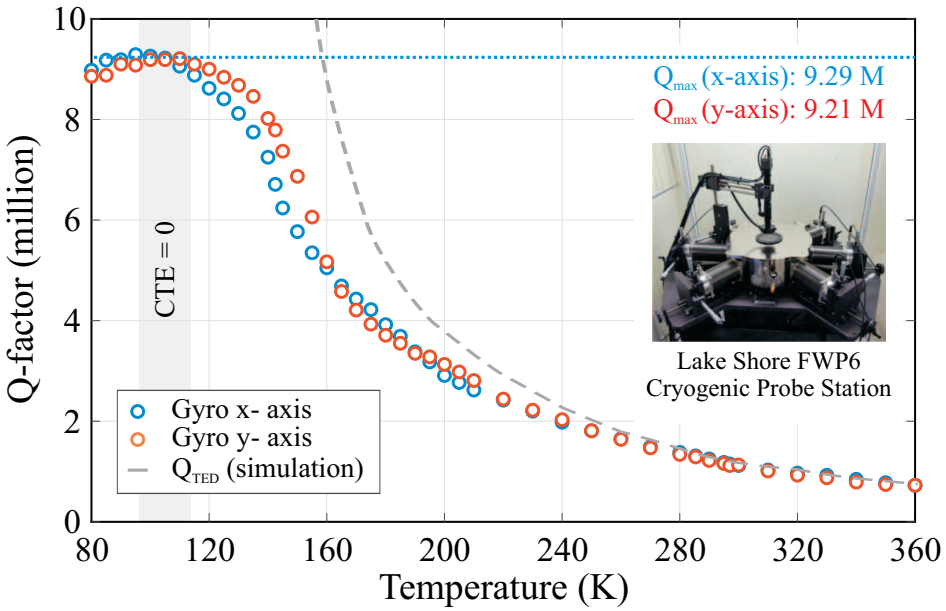

Figure 6.17: Experimental measurement of the Q-factor for DFP gyro as a function of temperature. At the peak of the curve, TED is eliminated, and unmasked anchor loss is observed. Inset figure shows the cryogenic probe station which was used for the measurements.

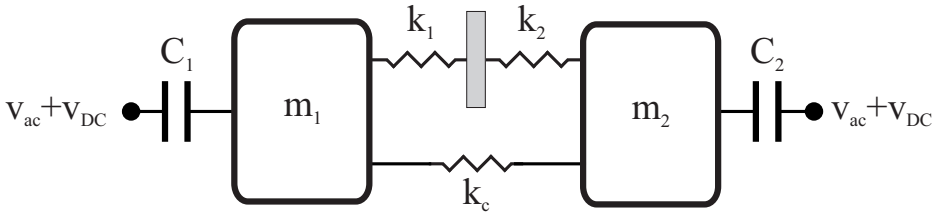

Figure 6.18: Schematics of one axis of a non-ideal DFP showing the unbalanced mass ($m_1 \neq m_2$), stiffness($k_1 \neq k_2$), and capacitance ($C_1 \neq C_2$), all due to fabrication imperfections.

to varying capacitive gaps.

The Q-factor of the DFP device was measured under different drive DC voltages at 110K and 300K. In all cases, the drive amplitude was fixed to avoid the effect of nonlinearities in the drive motion. At 110K, the Q-factor drastically reduced as the voltage increased, whereas it only reduced by 10% at room temperature. The sensitivity of Q-factor to the unbalanced motion proves that at 110K, where the TED and viscous damping are effectively eliminated, the Q-factor of 9.29 million is the anchor loss limit of the DFP device under test.

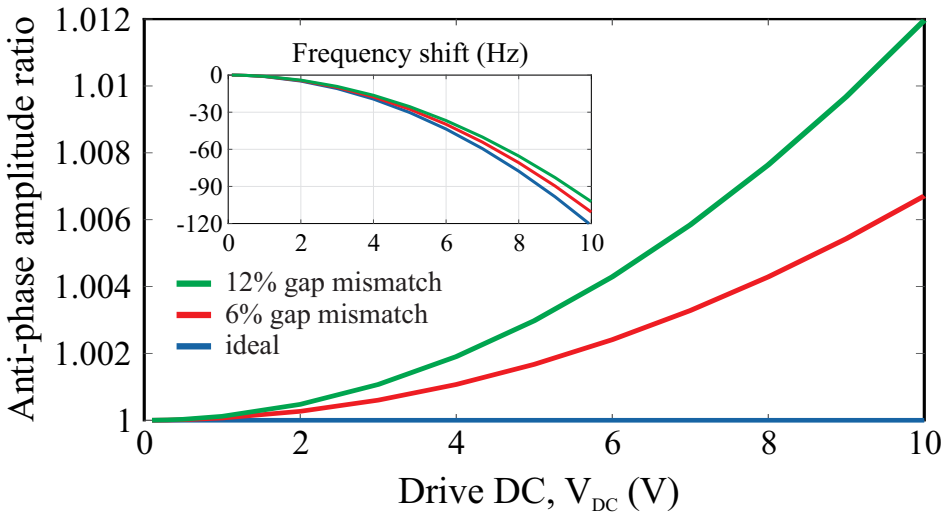

Figure 6.19: Effect of unbalanced electrostatic softening on the anti-phase amplitude ratio at different levels of capacitive gap nonuniformity. The inset figure shows the frequency tuning effect. (simulations were based on extracted parameters from the device under test.)

6.3.4 Noise Performance Characterization

For the rate operation, the as-fabricated frequency mismatch of 112 Hz was electrostatically tuned to less than 0.1 Hz with 6.95 V DC tuning voltage. The Phase-Locked Loop (PLL) and Automatic Gain Control (AGC) Loop were implemented using Zurich Instruments HF2LI Lock-in Amplifier to drive the gyroscope into resonance. The open-loop scale factor of 1.26 mV/deg/sec was extracted by applying an incremental step input rotation (up to 10 deg/sec) using an Ideal Aerosmith rate table. Fig. 6.21 shows the Allan Deviation (ADEV) of the zero rate output (ZRO) bias of the mode-ordered DFP operating in the open-loop rate mode, revealing ARW of 0.075 deg/$\sqrt{hr}$ and in-run bias instability of 1.9 deg /hr without temperature control in the lab environment. The noise performance of the mode-ordered DFP device was characterized under the controlled temperature using a rate table with a thermal chamber. The temperature was set to 28.5 ℃ during the bias and scale factor data recording. Fig. 6.22 demonstrates the ADEV plot of the ZRO in the mode-mismatched and (nearly) mode-matched cases. A bias instability of 0.43 deg/hr was measured on the mode-ordered DFP in a controlled temperature environment.

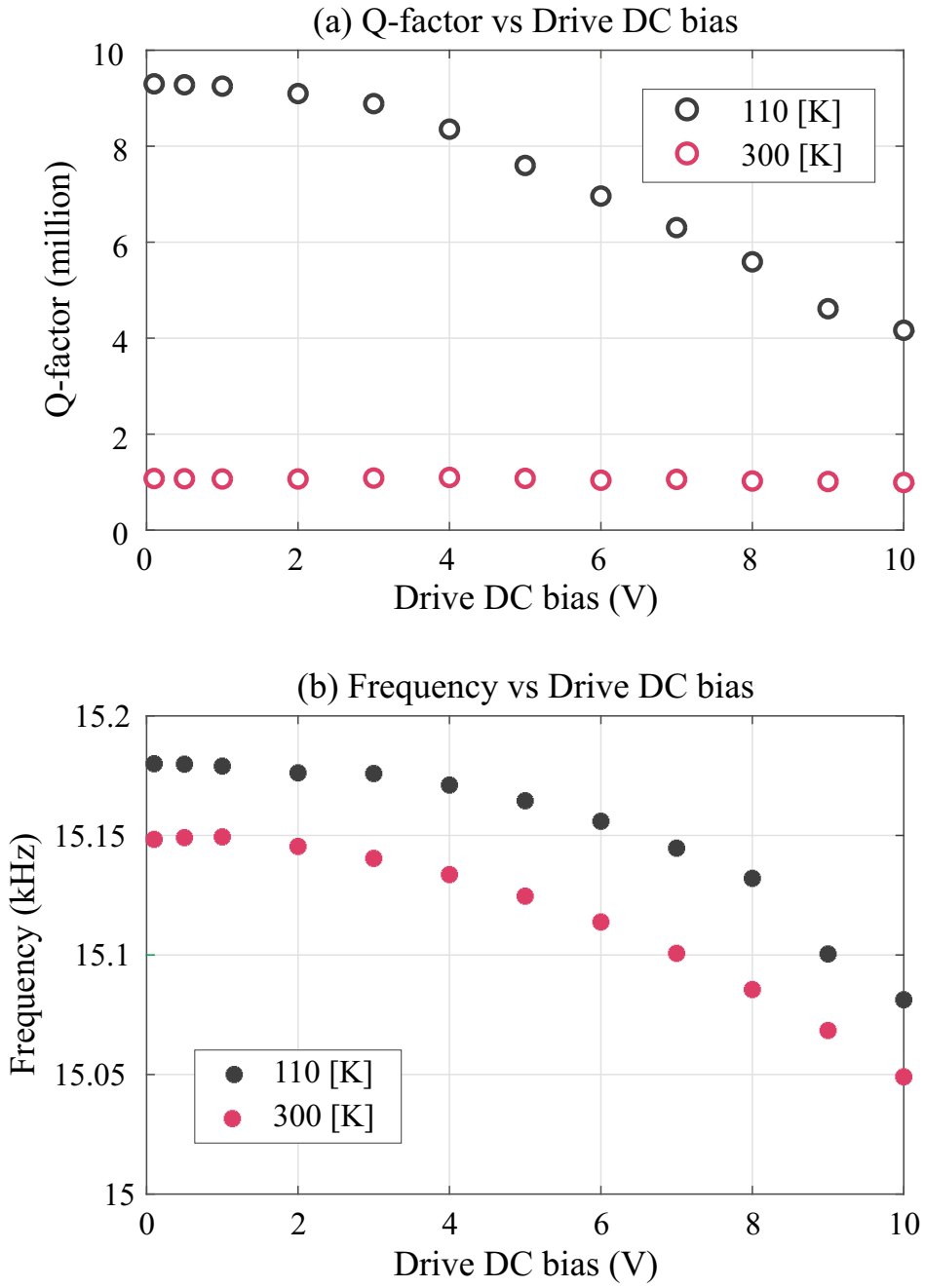

Figure 6.20: Experimental measurement of the Q-factor at 110K and 300K at different drive DC biases. At 110K, the Q-factor is sensitive to the motion unbalance imposed by non-uniform stiffness softening, inset figure shows a similar the frequency tuning effect at 110K and 300K.

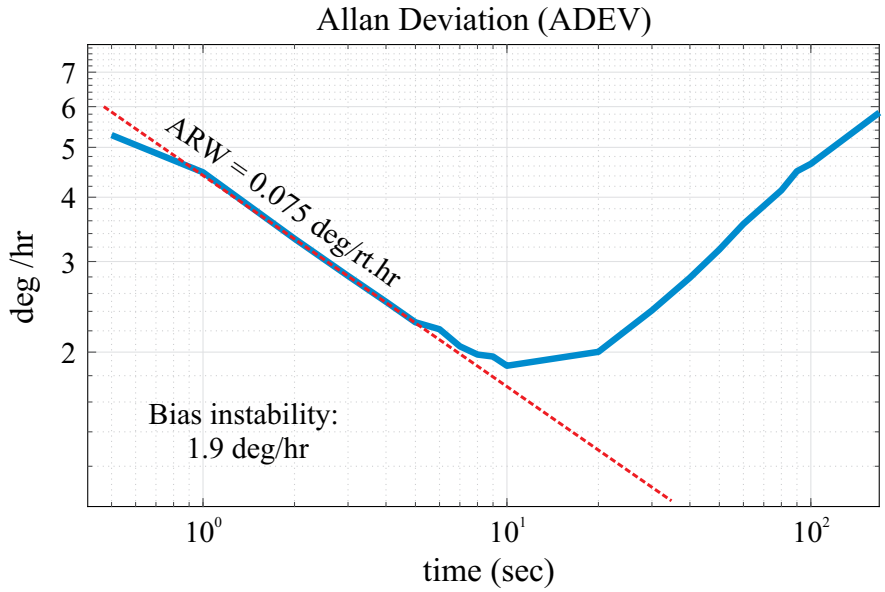

Figure 6.21: ADEV plot of the gyroscope open-loop rate output showing ARW of 0.075 deg/$\sqrt{hr}$ and bias stability of 1.9 deg /hr.

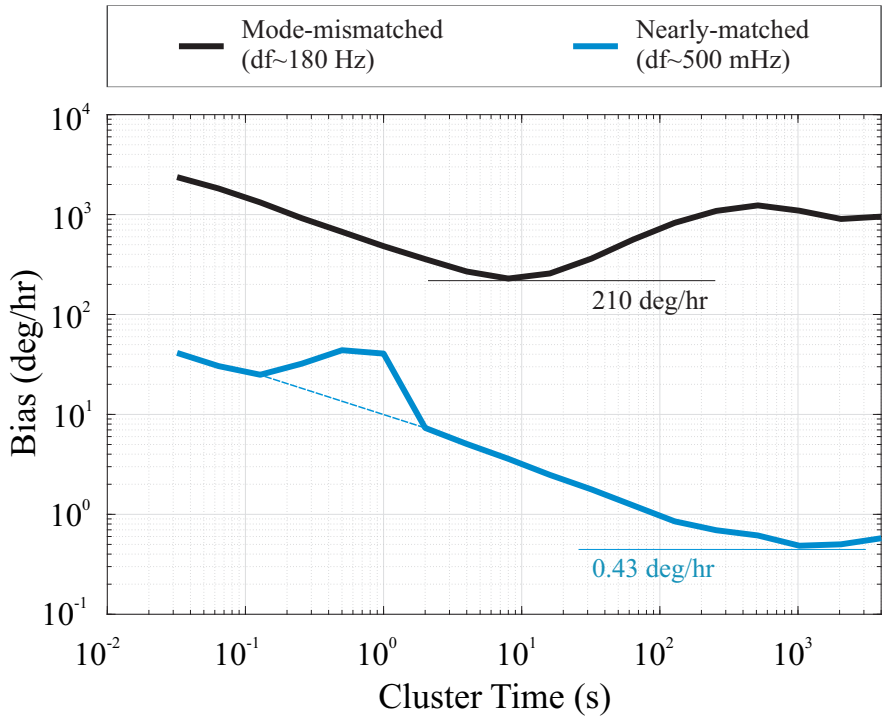

Figure 6.22: ADEV plot of the mode-ordered DFP in the open-loop rate mode with temperature control for mode-mismatched and (nearly) mode-matched cases.

6.4 Conclusion

In this chapter, the energy dissipation sources in silicon MEMS gyroscopes were studied. Effective elimination of viscous damping was successfully achieved by developing a package-level vacuum sealing process with getter activation for high-performance MEMS inertial sensors. The process parameters were adjusted to maximize de-sorption of gas molecules prior to the encapsulation, to activate getter efficiently, and to obtain a defect-free sealing, which resulted in high process yield on devices under test. The integrated getter was activated and continuously pumped the residual and desorbed gases, improving the Q-factor over a period of one year. For the first time, the improvement in the vacuum-level of sealed MEMS gyroscopes was reported. The experimental results reported in this work confirmed the reliability and repeatability of the proposed vacuum sealing procedure. The result suggests the suitable process parameters and requirements that can be adapted either for wafer-level high-vacuum packaging and other types of MEMS sensors with ultra-high vacuum requirements.

Novel suspension designs were implemented on Dual Foucault Pendulum (DFP) gyroscopes. The suspension was designed to order the anti-phase and in-phase resonant modes of DFP gyro such that the anti-phase becomes the first resonant mode and in-phase shifts to a higher frequency. The mode-ordered DFP gyroscopes at a center frequency of $\sim$ 15 kHz were designed and fabricated using epitaxial silicon encapsulation process with a footprint of 2 mm $\times$ 2 mm. Q-factors higher than 1 million were demonstrated after venting and vacuum sealing of the sensors with getter activation. The high Q-factor is associated with a dynamically balanced operation of the device in the anti-phase motion. The implemented new suspension, and coupling design provided $\sim$ 12kHz frequency separation between the desired and spurious frequency modes, ordered the anti-phase mode as the first vibration mode of the device. The open-loop rate gyro characterization results revealed ARW of 0.075 deg/$\sqrt{hr}$ and in-run bias stability of 1.9 deg /hr. The high Q-factor and mode-ordered DFP

operating in the degenerate mode can be possibly utilized for a reliable rate measurement in harsh environments.

Finally, the energy dissipation mechanisms in a high-Q mode-ordered DFP gyroscope were analyzed. At room temperature, a close match between the measured Q-factor and simulated thermoelastic damping limit was achieved after vacuum sealing with getter activation. The peak Q-factor value of 9.29 million was measured in a Cryogenic setup at $\sim$ 110 Kelvin revealed an exceptional anchor loss limit, which is attributed to a fully dynamically balanced architecture of DFP. The experimentally measured Q-factor on the mode-ordered DFP is, to best of our knowledge, the highest Q-factor reported on silicon MEMS gyroscopes. The unbalanced electrostatic softening was identified as the contributing factor to the anchor loss. The sensitivity of the Q-factor to stiffness unbalance was analyzed to identify the primary energy dissipation mechanisms at different temperatures.

Chapter 7

Conclusions

This dissertation reports results on development of 3D structures for MEMS Coriolis Vibratory Gyroscopes. The primary focus of this thesis is on the design optimization, modeling, and process development for fabrication, integration, and gyro operation of 3D fused quartz micro-shell gyroscopes, which can lead to development of a low-cost fabrication techniques for miniaturization of Hemispherical Resonator Gyroscopes. A practical implementation of high-Q dual-shell resonator is developed as a potential technology that may improve tolerance to high shock in micro-shell devices and enable continuous gyro operation in adverse environments. The energy dissipation mechanisms in 2D silicon and 3D fused quartz MEMS gyroscopes are studied. A reliable and repeatable ultra-high-vacuum sealing was developed to eliminate viscous damping. A novel suspension element was implemented on Dual Foucault Pendulum to mitigate the anchor losses and the energy dissipation through mode mixing. The specific contributions of this work are summarized below.

7.1 Contributions

- Fabrication processes were developed that enabled the realization of 3D fused quartz micro-shell resonators with a broad range of operational frequencies. The limitations of the existing baseline micro-glassblowing process in fabrication of low-frequency shell resonators were addressed by developing the "vacuum" and the "reverse" glassblowing processes. The introduced processes enabled fabrication of micro-shell resonators with the n=2 wineglass frequency on the order of 5 kHz, which was previously limited to $\sim$ 100 kHz with the baseline process. The Q-factor as high as 1.7 million was demonstrated on the n=2 wineglass mode of a shell resonator at 22 kHz. The highest measured Q-factor was demonstrated at 3.2 million on the n=4 mode of a shell resonator at 254 kHz.

- Design space exploration for optimization of geometric parameters of 3D micro-shell geometry parameters through extensive finite element simulations, the dissipation of energy through mode-mixing and TED were identified as the main challenges in the design of low-frequency hemi-toroidal resonators. The scaling of frequencies of the operational and non-operational modes with the shell geometry and a possibility of mode-ordering in shell resonators were demonstrated numerically and experimentally.

- Micro-glassblowing processes were modeled to predict the final 3D shell geometry. A fluid flow model was developed to simulate the micro-glassblowing processes. The model captures the self-limiting nature of the process by calculating the volume of the glassblown shells and re-adjusting the pressure. A post-processing technique based on results of the fluid flow simulation was presented for performing the analysis of the modal and transient dynamics. The presented hybrid fluid-structural method could reduce the cost and time in the development of 3D shell resonators through numerical design iterations, instead of experimental trial-and-error approach. The developed

model was also employed in the design and simulation of micro-cells for atomic sensors, which is outside the scope of this thesis.

- A vacuum-compatible assembly process was developed for integration of micro-shell resonators with planar electrodes. The out-gassing, electrical and mechanical properties, etch selectivity, and temperature compatibility of the materials were considered in the process development. An assembled micro-shell resonator with uniform capacitive gaps $<5\mu$m was demonstrated for the electrostatic operation. The gap reduction is a technological step leading to drastic improvements in sensitivity of shell-type devices. For the first time, a glass-blown micro-shell resonator was implemented as a rate gyroscope.

- A novel fused quartz "dual-shell" resonator was designed for high shock applications. A full-cycle development of the dual-shell technology was presented in this thesis, including design optimization, modeling, process development, fabrication, integration with electrodes, vacuum encapsulation, capacitive actuation and detection, electrostatic frequency tuning, and open-loop gyro operation. Q-factors of over 1 million on dual-shell resonators at the center frequency of 5-7 kHz were demonstrated on dual-shell resonators. A ring-down time higher than 120 seconds and the Q-factor of above 3.75 million were demonstrated experimentally, which is the highest measured ring-down time and Q-factor on glass-blown micro-shell resonators, to date.

- An ultra-high and ultra-stable die-level vacuum sealing process was developed for 2D and 3D MEMS inertial sensors. The process was optimized for effective desorption of gas molecules on the surface of devices before encapsulation, efficient activation of getter material for long-time vacuum stability, and defect-free solder reflow. The developed process has been successfully employed in vacuum sealing of high-Q silicon MEMS devices, demonstrating greater than 90% process yield. Q-factors of over 1 million were repeatedly obtained on multiple quad mass gyroscopes and mode-ordered

Dual Foucault Pendulum sensor with proven vacuum stability over the last three years.

- A mode-ordering suspension element was designed and implemented on Dual Foucault Pendulum silicon MEMS gyro. The device was fabricated in the Epitaxially Encapsulated Silicon-on-Insulator process at Stanford University. After post-processing and vacuum sealing with getter, the Q-factor of 1.15 million was demonstrated on an anti-phase resonant mode of the mode-ordered DFP at the center frequency of 15 kHz. The characterization of energy dissipation at low temperature revealed an outstanding Q-factor of 9.29 million which, to the best of our knowledge, is the highest Q-factor measured on silicon MEMS gyroscopes.

7.2 Future Research Directions

7.2.1 Patterned Micro-Shell Resonators

Micro-shell resonators with complex geometries can be fabricated by pre-patterning of the device layer before the glassblowing process. The FE model of the glassblowing in Chapter 3 was demonstrated the capability to predict the final shell geometry. The simulation results also showed that patterning the device layer would change the final geometry that can be used to design shell resonators with low n=2 wineglass mode and more significant modal separation. A 3D model can be developed to incorporate non-axisymmetric features on the device layer, which can potentially decouple mass and stiffness, or define the principal axes of elasticity in the glass-blown resonators.

7.2.2 Balancing of Micro-Shell Resonators

Imperfections are always present in micro-fabricated shell devices. The major sources of the fabrication imperfection in the glass-blown micro-shells are non-uniform temperature

distribution in the fused quartz die during the glassblowing, the non-uniform initial thickness of the fused quartz die due to thickness variation in the wafers and non-uniform wet etching. The developed assembly process for the micro-glassblown shell and dual-shell resonators demonstrated the ability to electrostatically tune the frequency mismatches between the n=2 wineglass modes due to fabrication imperfection. The planar electrodes were implemented to reduce the complexity of the assembly process. However, in very thin shell resonators, the capacitance at the rim of the shell is limited. Thus, much smaller gaps are required to compensate for the limited area. The permanent tuning of shell and dual-shell resonators using femtosecond laser ablation/irradiation or chemical etching can be employed to reduce the as-fabricated asymmetry before integration with the electrode substrates. A model must be developed to identify the mass unbalance in the shell resonators. The frequency mismatch can be characterized at different wineglass modes, i.e., n=2, n=3, and higher-order wineglass modes, and can be used to build a model for the mass unbalance.

7.2.3 Analysis of Energy Dissipation Mechanisms

The Q-factor measurement on the glass-blown shell and dual-shell resonators revealed that different wineglass modes have different Q-factors. The dissipation of energy at different orders of wineglass modes can be analyzed to determine the dissipation mechanism that limits the Q-factor. This will be a fundamental research that would study the primary energy dissipation mechanism at different wineglass modes. A potential research question is "what is the dependency of surface losses, anchor losses, and TED on the order of wineglass mode?" As demonstrated in silicon MEMS devices, the Q-factor measurement in a Cryogenic setup, at the temperature when CTE of fused silica is zero, can be performed to eliminate the TED, and observe other energy dissipation mechanisms, which are higher than TED.

7.2.4 High Shock Resilient Resonators and Gyroscopes

Numerical simulations predicted that dual-shell resonators could potentially be implemented in the rate measurement applications wth high-g external shocks. The presented FE framework enabled prediction of the sensor's integrity when an external shock is applied. Optimization of the dual-shell geometry parameters may lead to a design with unprecedented shock resilience and may enable continuous gyro operation during the shock event. This anticipated capability would need to be addressed in the future research.

7.2.5 Piezo Actuation of Micro-Shell Gyroscope

The dual-shell resonators demonstrated as part of this thesis. The outer shell in the dual-shell resonators can be used to potentially deposit and pattern thin-film piezoelectric material to actuate the wineglass mode of the inner shell instead of capacitive actuation. A conformal multi-channel fiber optic vibrometry technique can be employed to detect the amplitude of vibration. Piezo actuation and detection using vibrometry eliminate the requirement for coating the vibrating shell and would lead to higher mechanical quality factor.

7.2.6 Dual-Shell Stacked 3D Micro-Shell Resonators

In the dual-shell resonator presented as a part of this thesis, the outer shell was utilized to anchor the inner shell (sensing element). In another configuration, the outer shell can be released to fabricate dual-shell stacked resonator. In this way, two shell resonators with a single central stem are fabricated. The design parameters can be selected such that the shells have similar or different resonant frequencies. The dual-shell stacked resonators with small form factor have potential advantages when self-calibration run-time techniques can be performed on one shell while the other is instrumented to operate in the gyro mode. Thus, the calibration and gyro operation can be performed without interruption.

Bibliography

[1] D. Senkal, M.J. Ahamed, M.H. Asadian, S. Askari, and A.M. Shkel. Demonstration of 1 million Q-factor on microglassblown wineglass resonators with out-of-plane electrostatic transduction. *IEEE Journal of Microelectromechanical Systems (JMEMS)*, 24(1):29–37, 2015.

[2] M.H. Asadian, Y. Wang, S. Askari, and A.M. Shkel. Controlled capacitive gaps for electrostatic actuation and tuning of 3d fused quartz micro wineglass resonator gyroscope. *IEEE International Symposium on Inertial Sensors and Systems (INERTIAL)*, Kauai, HI, USA, March, 2017.

[3] D.M. Rozelle. The hemispherical resonator gyro: From wineglass to the planets. *the Proceedings of 19th AAS/AIAA Space Flight Mechanics Meeting*, Savannah, Georgia, Feb. 8-12, 2009.

[4] D. Senkal. *Micro-glassblowing Paradigm for Realization of Rate Integrating Gyroscopes*. PhD thesis, University of California, Irvine, CA, USA, 2015.

[5] A.M. Shkel. Type I and type II micromachined vibratory gyroscopes. *IEEE/ION Position, Location, And Navigation Symposium (PLANS)*, pages 586–593, April 25-27, 2006, San Diego, CA.

[6] C. Acar and A.M. Shkel. *MEMS vibratory gyroscopes: structural approaches to improve robustness*. Springer Science & Business Media, 2008.

[7] D.D. Lynch. Vibratory gyro analysis by the method of averaging. *The 2nd St. Petersburg International Conference on Gyroscopic Technology and Navigation*, Saint Petersburg, Russia, May 24-25, 1995.

[8] R.P. Leland. Mechanical-thermal noise in MEMS gyroscopes. *IEEE Sensors Journal*, 5(3):493–500, 2005.

[9] V. Kaajakari. Practical MEMS: Design of microsystems, accelerometers, gyroscopes, RF MEMS, optical MEMS, and microfluidic systems. *Las Vegas, NV: Small Gear Publishing*, 2009.

[10] M.F. Zaman, A. Sharma, and F. Ayazi. High performance matched-mode tuning fork gyroscope. *IEEE International Conference on Micro Electro Mechanical Systems (MEMS)*, Istanbul, Turkey, Jan. 22-26, 2006.

[11] D. Vatanparvar and A.M. Shkel. Effect of fabrication imperfections on energy loss through mechanical mode coupling in MEMS. *IEEE International Symposium on Inertial Sensors and Systems (INERTIAL), Lake Como, Italy*, March 26-29, 2018.

[12] C. Zener. Internal friction in solids II. General theory of thermoelastic internal friction. *Physical Review*, 53(1):90, 1938.

[13] R. Lifshitz and M.L. Roukes. Thermoelastic damping in micro-and nanomechanical systems. *Physical review B*, 61(8):5600, 2000.

[14] B. Kühn and R. Schadrack. Thermal expansion of synthetic fused silica as a function of OH content and fictive temperature. *Journal of Non-Crystalline Solids*, 355(4-5):323–326, 2009.

[15] T. Middelmann, A. Walkov, G. Bartl, and René Schödel. Thermal expansion coefficient of single-crystal silicon from 7 k to 293 k. *Physical Review B*, 92(17):174113, 2015.

[16] A. Darvishian, T. Nagourney, J.Y. Cho, B. Shiari, and K. Najafi. Thermoelastic dissipation in micromachined birdbath shell resonators. *IEEE Journal of Microelectromechanical Systems (JMEMS)*, 26(4):758–772, 2017.

[17] H. Niino, Y. Kawaguchi, T. Sato, A. Narazaki, T. Gumpenberger, and R. Kurosaki. Laser ablation of toluene liquid for surface micro-structuring of silica glass. *Applied Surface Science*, 252(13):4387–4391, 2006.

[18] E. Belloy, A. Sayah, and M.A.M. Gijs. Powder blasting for three-dimensional microstructuring of glass. *Sensors and Actuators A: Physical*, 86(3):231–237, 2000.

[19] X. Li, T. Abe, Y. Liu, and M. Esashi. Fabrication of high-density electrical feedthroughs by deep-reactive-ion etching of pyrex glass. *IEEE Journal of Microelectromechanical Systems (JMEMS)*, 11(6):625–630, 2002.

[20] Y. Bellouard, A. Said, M. Dugan, and P. Bado. Fabrication of high-aspect ratio, micro-fluidic channels and tunnels using femtosecond laser pulses and chemical etching. *Optics Express*, 12(10):2120–2129, 2004.

[21] P. Shao, V. Tavassoli, C.-S. Liu, L.D. Sorenson, and F. Ayazi. Electrical characterization of ald-coated silicon dioxide micro-hemispherical shell resonators. *IEEE International Conference on Micro Electro Mechanical Systems (MEMS)*, San Francisco, CA, USA, Jan. 26-30, 2014.

[22] LD Sorenson, X Gao, and F Ayazi. 3-d micromachined hemispherical shell resonators with integrated capacitive transducers. *IEEE International Conference on Micro Electro Mechanical Systems (MEMS)*, Paris, France, Jan. 29 - Feb 2, 2012.

[23] L. D. Sorenson, X. Gao, and F. Ayazi. 3-D micromachined hemispherical shell resonators with integrated capacitive transducers. *IEEE International Conference on Micro Electro Mechanical Systems (MEMS)*, Paris, France, 29 Jan.- 2 Feb. 2012.

[24] F. Ayazi and K. Najafi. A harpss polysilicon vibrating ring gyroscope. *IEEE Journal of Microelectromechanical Systems (JMEMS)*, 10(2):169–179, 2001.

[25] P. Shao, V. Tavassoli, C.L. Mayberry, and F. Ayazi. A 3d-harpss polysilicon micro-hemispherical shell resonating gyroscope: Design, fabrication, and characterization. *IEEE Sensors Journal*, 15(9):4974–4985, 2015.

[26] P. Pai, F.K. Chowdhury, C.H. Mastrangelo, and M. Tabib-Azar. Mems-based hemispherical resonator gyroscopes. *Sensors, 2012 IEEE*, pages 1–4, 2012.

[27] Y. Xie, H.-C. Hsieh, P. Pai, H. Kim, M. Tabib-Azar, and C.H. Mastrangelo. Precision curved micro hemispherical resonator shells fabricated by poached-egg micro-molding. *IEEE Sensors Conference (SENSORS)*, Taipei, Taiwan, October 28-31, 2012.

[28] M.M. Rahman, Y. Xie, C. Mastrangelo, and H. Kim. 3-D hemispherical micro glass-shell resonator with integrated electrostatic excitation and capacitive detection transducers. *IEEE International Conference on Micro Electro Mechanical Systems (MEMS)*, San Francisco, CA, USA, Jan. 26-30, 2014.

[29] R. Perahia, J. Lake, S. Iyer, D. Kirby, H. Nguyen, T. Boden, R. Joyce, L. Huang, L. Sorenson, and D. Chang. Electric gradient force drive mechanism for novel microscale all-dielectric gyroscope. *IEEE International Conference on Micro Electro Mechanical Systems (MEMS)*, San Francisco, CA, USA, Jan. 26-30, 2014.

[30] R. Perahia, H.D. Nguyen, L.X. Huang, T.J. Boden, J.J. Lake, D.J. Kirby, R.J. Joyce, and L. Sorenson. Novel touch-free drive, sense, and tuning mechanism for all dielectric micro-shell gyroscope. *Solid-State Sensors, Actuators, and Microsystems Workshop*, Hilton Head Island, SC, USA, June 8-12, 2014.

[31] P. Ovartchaiyapong, L.M.A. Pascal, B.A. Myers, P. Lauria, and A.C. Jayich. High quality factor single-crystal diamond mechanical resonators. *Applied Physics Letters*, 101(16):163505, 2012.

[32] M.L. Chan, J. Xie, P. Fonda, H. Najar, K. Yamazaki, L. Lin, and D.A. Horsley. Micromachined polycrystalline diamond hemispherical shell resonators. *Solid-State Sensors, Actuators, and Microsystems Workshop, Hilton Head Island, SC, USA*, June 3-7, 2012.

[33] A. Heidari, M.-L. Chan, H.-A. Yang, G. Jaramillo, P. Taheri-Tehrani, P. Fonda, H. Najar, K. Yamazaki, L. Lin, and D.A. Horsley. Hemispherical wineglass resonators fabricated from the microcrystalline diamond. *Journal of Micromechanics and Microengineering*, 23(12):p.125016, 2013.

[34] P. Taheri-Tehrani, T. Su, A. Heidari, G. Jaramillo, C. Yang, S. Akhbari, H. Najar, S. Nitzan, D. Saito, and L. Lin. Microscale diamond hemispherical resonator gyroscope. *Solid-State Sensors, Actuators, and Microsystems Workshop, Hilton Head Island, SC, USA*, June 8-12, 2014.

[35] D. Saito, C. Yang, A. Heidari, H. Najar, L. Lin, and D.A. Horsley. Batch-fabricated high q-factor microcrystalline diamond cylindrical resonator. *IEEE International Conference on Micro Electro Mechanical Systems (MEMS)*, Estoril, Portugal, Jan. 18-22, 2015.

[36] D. Saito, C. Yang, A. Heidari, H. Najar, L. Lin, and D.A. Horsley. Microcrystalline diamond cylindrical resonators with quality-factor up to 0.5 million. *Applied Physics Letters*, 108(5):051904, 2016.

[37] J.J. Bernstein, M.G. Bancu, E.H. Cook, M.V. Chaparala, W.A. Teynor, and M.S. Weinberg. A MEMS diamond hemispherical resonator. *Journal of Micromechanics and Microengineering*, 23(12):p.125007, 2013.

[38] J.J. Bernstein, M. Bancu, E. Cook, T. Henry, P. Kwok, T. Nyinjee, G. Perlin, B. Teynor, and M. Weinberg. Diamond hemispherical resonator fabrication by isotropic glass etch. *Solid-State Sensors, Actuators, and Microsystems Workshop, Hilton Head Island, SC, USA*, June 8-12, 2014.

[39] B.R. Johnson, C. Boynton, E. Cabuz, S. Chang, K. Christ, S. Moore, J. Reinke, and K. Winegar. Toroidal resonators with small frequency mismatch for rate integrating gyroscopes. *IEEE International Symposium on Inertial Sensors and Systems (INERTIAL)*, Laguna Beach, CA, Feb. 25-26, 2014.

[40] N. Mehanathan, V. Tavassoli, P. Shao, L.D. Sorenson, and F. Ayazi. Invar-36 micro hemispherical shell resonators. *IEEE International Conference on Micro Electro Mechanical Systems (MEMS)*, pages 40–43, San Francisco, CA, USA, Jan. 26-30, 2014.

[41] P. Mohn. Materials science: A century of zero expansion. *Nature*, 400(6739):18, 1999.

[42] X. Zhuang, X. Wang, L. Yu, P. Li, B. Chen, Q. Guo, and S. Guo. Micromachined silicon hemispherical resonators with self-aligned spherical capacitive electrodes. *SENSORS, 2015 IEEE*, pages 1–4, 2015.

[43] M.M. Torunbalci, S. Dai, A. Bhat, and S. Bhave. Acceleration insensitive hemispherical shell resonators using pop-up rings. *IEEE International Conference on Micro Electro Mechanical Systems (MEMS)*, Belfast, Northern Ireland, UK, Jan., 21-25, 2018.

[44] E.J. Eklund and A.M. Shkel. Glass blowing on a wafer level. *IEEE Journal of Microelectromechanical Systems (JMEMS)*, 16(2):232–239, 2007.

[45] E.J. Eklund, A.M. Shkel, S. Knappe, E. Donley, and J. Kitching. Glass-blown spherical microcells for chip-scale atomic devices. *Sensors and Actuators A: Physical*, 143(1):175–180, 2008.

[46] R.M. Noor, N. Kulachenkov, M.H. Asadian, and A.M. Shkel. Study on MEMS Glass-blown Cells for NMR Sensors. *IEEE International Symposium on Inertial Sensors and Systems (INERTIAL)*, Naples, FL, April 1-5, 2019.

[47] S.A. Zotov, I.P. Prikhodko, A.A. Trusov, and A.M. Shkel. 3-d micromachined spherical shell resonators with integrated electromagnetic and electrostatic transducers. *Solid-State Sensors, Actuators, and Microsystems Workshop, Hilton Head Island, SC, USA*, June 6-10, 2010.

[48] I.P. Prikhodko, S.A. Zotov, A.A. Trusov, and A.M. Shkel. Microscale glass-blown three-dimensional spherical shell resonators. *IEEE Journal of Microelectromechanical Systems (JMEMS)*, 20(3):691–701, 2011.

[49] D Senkal, IP Prikhodko, AA Trusov, and AM Shkel. Micromachined 3-D glass-blown wineglass structures for vibratory MEMS applications. *Technologies or Future Micro-Nano Manufacturing*, August 2011.

[50] D. Senkal, M.J. Ahamed, A.A. Trusov, and A.M. Shkel. Electrostatic and mechanical characterization of 3-D micro-wineglass resonators. *Sensors and Actuators A: Physical*, 215:150–154, 2014.

[51] D. Senkal, M.J. Ahamed, A.A. Trusov, and A.M. Shkel. Adaptable test-bed for characterization of micro-wineglass resonators. *IEEE International Conference on Micro Electro Mechanical Systems (MEMS)*, Taipei, Taiwan, Jan. 20-24, 2013.

[52] D. Senkal, M.J. Ahamed, A.A. Trusov, and A.M. Shkel. Achieving sub-hz frequency symmetry in micro-glassblown wineglass resonators. *IEEE Journal of Microelectromechanical Systems (JMEMS)*, 23(1):30–38, 2014.

[53] J. Giner, J.M. Gray, J. Gertsch, V.M. Bright, and A.M. Shkel. Design, fabrication, and characterization of a micromachined glass-blown spherical resonator with insitu integrated silicon electrodes and ald tungsten interior coating. *IEEE International Conference on Micro Electro Mechanical Systems (MEMS)*, Estoril, Portugal, Jan. 18-22, 2015.

[54] D. Senkal, C.R. Raum, A.A. Trusov, and A.M. Shkel. Titania silicate/fused quartz glassblowing for 3-D fabrication of low internal loss wineglass micro-structures. *Solid-State Sensors, Actuators, and Microsystems Workshop, Hilton Head Island, SC, USA*, June 3-7, 2012.

[55] D. Senkal, M.J. Ahamed, A.A. Trusov, and A.M. Shkel. High temperature micro-glassblowing process demonstrated on fused quartz and ULE TSG. *Sensors and Actuators A: Physical*, 201:525–531, 2013.

[56] D. Senkal, M.J. Ahamed, and A.M. Shkel. Design and modeling of micro-glassblown inverted-wineglass structures. *IEEE International Symposium on Inertial Sensors and Systems (INERTIAL)*, Laguna Beach, CA, Feb. 25-26, 2014.

[57] D. Senkal, M.J. Ahamed, M.H. Asadian, S. Askari, and A.M. Shkel. Out-of-plane electrode architecture for fused silica micro-glassblown 3-D wineglass resonators. *IEEE Sensors Conference (SENSORS)*, Valencia, Spain, November 2-5, 2014.

[58] Y. Wang, M.H. Asadian, and A.M. Shkel. Modeling the effect of imperfections in glass-blown micro-wineglass fused quartz resonators. *Journal of Vibration and Acoustics*, 139(4):040909, 2017.

[59] Y. Wang, M.H. Asadian, and A.M. Shkel. Compensation of frequency split by directional lapping in fused quartz micro wineglass resonators. *Journal of Micromechanics and Microengineering*, 28(9):p.095001, 2018.

[60] Y. Wang and A.M. Shkel. Study on surface roughness improvement of fused quartz after thermal and chemical post-processing. *IEEE International Symposium on Inertial Sensors and Systems (INERTIAL)*, Laguna Beach, CA, Feb. 22-25, 2016.

[61] J. Cho, J. Yan, J.A. Gregory, H. Eberhart, R.L. Peterson, and K. Najafi. High-q fused silica birdbath and hemispherical 3-D resonators made by blow torch molding. *IEEE International Conference on Micro Electro Mechanical Systems (MEMS)*, Taipei, Taiwan, Jan. 20-24, 2013.

[62] T. Nagourney, J.Y. Cho, A. Darvishian, B. Shiari, and K. Najafi. Micromachined high-Q fused silica bell resonator with complex profile curvature realized using 3D micro blowtorch molding. *International Conference on Solid-State Sensors, Actuators and Microsystems (TRANSDUCERS)*, Anchorage, Alaska, USA, June 21-25, 2015.

[63] S. Singh, A. Darvishian, J.Y. Cho, B. Shiari, and K. Najafi. Resonant characteristics of birdbath shell resonator in n= 3 wine-glass mode. *IEEE Sensors Conference (SENSORS)*, New Delhi, India, October 28-31, 2018.

[64] S. Singh, T. Nagourney, J.Y. Cho, A. Darvishian, K. Najafi, and B. Shiari. Design and fabrication of high-q birdbath resonator for MEMS gyroscopes. *IEEE/ION Position, Location and Navigation Symposium (PLANS)*, Monterey, CA, USA, April 23-26, 2018.

[65] C. Boyd, J.K. Woo, J.Y. Cho, T. Nagourney, A. Darvishian, B. Shiari, and K. Najafi. Effect of drive-axis displacement on MEMS birdbath resonator gyroscope performance. *IEEE International Symposium on Inertial Sensors and Systems (INERTIAL)*, Kauai, HI, USA, March 27-30, 2017.

[66] J.Y. Cho, J.K. Woo, G. He, D. Yang, C. Boyd, S. Singh, A. Darvishian, B. Shiari, and K. Najafi. 1.5-Million q-factor vacuum-packaged birdbath resonator gyroscope (BRG). *IEEE International Conference on Micro Electro Mechanical Systems (MEMS)*, Seoul, South Korea, Jan. 27-31, 2019.

[67] W. Li, X. Xi, K. Lu, Y. Shi, Z. Hou, Y. Wu, X. Wu, and D. Xiao. A novel high transduction efficiency micro shell resonator gyroscope with 16 t-shape masses using out-of-plane electrodes. *IEEE Sensors Journal*, 19(13):4820–4828, 2019.

[68] M. Kanik, P. Bordeenithikasem, J. Schroers, N. Selden, A. Desai, D. Kim, and R. M'Closkey. Microscale three-dimensional hemispherical shell resonators fabricated from metallic glass. *IEEE International Symposium on Inertial Sensors and Systems (INERTIAL)*, Laguna Beach, CA, Feb. 25-26, 2014.

[69] M. Kanik, P. Bordeenithikasem, D. Kim, N. Selden, A. Desai, R. MCloskey, and J. Schroers. Metallic glass hemispherical shell resonators. *IEEE Journal of Microelectromechanical Systems (JMEMS)*, 24(1):19–28, 2015.

[70] J. Schroers. Processing of bulk metallic glass. *Advanced Materials*, 22(14):1566–1597, 2010.

[71] B. Sarac, G. Kumar, T. Hodges, S. Ding, A. Desai, and J. Schroers. Three-dimensional shell fabrication using blow molding of bulk metallic glass. *IEEE Journal of Microelectromechanical Systems (JMEMS)*, 20(1):28–36, 2011.

[72] S.Y. Choi, Y.H. Na, and J.H. Kim. Thermoelastic damping of inextensional hemispherical shell. *World Academy of Science, Engineering and Technology*, 56(32):198–203, 2009.

[73] B.R. Simon, S. Khan, A.A. Trusov, and A.M. Shkel. Mode ordering in tuning fork structures with negative structural coupling for mitigation of common-mode g-sensitivity. *IEEE Sensors Conference (SENSORS)*, Busan, South Korea, November 1-4, 2015.

[74] D. Xiao, W. Li, Zh. Hou, K. Lu, Y. Shi, Y. Wu, and X. Wu. Fused silica micro shell resonator with t-shape masses for gyroscopic application. *IEEE Journal of Microelectromechanical Systems (JMEMS)*, 27(1):47–58, 2017.

[75] D. Senkal, M.J. Ahamed, and A.M. Shkel. Design and modeling of micro-glassblown inverted-wineglass structures. *IEEE International Symposium on Inertial Sensors and Systems (INERTIAL)*, pages 1–4, Laguna Beach, CA, Feb. 25-26, 2014.

[76] B. Shiari, T. Nagourney, A. Darvishian, J.Y. Cho, and K. Najafi. Simulation of blowtorch reflow of fused silica micro-shell resonators. *IEEE Journal of Microelectromechanical Systems (JMEMS)*, 26(4):782–792, 2017.

[77] R.H. Doremus. Viscosity of silica. *Journal of Applied Physics*, 92(12):7619–7629, 2002.

[78] M.K. Choudhary, R. Venuturumilli, and M.R. Hyre. Mathematical modeling of flow and heat transfer phenomena in glass melting, delivery, and forming processes. *International Journal of Applied Glass Science*, 1(2):188–214, 2010.

[79] M.H. Asadian, R.M. Noor, and A.M. Shkel. Simulation-based approach in design of 3D micro-glassblown structures for inertial and optical sensors. *IEEE Sensors Conference (SENSORS)*, Montreal, QC, Canada, October 27-30, 2019.

[80] B.S. Lunin and K.V. Tokmakov. Reduction in internal friction in silica glass with high oh content. *Journal of the American Ceramic Society*, 102(6):3329–3340, 2018.

[81] B. Shiari, T. Nagourney, A. Darvishian, J.Y. Cho, and K. Najafi. Numerical prediction of stress evolution during blowtorch reflow of fused silica micro-shell resonators. *IEEE International Symposium on Inertial Sensors and Systems (INERTIAL)*, Laguna Beach, CA, Feb. 22-25, 2016.

[82] B.S. Lunin, A.N. Kharlanov, and S.E. Kozlov. Dehydroxylation and formation of ku-1 silica glass surface defects during annealing. *Moscow University Chemistry Bulletin*, 65(1):34–37, 2010.

[83] A. Ageev, B.C. Palmer, A. De Felice, S.D. Penn, and P.R. Saulson. Very high quality factor measured in annealed fused silica. *Classical and Quantum Gravity*, 21(16):3887–3892, 2004.

[84] A. Jeanroy and P. Leger. Gyroscopic sensor and rotation measurement apparatus constituting an application thereof. US Patent 6,474,161, Nov. 2002.

[85] D. Senkal, M.J. Ahamed, M.H. Asadian, S. Askari, and A.M. Shkel. Out-of-plane electrode architecture for fused silica micro-glassblown 3-D wineglass resonators. *IEEE Sensors Conference (SENSORS)*, Valencia, Spain, November 2-5, 2014.

[86] M.H. Asadian, , Y. Wang, and A.M. Shkel. Development of 3D fused quartz hemitoroidal shells for high-Q resonators and gyroscopes. *IEEE Journal of Microelectromechanical Systems (JMEMS)*, (article in press), 2019.

[87] D.M. Tanner, J.A. Walraven, K. Helgesen, L.W. Irwin, F. Brown, N.F. Smith, and N. Masters. MEMS reliability in shock environments. *IEEE 38th Annual International Reliability Physics Symposium Proceedings*, San Jose, CA, April 10-13, 2000.

[88] S.W. Yoon, N. Yazdi, N.C. Perkins, and K. Najafi. Micromachined integrated shock protection for MEMS. *Sensors and Actuators A: Physical*, 130:166–175, 2006.

[89] E.E. Aktakka, J.-K. Woo, D. Egert, R.J.M. Gordenker, and K. Najafi. A microactuation and sensing platform with active lockdown for in situ calibration of scale factor drifts in dual-axis gyroscopes. *IEEE/ASME Transactions on Mechatronics*, 20(2):934–943, 2014.

[90] S.J. Kim, R. Dean, G. Flowers, and C. Chen. Active vibration control and isolation for micromachined devices. *Journal of Mechanical Design*, 131(9):091002, 2009.

[91] H. Wen, A. Daruwalla, C.-S. Liu, and F. Ayazi. A high-frequency resonant framed-annulus pitch or roll gyroscope for robust high-performance single-chip inertial measurement units. *IEEE Journal of Microelectromechanical Systems (JMEMS)*, 27(6):995–1008, 2018.

[92] J.Y. Cho, J.-K. Woo, J. Yan, R.L. Peterson, and K. Najafi. Fused-silica micro birdbath resonator gyroscope. *IEEE Journal of Microelectromechanical Systems (JMEMS)*, 23(1):66–77, 2014.

[93] J.Y. Cho, T. Nagourney, A. Darvishian, and K. Najafi. Ultra conformal high aspect-ratio small-gap capacitive electrode formation technology for 3D micro shell resonators. *IEEE International Conference on Micro Electro Mechanical Systems (MEMS)*, Las Vegas, NV, Jan. 22-26, 2017.

[94] A.M. Shkel and M.H. Asadian. Fused quartz dual shell resonator and method of fabrication. UC Case No. 2019-670, 2019.

[95] G.H. Bryan. On the beats in the vibrations of a revolving cylinder or bell. *Proceedings of the Cambridge Philosophical Society*, 7(24):101–111, 1890.

[96] M.H. Asadian, Y. Wang, Radwan Noor, and A.M. Shkel. Design space exploration of hemi-toroidal fused quartz shell resonators. *IEEE International Symposium on Inertial Sensors and Systems (INERTIAL)*, Naples, FL, April 1-5, 2019.

[97] M.H. Asadian, Y. Wang, and A.M. Shkel. Design and Fabrication of 3D Fused Quartz Shell Resonators for Broad Range of Frequencies and Increased Decay Time. *IEEE Sensors Conference (SENSORS)*, New Delhi, India, October 28-31, 2018.

[98] J. Cao and C. Nguyen. Drive amplitude dependence of micromechanical resonator series motional resistance. *Digest of Technical Papers, International Conference on Solid-State Sensors and Actuators*, Sendai, Japan, June 7, 1999.

[99] A.A. Trusov, A.R. Schofield, and A.M. Shkel. Micromachined tuning fork gyroscopes with ultra-high sensitivity and shock rejection. US Patent 8,322,213, Dec. 2012.

[100] A.D. Challoner, H.G. Howard, and J.Y. Liu. Boeing disc resonator gyroscope. *IEEE/ION Position, Location and Navigation Navigation Symposium PLANS*, Monterey, CA, May 5-8, 2014.

[101] S.A. Zotov, B.R. Simon, G. Sharma, J. Han, I.P. Prikhodko, A.A. Trusov, and A.M. Shkel. Investigation of energy dissipation in low frequency vibratory. MEMS demonstrating a resonator with 25 minutes time constant. *Solid-State Sensors, Actuators, and Microsystems Workshop, Hilton Head Island, SC, USA*, June 8-12, 2014.

[102] S. Askari, M.H. Asadian, K. Kakavand, and A.M. Shkel. Near-Navigation Grade Quad Mass Gyroscope with Q-factor Limited by Thermo-Elastic Damping. *Solid-State Sensors, Actuators, and Microsystems Workshop*, Hilton Head Island, SC, USA, June 5-9, 2016.

[103] M.H. Asadian, S. Askari, I.B. Flader, Y. Chen, D.D. Gerrard, D.D. Shin, H.-K. Kwon, T.W. Kenny, and A.M. Shkel. High quality factor mode ordered dual foucault pendulum gyroscope. *IEEE Sensors Conference (SENSORS)*, New Delhi, India, October 28-31, 2018.

[104] T. Nagourney, J.Y. Cho, A. Darvishian, B. Shiari, and K. Najafi. 130 Second Ring-Down Time and 3.98 Million Quality Factor in 10 kHz Fused Silica Micro Birdbath Shell Resonator. *Solid-State Sensors, Actuators, and Microsystems Workshop, Hilton Head Island, SC, USA*, June 5-9, 2016.

[105] A.B. Graham, M.W. Messana, P.G. Hartwell, J. Provine, S. Yoneoka, R. Melamud, B. Kim, R.T. Howe, and T.W. Kenny. A method for wafer-scale encapsulation of large lateral deflection MEMS devices. *IEEE Journal of Microelectromechanical Systems (JMEMS)*, 19(1):28–37, 2009.

[106] S.-H. Lee, J. Cho, S.W. Lee, M.F. Zaman, F. Ayazi, and K. Najafi. A low-power oven-controlled vacuum package technology for high-performance MEMS. *IEEE International Conference on Micro Electro Mechanical Systems (MEMS)*, Sorrento, Italy, Jan. 25-29, 2009.

[107] M. Esashi. Wafer level packaging of MEMS. *Journal of Micromechanics and Microengineering*, 18(7):p.073001, 2008.

[108] S.-H. Choa. Reliability of MEMS packaging: vacuum maintenance and packaging induced stress. *Microsystem technologies*, 11(11):1187–1196, 2005.

[109] T.F. Marinis and J.W. Soucy. Vacuum packaging of MEMS inertial sensors. *International Society for Optical Engineering SPIE*, Boston, MA, USA, November 2003.

[110] E. Rizzi, L. Mauri, M. Moraja, A. Conte, A. Bonucci, G. Longoni, and M. Amiotti. *Outgassing and Gettering in Handbook of silicon based MEMS materials and technologies*. William Andrew, 2015.

[111] I.P. Prikhodko, B.R. Simon, G. Sharma, S.A. Zotov, A.A. Trusov, and A.M. Shkel. High and moderate-level vacuum packaging of vibratory MEMS. *International Microelectronics Assembly and Packaging Society (IMAPS)*, Orlando, FL, USA, October 2013.

[112] B. R. Simon, S. Khan, A.A. Trusov, and A.M. Shkel. Mode ordering in tuning fork structures with negative structural coupling for mitigation of common-mode g-sensitivity. *IEEE Sensors Conference (SENSORS)*, Busan, South Korea, November 1-4, 2015.

[113] M.H. Asadian, S. Askari, and A.M. Shkel. An ultrahigh vacuum packaging process demonstrating over 2 million Q-factor in MEMS vibratory gyroscopes. *IEEE Sensors Letters*, 1(6), 2017.

[114] D. Senkal, A. Efimovskaya, and A.M. Shkel. Dual foucault pendulum gyroscope. *the International Conference on Solid-State Sensors, Actuators and Microsystems (TRANSDUCERS)*, Anchorage, Alaska, USA, June 21-25, 2015.

[115] J. Bernstein, S. Cho, A.T. King, A. Kourepenis, P. Maciel, and M. Weinberg. A micromachined comb-drive tuning fork rate gyroscope. *IEEE International Conference on Micro Electro Mechanical Systems (MEMS)*, Fort Lauderdale, FL, USA, Feb. 10, 1993.

[116] D. Senkal, A. Efimovskaya, and A.M. Shkel. Minimal realization of dynamically balanced lumped mass WA gyroscope: dual foucault pendulum. *IEEE International Symposium on Inertial Sensors and Systems (INERTIAL)*, Hapuna Beach, HI, March 23-26, 2015.

[117] J. Giner, Y. Zhang, D. Maeda, K. Ono, A.M. Shkel, and T. Sekiguchi. Dynamicaly balanced degenerate mode gyro with sub-hz frequency symmetry and temperature robustness. *IEEE International Conference on Micro Electro Mechanical Systems (MEMS)*, Las Vegas, NV, Jan. 22-26, 2017.

[118] M.F. Zaman, A. Sharma, Z. Hao, and F. Ayazi. A mode-matched silicon-yaw tuning-fork gyroscope with sub degree-per-hour allan deviation bias instability. *IEEE Journal of Microelectromechanical Systems (JMEMS)*, 17(6):1526–1536, 2008.

[119] A. Efimovskaya and A.M. Shkel. Multi-Degree-of-Freedom MEMS Coriolis Vibratory Gyroscopes Designed for Dynamic Range, Robustness, and Sensitivity. *DGON Inertial Sensors and Systems (ISS)*.

[120] Doruk Senkal, Sergei A Zotov, and Andrei M Shkel. Fully balanced micro-machined inertial sensor. US Patent App. 10/247,554, April 2019.

[121] I.B. Flader, Y. Chen, C.H. Ahn, D.D. Shin, A.L. Alter, J. Rodriguez, and T.W. Kenny. Epitaxial encapsulation of fully differential electrodes and large transduction gaps for MEMS resonant structures. *IEEE International Conference on Micro Electro Mechanical Systems (MEMS)*, Belfast, Northern Ireland, UK, Jan., 21-25, 2018.

[122] Y. Wang, Y.W. Lin, J. Rodriguez, G.D. Vukasin, D.D. Shin, H.K. Kwon, D.B. Heinz, Y. Chen, D.D. Gerrard, T.W. Kenny, and A.M. Andrei. On decoupled quantification of energy dissipation mechanisms in toroidal ring gyroscopes. *Solid-State Sensors, Actuators, and Microsystems Workshop, Hilton Head Island, SC, USA*.

[123] C. Zener. Internal friction in solids. I. Theory of internal friction in reeds. *Physical review*, 52(3):230, 1937.

[124] M.H. Asadian, S. Askari, Y. Wang, and A.M. Shkel. Characterization of energy dissipation mechanisms in dual foucault pendulum gyroscopes. *IEEE International Symposium on Inertial Sensors and Systems (INERTIAL)*, Naples, FL, April 1-5, 2019.

Appendix A

Die-level vacuum packaging of MEMS inertial sensors

A.1 Purpose

This procedure describes the steps for vacuum sealing of MEMS devices in ceramic packages with (Kovar/Glass) lids. The procedure includes the basic operating steps and temperature profiles to run a successful sealing process. The temperature profile is developed for AuSn Eutectic solder preform and getter activation. This procedure includes processes for

- Sealing furnace chamber bake-out
- LCC package back process
- Ultra-high-vacuum sealing of sensors

The Q-factor of the MEMS resonators is a measure of vacuum level inside the sealed packages. The Q-factor measurements over a long period after sealing is an indication of activated getter inside the sealed package.

Table A.1: Required and Recommended equipment and parts

Instrument/Part	Recommended Models/Material	Manufacturer/Supplier
Vacuum sealing furnace	SST 3150	SST International (Palomar Technologies)
Liquid chiller	OTC-3.0AL-C3-236-SC1-M12	OptiTemp
Cryo Compressor	CTI 8200	Brooks Automatic Inc.
Tack-welding station	UB25 UNIBOND	Amada Miachi Inc.
Lid	Kovar	HRA (Hi-REL Alloys) ULC
Eutectic preform	Gold-Tin (80-20)	HRA (Hi-REL Alloys) ULC
Thin film getter deposition	PaGe Getter	SAES Getter

A.2 Scope

This procedure applies only to SST 3150 vacuum sealing furnace, and was developed in UCI Microsystems lab from January 2014 to March 2015. All the materials, parts, and equipment to perform the vacuum sealing of MEMS inertial sensors are listed in Table A.1.

A.3 Procedure

The main components of vacuum sealing setup are connected, as shown in Fig. A.1:

- OptiTemp liquid chiller is located outside of the soft-wall cleanroom providing water circulation for cooling down the sealing furnace.

- SST 3150 vacuum sealing furnace is located inside the soft-wall cleanroom, compressed air and nitrogen are supplied to the SST by lab compressed air line and nitrogen tank. The main power switch of the SST 3150 furnace is mounted on the wall outside the soft-wall cleanroom.

- Brooks CTI compressor is located inside the soft-wall cleanroom, provides gas circulation to the SST chamber.

4.3.1 Power ON the liquid chiller, before turning ON the chiller, remove the top cover carefully and check the water level of the chiller. If the water level is below the minimum line, you should open the lid and add (only) distilled water. Also, check the back of the chiller near the filter and make sure there is no leakage. Filter and water have to be re-

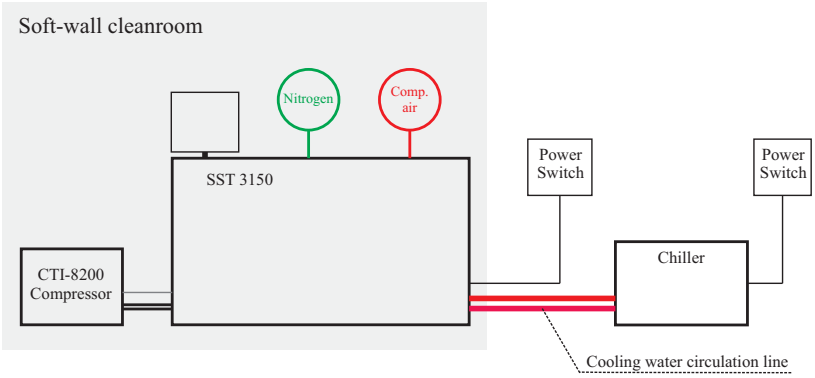

Figure A.1: Diagram of the major components of the vacuum sealing setup.

Figure A.2: From left to right, showing the state of chiller before and after Power ON.

freshed every year according to the label on the front panel, refer to the OptiTemp manual No. O002639AD.

Switch ON the main power of the OptiTemp liquid chiller. The switch is mounted on the wall on the top-right of the chiller and is labeled as OptiTemp chiller. Turn ON the chiller, the SYSTEM RUN green indicator lights on, the FREEZE ALARM red indicator lights on, and after few seconds temperature controller displays PV and SV numbers. At this moment you hear the noise of fans starting, and the FREEZE ALARM goes OFF. By default, the chiller temperature set value is on 62.5 F. Fig. A.2 shows the front panel before and after turning ON the chiller.

Power ON the SST 3150 Furnace, switch ON the main power of the SST 3150 Furnace. The switch is mounted in the wall outside of the cleanroom on the top-left of the chiller and is labeled as SST 3150.

Turn ON the nitrogen tank valve behind the SST 3150 furnace in the soft-wall cleanroom area. There are two pressure gauges connected to the nitrogen tank, the closer to the valve indicates the pressure inside the tank and the other one indicates the pressure after the regulator. Two black lines are drawn on the pressure gauges showing the minimum operating nitrogen pressure (260 kPa) for the unit.

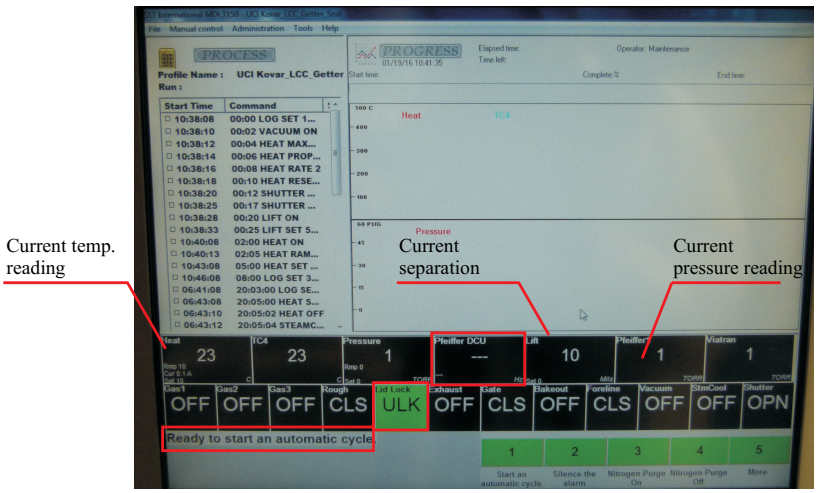

Figure A.3: SST software default screen after turning on the unit.

At this moment, the red light (stop button) on the front panel of the SST 3150 furnace is lit. To turn on the unit, push the start button. The green light goes on indicating system is turned ON. You see the operating system is loading on the screen and after 1 minute SST software starts and asks for the login information.

Log in to SST 3150 Furnace and the Default Screen, you can login using "Administrator" account for running the tool, or "Maintenance" account for the maintenance purposes. After you log in, you see the screen as it is shown in the Fig.A.3. You should see the message on the bottom-left of the screen: Ready to start an automatic cycle.

On the default screen, you can see following information:

- Current temperature reading of the main thermocouple in Celsius in a box labeled as Heat.

- Current separation between bottom and top graphite plates in Mils in a box labeled as Lift.

- Current pressure reading in Torr in a box labeled as Pfeiffer1. - Current status of the lid indicating ULK meaning unlocked in a box labeled as Lid Lock.

- All boxes other than Lid Lock should be in black at this moment. - Current speed of the turbo pump is Hertz is indicated in a box labeled as Pfeiffer DCU.

Turn ON the turbo pump, at this moment, the turbopump speed is zero and showing — in the Pfeiffer DCU box. To start using SST 3150, turbopump has to be turned ON.

Otherwise, a red error box appears on the screen and alarm goes ON indicating an error in the operation. To turn on the turbopump, go to Manual Control menu and click on Vacuum Pump. (Or, click on more button on the bottom-right of the screen and navigate through quick access menu and click on Vacuum Pump ON). It will take a few minutes for the turbopump to reach its maximum nominal speed (820 Hz). After the speed reaches 800 Hz, the Pfeiffer DCU turns to green indicating that the unit is ready to use.

Opening the chamber lid, At this moment, the system is ready to load your packages. If the chamber is at atmospheric pressure, you can open the lid by turning the wheel lock counter clock-wise. However, most of the time, you will find that the chamber is kept in a vacuum. This is crucial to keep the chamber in a vacuum to avoid contamination and moisture absorption on the inner surface and graphite plates.

If the chamber is in a vacuum, you have to purge the chamber. Navigate through the quick access menu at the bottom-right of the screen and click Nitrogen Purge ON. You will hear the sound of valve opening and pressure rising in the chamber. Once you read 760 Torr on the Pfeiffer1 box and 2 PSIG on the Viatran box you click on Nitrogen Purge OFF. At this moment you can open the lid by turning the wheel lock CCW.

Turn the wheel lock slowly and completely until the lid reaches its highest position. Then, turn the lid slowly to the right to clear the opening of the chamber. Be very careful not to cause any twist or excessive tension on the water lines attached to the lid. Note: Before opening the lid, wipe the top surface of SST with IPA and remove all source of dust (papers, etc.)

Loading packages and lids, Note: while you are handling the graphite tooling parts, you MUST avoid rushing through the process, you should slow down your movement when you load or unload the graphite plates to avoid any crashing or breaking the fragile graphite parts. When you open the chamber, you should see the load plate and two graphite springs, Fig. A.4.

Start with removing the graphite springs, use quick-release t-bars to grab the graphite parts.

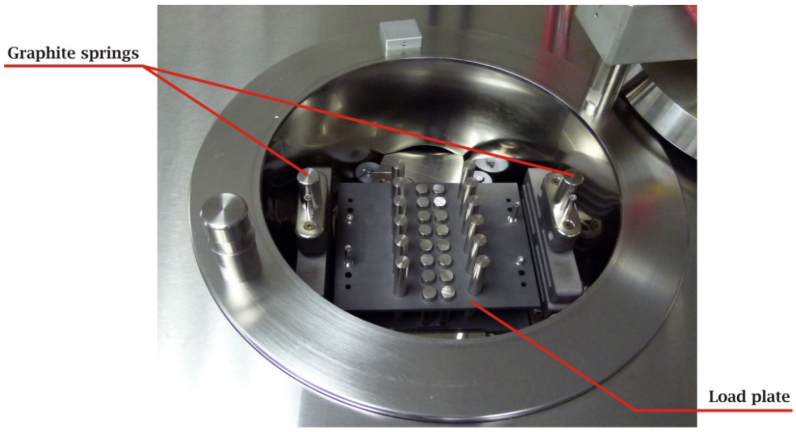

Figure A.4: Graphite springs and the load plate position, you should see these parts anytime you open the SST chamber.

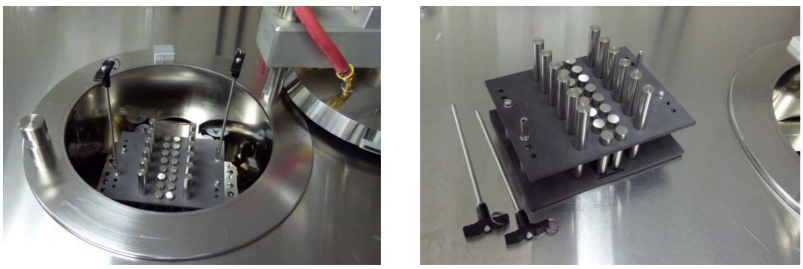

Figure A.5: Quick-release t-bars are locked in the load plate pins and used to handle the graphite load plate.

Remove the springs and place them in the spring nests.

Then, you should remove the load plate. This is the heaviest piece of the graphite tooling. Be extremely careful when you use quick-release t-bars make sure that the t-bars are fully locked in the pins. Grab the load plate with t-bars and remove it from the chamber. Leave it on a clean surface on top panel of SST, Fig. A.5.

The next step is to remove the lift plate. The lift plate is used to load packages. Use the same technique that was explained for removing the load plate to remove the lift plate. There might be a thermocouple attached to lift plate, carefully remove the thermocouple before fully removing the lift plate from the chamber.

After removing the lift plate, you see the boat plate. The boat plate has lots to hold lids (Kovar/glass). The main thermocouple of the system is attached to the boat plate. You can load the lids on the lots without removing the graphite plate. There are three columns of lots on the boat plate. On the left column, there are six lots for Kovar lids for LCC packages.

The column in the middle has eight lots for Kovar/glass lids for DIP packages. The right column has 6 lots for Kovar/glass lids for LCC packages.

Note: In all of the graphite plates, left side refers to the side that serial number is written on the plate.

Note: Before replacing the graphite plates to the chamber, make sure that the main thermocouple is fully inserted in the boat plate.

The same number of lots is available on the lift plate. The side columns are dedicated to LCC packages, and the middle one is for DIP packages. From the tooling configuration, the packages have to be loaded upside down on the lift plate.

After loading lids and packages, replace the lift plate, load plate, and graphite springs. Then, close the chamber lid and lock the wheel lock clockwise.

Note: lift plate and load plate are directly sitting on the lift mechanism of the SST furnace. Any excessive load or shock on the lift mechanism causes the mechanism going out of calibration.

Run a profile, after closing the chamber lid, on the software you go to Administration menu and click on Profiles. All the developed processes are available in the profiles window. You scroll up/down through the list of processes and find the desired process. The main processes are:

- UCI Chamber Bake: for baking-out the chamber
- UCI Package Bake: for ceramic package de-hydrogenation
- UCI Kovar LCC Getter Seal: for sealing devices in LCC packages with Kovar lids
- UCI Glass LCC Getter Seal: for sealing devices in LCC packages with glass lids

After selecting your process, click on Load. Then go to the main software, and you will see a preview of the steps on the left side of the screen. To start the process, navigate through the quick access menu and select Run an automatic cycle, click yes to confirm.

At this moment, the status of the tool changes from Ready to run an automatic cycle to run in cycle. This means that the process is running. As time passes, you see the pressure

drops as the turbopump is running. Temperature and separation also change based on the temperature profile and steps of the process. After the process is completed, the status changes to Run complete. The chamber lid will be locked until the temperature falls below 80 C. To open the lid and remove the packages, follow the steps in sections 4.3.4 and 4.3.5.

Shut down the furnace, after you replace all the graphite tooling back to the chamber and close the lid, you should turn on the vacuum before shutting down the tool. This dramatically helps to keep the chamber clean and moisture-free for the next run.

To do so, navigate through the quick access menu and find Vacuum before shut down. This will run turn on the vacuum for 5 minutes and turn it off. After this process is completed, you click on the Powerdown the machine in the quick access menu and confirm. This will safely turn off the whole system.

After turning off the machine:

1- Push the stop button on the front panel of SST

2- Fully close the Nitrogen tank valve

3- Turn OFF the main power switch

4- Turn OFF the chiller

5- Turn OFF the chiller main power switch

Precautions, you should watch the tool during the first 30 minutes to make sure all the primary steps are running without any issue. If you are running a long process (¿48 hours), you should periodically go and check the status of the machine. Although this is an industrial-level and reliable tool, it may fail during a process. Try to be around the machine to check any error messages or alerts.

For high-temperature applications, above 600℃, please consult SST engineers.

Do not use non-standard loads on the load plate. The lift mechanism has a limited load capacity; if you exceed that limit, you may damage the lift mechanism.

A.4 Ultra-high vacuum sealing recipe

The following recipe was developed for vacuum sealing of MEMS gyroscopes at UCI Microsystems laboratory. The process parameters were optimized with respect to the packaging materials (LCC packages and Kovar lids with deposited getter) and the custom tooling assembly (graphite boat, lift plate, and load plate) that were used in the SST 3150 furnace. The pre-bake duration can be modified to make it shorter or longer. The vacuum sealing process yield above 90% was achieved with this recipe. A complete elimination of air damping was claimed in QMG [102] and mode-ordered DFP [124] with the Q-factor limited by Q_{TED}.

00:00 LOG SET 10 SEC

00:02 VACUUM ON

00:04 HEAT MAXPOWER 60

00:06 HEAT PROPBAND 50

00:08 HEAT RATE 2

00:10 HEAT RESET 7

00:12 SHUTTER OPEN

00:17 SHUTTER OPEN CHECK

00:20 LIFT ON

00:25 LIFT SET 500 MILS

02:00 HEAT ON

02:05 HEAT RAMP 220 C

05:00 HEAT SET 220 C

08:00 LOG SET 300 SEC

32:03:00 LOG SET 10 SEC

32:05:00 HEAT SET 220 C

32:05:02 HEAT OFF

32:05:04 Steamcool On

32:05:32 LIFT SET 1850 MILS

32:07:00 SHUTTER CLOSE

32:07:05 SHUTTER CLOSE CHECK

34:05:50 Steamcool Off

34:06:00 HEAT ON

34:06:05 HEAT RAMP 445 C

34:13:00 HEAT SET 445 C

34:53:00 HEAT SET 445 C

34:53:02 HEAT OFF

34:53:07 Steamcool On

34:53:10 LOG SET 30 SEC

35:23:05 Steamcool Off

35:23:07 LOG SET 10 SEC

35:23:10 SHUTTER OPEN

35:23:15 SHUTTER OPEN CHECK

35:23:20 LIFT ON

35:23:30 LIFT SET 10 MILS

35:24:31 HEAT ON

35:24:36 HEAT RAMP 360 C

35:32:33 HEAT SET 360 C

35:40:33 HEAT SET 360 C

35:40:34 HEAT OFF

35:40:36 Steamcool On

36:39:23 Steamcool Off

36:42:23 VACUUM OFF

36:42:55 BEEP ON

36:42:56 BEEP OFF

Appendix B

List of Vendors and Suppliers

Airgas USA, LLC-West Region.
23585 Los Adornos Aliso Viejo, CA 92656
Contact: 619-787-1425.
Website: *http://www.airgas.com/*
Email: *Todd.Price@airgas.com* (Todd Price)
NOTE: supplier of high purity nitrogen gas for SST furnace and AML wafer bonder. supplier of liquid nitrogen for LakeShore probe station.

Allied HighTech
2376 East Pacifica Place, Rancho Dominguez, CA 90220
Contact: 800-675-1118
Website: *www.alliedhightech.com*
NOTE: This vendor provides polishing equipment and consumables. The 12-inch MultiPrep lapping machine was used in the release process of shell and dual-shell resonators.

Amada Miyachi America, Inc.
1820 South Myrtle Avenue, PO Box 5033, Monrovia, CA 91016 USA
Contact: 626-930-8582
Website: *www.amadamiyachi.com*
NOTE: manufacturer of precision welding workstations.

Bonding Source
Contact: 603-595-9600
Website: *http://www.bondingsource.com/*
NOTE: supplier of adhesive epoxies and wires for wirebonders.

Brooks Automation, Inc.

15 Elizabeth Drive, Chelmsford, MA 01824
Contact: (978)262-2400.
Website: *http://www.brooks.com*
NOTE: manufacturer of cryo compressors (CTI-8200) for SST sealing furnace.

ElectroTech Machining
2000 W. Gaylord St. Long Beach, CA 90813
Contact: 217-974-5510.
Website: *https://www.etmgraphite.com*
Note: local machine shop for machining of graphite parts for the die-attachment and vacuum sealing furnaces.

First Contact Polymer
1895 Short Lane, Platteville, WI 53818
Contact: 608-467-5396
Website: *http://www.photoniccleaning.com*
NOTE: supplier of first contact polymer for cleaning of glass and optics.

Hi-Rel Alloys
6934 Kinsmen Ct. Niagara Falls, Ontario Canada, L2H 0Y5
Contact: (289) 296-4078
Website: *www.hirelgroup.com*
NOTE: supplier of AuSn eutectic preforms and Kovar lids.

Mark Optics
1424 E. St. Gertrude Place, Santa Ana, CA 92705
Contact: 714-545-6684 (Erika Puentes).
Website: *www.markoptics.com*
NOTE: supplier of fused silica wafers with different materials and grades.

Micro Connex
34935 SE Douglas Street, Suite 110, Snoqualmie WA, 98065
Contact: 425-396-5707
Website: *http://www.microconnex.com*
NOTE: laser drilling of fused silica wafers

MTI Corp.
860 S. 19th Street, Richmond, CA 94804-3809.
Contact: 510-525-3070.
Website: *http://www.mtixtl.com/*
NOTE: manufacturer of the glassblowing furnace, supplier of parts for the furnace.

Opti Temp, Inc.
1500 International Drive, Traverse City, MI 49686
Contact: 231-946-2931
Website: *http://www.optitemp.com*
NOTE: manufacturer of the liquid chiller for vacuum sealing setup and supplier of consumables.

Photo-sciences,
2542 W 237th St., Torrance, CA, 90505.
Contact: 310-634-1500.
Website: *https://dev.photo-sciences.com/*
NOTE: Supplier of high-quality chrome masks with fast turn around.

PTB Sales
1361 Mountain View Circle, Azusa, CA 91702
Contact: 626-334-0500.
Website: *http://www.ptbsales.com/*
NOTE: Local Vacuum system repair.

SAES Getters
1122 E. Cheyenne Mountain BLVD Colorado Springs, CO 80906
Contact: 719-527-4116.
Website: *https://www.saesgetters.com/*
NOTE: Supplier of patterned getter (PaGe) on Kovar lids for ultra high vacuum sealing process.

Sierra Assembly Technology Inc.
10880 Mulberry Ave, Fontana, CA 92337
Contact: 909-355-5400.
Website: *https://www.protoexpress.com/*
NOTE: This vendor supplies high-quality, specialized PCBs. .

SPECTRUM MICROMECHANICAL, INC.
4182 Sorrento Valley Blvd. Suite G, San Diego, CA 92121
Contact: 858-395-2264
Website: *www.spmmi.com*
NOTE: local wafer dicing service.

SST International
9801 Everest St, Downey, CA 90242
Contact: 562-803-3361
Website: *http://www.palomartechnologies.com/sst-international*
NOTE: manufacturer of vacuum sealing furnace, and supplier of the consumables.

Transene Company, Inc.
10 Electronics Avenue, Danvers MA 01923
Contact: 978-777-7860
Website: *www.transene.com*
NOTE: supplier of metal etchants.

UC Berkeley Nano Lab
520 Sutardja Dai Hall MS 1754, BERKELEY, CA 94720
Contact: 510-809-8612
NOTE: LPCVD Polysilicon deposition service.

UC Irvine FABWorks

University of California Irvine, California IT2, Irvine, CA 92697.
Contact: 949-824-5667.
Website: *http://manufacturing.uci.edu/index.php/fabworks-2/*
NOTE: self serve 3D printing, laser cutting, and CNC machining.

University Wafer
850 Summer St. Suite# 207, Boston, MA 02127, USA
Contact: 800-713-9375 (Chris Baker).
Website: *www.UniversityWafer.com*
NOTE: Supplier of prime Si wafers with different thicknesses as well as borosilicate glass wafers.